Experimental Investigation of the Aerodynamics of a Reverse Delta Wing in Ground Effect Using Passive Control

Submitted by

David Huitema
Department of Mechanical Engineering
McGill University
Montreal, Quebec, Canada
August 2, 2018

A thesis submitted to McGill University in partial fulfilment of
requirements of the degree of Master of Engineering

ACKNOWLEDGEMENTS

I'm deeply thankful and immensely grateful to my supervisor, Professor Lee, for his support and guidance during my Master's studies. His steady hand, encouragement, and continuous support have been instrumental in this work. I am particularly grateful to my colleague Vincent Tremblay-Dionne, for his assistance in the creation of the experimental models, data acquisition and for his continuous help during the course of my research.

Many thanks and appreciation go to my colleagues at the Experimental Aerodynamics Laboratory: Lok Sun Ko, Pedro Leite, Amaan Majeed, Bilal Siddiqui, and Shawn He. Their presence made many long days feel short, and their insights, suggestions, and discussions are greatly appreciated.

I thank my parents and siblings for their support and encouragement. Special thanks goes to my friends who have been both inspiring and encouraging.

ABSTRACT

Wing-in-ground effect craft utilize the lift augmentation and drag reduction experienced by aircraft flying in close proximity to the ground. Several designs use a reverse delta wing with anhedral tips due to improved stability in ground effect, despite the inferior lift generation of this planform limiting its widespread adoption. Also, archived research into reverse delta wings is limited, especially in ground effect. The aerodynamic forces generated by a slender and non-slender reverse delta wing in ground effect was experimentally investigated using force balance measurements in an open return wind tunnel. The impact of anhedral, rear planform cropping and passive control via Gurney flaplike strips was investigated.

The results demonstrate that the impact of ground effect on the reverse delta wing was greatest at low angles of attack and ground clearances. Increased lift is in part a result of increased static pressure on the lower surface. Anhedral further increased lift, suggesting the stagnation of high momentum flow beneath the wing resulting in an "air tunnel" like effect and resulting in significant lift increases at low ground clearances and high anhedral angles. The relation between the lift and drag increments in ground effect was found to be approximately linear, with marginal improvement in the lift-to-drag ratio. In the freestream, employment of side-edge strips shifted the lift-curve leftward (induced camber-like effect), resulting from reduced crossflow leakage and increased windward surface pressure. Equipping these strips in ground effect significantly augmented lift with increasing strip height. An increasingly adverse pressure gradient and extension of the side-edge strip beyond the boundary layer led to increased drag with strip height. Rear planform cropping in freestream conditions had a benign impact on aerodynamic forces, while in ground effect increased lift and drag from greater ground proximity, with increased drag suggesting an enhanced disruption of the spanwise vortex filaments. The optimum configuration was found to be a 30% cropped reverse delta wing with 15-degree anhedral, equipped with side-edge strips with height of 4% of the root chord, resulting in significant lift and aerodynamic efficiency improvements alongside weight loss from the cropping. The above findings generally agreed with the results for the non-slender models, with greater force magnitudes observed for the non-slender case. A non-zero lift coefficient was observed at zero incidence for the non-slender wing in ground effect. Further study is required to elucidate the flow mechanisms.

The results presented here are first of a kind for a reverse delta wing in ground effect, demonstrating that lift augmentation may be achieved on reverse delta wings operating in ground effect through the utilization of passive control. These results provide benchmark data for further studies on reverse delta wings in and out of ground effect.

ABRÉGÉ

Les avions à effet de sol utilisent l'augmentation de la portance et la réduction de la traînée auxquels ils sont soumis près du sol. Plusieurs conceptions utilisent une aile delta inversée en raison d'une meilleure stabilité de l'effet de sol, malgré une portance moindre limitant son adoption généralisée. De plus, peu d'études ont été conduites sur ces ailes, en particulier en cas d'effet de sol. Les forces aérodynamiques générées par l'effet de sol sur une aile delta inversée, qu'elle soit élancée ou non, ont été étudiées expérimentalement en utilisant des balances de force dans une soufflerie. L'impact du dièdre négatif, d'une réduction de la surface alaire et du contrôle passif via des bandes de type Gurney on été étudiés.

Les résultats démontrent que sur une aile delta inversée, l'impact de l'effet de sol est plus important près du sol et aux angles d'attaque plus faibles. La portance accrue résulte d'une augmentation de la pression statique sur la surface inférieure. Le dièdre négatif augmente ce flux stagnant, produisant un effet de « tunnel d'air », emprisonnant sous l'aile un flux à forte quantité de mouvement et résultant en une augmentation significative de la portance par rapport à l'aile de référence pour de faibles hauteurs par rapport au sol et des dièdres fortement négatifs. La relation entre les incréments de portance et de traînée en effet de sol s'est avérée être approximativement linéaire, avec une amélioration marginale de la finesse. En écoulement libre, l'ajout de bandes sur les bords latéraux décale vers la gauche la courbe de portance, grâce à une réduction des fuites par écoulement transversal et à une augmentation de la pression statique sur la surface inférieure. L'emploi de ces bandes en effet de sol entraine une augmentation de la portance avec la hauteur de celles-ci. Un accroissement du gradient de pression inverse accompagné d'une extension de la bande latérale au-delà de la couche limite conduit à une augmentation de la traînée avec la hauteur de bande. Une réduction de la surface arrière a un impact négligeable sur les forces en écoulement libre, mais, en cas d'effet de sol, la portance et la traînée croissent du fait de la proximité du sol et la perte de cohérence des vortex le long de l'envergure de l'aile sont accrues. La configuration optimale déterminée est un dièdre négatif de 15 degrés, avec une réduction de 30% de la surface arrière, équipée de bandes latérales larges de 4% de la corde. Les paramètres obtenus précédemment sont généralement en accord avec les résultats découlant des modèles d'ailes non élancées, malgré des forces de magnitude plus importantes pour ces secondes. Un coefficient de portance non nul a été observé à angle d'incidence nul. Des études plus approfondies sont nécessaires pour expliquer le comportement du flux.

Ces résultats montrent qu'un ajout de la portance peut être obtenu pour une aile delta inversée en effet de sol avec le contrôle passif, et sont de référence pour de futures études.

CONTENTS

LIST OF SYMBOLS

b	geometric wing span
c	root chord of wing
C_D	total drag coefficient
C_L	total lift coefficient
C_L/C_D	lift-to-drag ratio
C_{Lmax}	maximum C_L
h	distance between trailing edge of the wing and the ground, ground proximity
h_{SES}	strip height
Re	Reynolds number, $= cU_\infty/\nu$
S	projected wing surface area
S_{org}	original projected surface area of planar, non-cropped wing
U_∞	freestream velocity
α	angle of attack
α_{ss}	static-stall angle
Δ	increment
δ_A	anhedral angle
δ_D	dihedral angle
Λ	sweep angle
ν	fluid kinematic viscosity
ρ	fluid density

LIST OF FIGURES

LIST OF TABLES

Page

CHAPTER 1

INTRODUCTION

An aircraft flying in close proximity to the ground, such as experienced on take-off and landing for conventional aircraft, experiences an increase in lift and a reduction in drag, particularly lift-induced drag. The aerodynamic flowfield is altered by the presence of the solid boundary, increasing the static pressure underneath the aircraft wing through the RAM effect, also known as a dynamic air “cushion”. In the early days of aviation, it was observed that landing was possible at speeds lower than predicted, and some difficulty was observed when landing aircraft with high-lift wings. Early aviators reported feeling like the aircraft was floating above the ground on landing. An observation made in the January 25th, 1921 edition of *Aviation* about the Pischoff Avionette was that “the proximity of the lower wing to the ground, eight inches, causes the air imprisoned between the wing and the ground to act as a cushion” (Raymond 1921). In ground effect, the air becomes trapped beneath the lifting body, and similarly to the static air cushion of hovercraft, the dynamic air cushion generates the feeling of floating or hovering during an aircraft’s landing.

With increasing proximity to the ground, the gap between the boundary and the lower surface of the wing is reduced, thus preventing the free expansion of the air and increasing the static pressure while the dynamic pressure is reduced and the air stagnates. Additionally, the suction on the upper surface of the wing increases from accelerated flow over the upper surface. Thus, with increasing ground proximity the lift is generally increased. The downwash of the wing is decreased due to interference of the boundary with the tip vortices, increasing the effective angle of attack. As well, the effective span of the wing is increased as the air underneath the wing accelerates in the spanwise direction. These combined effects thus decrease the lift-induced drag, resulting in an improved lift-to-drag ratio for aircraft flying in ground effect.

Ground effect may explain why some birds, bats, and flying insects fly in close proximity to the ground. By utilizing the additional lift and reduced drag provided by this aerodynamic phenomenon, these animals require less energy to travel over a given distance. Larger flying birds may use ground effect for take-off assistance, and some birds with high wing loading routinely fly close to the water or ground. Similarly, ground effect vehicles or wing-in-ground effect (WIG) craft take advantage of these benefits, flying within less than ten percent of their wing span to the ground. The improved aerodynamic efficiency in ground effect leads to reduced fuel consumption, thus reducing operating costs and increasing range. As well, by operating in marine environments, it is possible to avoid the large airport infrastructure for takeoff or landing, as the aircraft can simply land in the water and taxi into a port. Operating at a low altitude, there is no need for a pressurized cabin and the craft has increased safety from being able to land in the water at any point during flight. Ground effect vehicles may be amphibious in nature and fly below surface radar, allowing greater operational capabilities. The operational benefits and increased speed of transport compared to marine vessels demonstrates a clear role for ground effect craft in the civil and military aviation industries.

1.1 DESCRIPTION OF WING-IN-GROUND EFFECT, AND EXISTING CRAFT

While the 1903 maiden flight of the Wright Brothers may have been performed entirely in ground effect, the added efficiency thus helping these pioneers make history, the first truly operational WIG craft was not developed until 60 years later in the 1960s. This is a result of the design of WIG craft being hindered by the power requirements to overcome hydrodynamic hump-drag during takeoff. The first operational WIG craft were the Russian Ekranoplans operating in the Baltic Sea in the 1970's and 1980's before the collapse of the Soviet bloc. The first of these, the KM-1, was dubbed the "Caspian Sea Monster" by the West, due to its immense size (approximately the same size as the AN-225). The Russian Ekranoplan is characterized by low aspect ratio rectangular wings and a large horizontal stabilizer elevated outside of ground effect. Several Ekranoplans also featured powered augmented ram (PAR), which used eight jet engines to re-direct high pressure exhaust under the wings for take-off assistance. These engines were not used for cruise flight, causing a significant penalty in order to overcome hydrodynamic hump-drag at take-off. Additionally, typical rectangular wings when in ground effect have poor longitudinal stability due to the modification of the pressure distribution in ground effect introducing undesirable pitching moments. The large horizontal stabilizer operating outside of ground effect is used to maintain control authority, but has significant structural and weight penalties.

In 1963, an alternative design was developed by Dr. Alexander Lippisch. The Lippisch-type WIG craft uses a reverse delta wing (RDW) as a planform (a delta wing with the leading and trailing edges reversed), with development proceeding through several experimental craft, the X-112 through X-114. The X-114 uses the reverse delta wing planform with anhedral wing tips, thus reducing hydrodynamic drag by significantly reducing the surface area immersed in water at takeoff. Reportedly, the X-114 flies by "floating on a cushion of air" further implying the beneficial impact of ground effect on its performance, though the X-114 is capable of short flight out of ground effect (Kocivar 1977). As well, the reverse delta wing planform has been proven to be advantageous in countering the longitudinal and height instabilities of the Ekranoplan-type WIG craft, and current variants of the X-114 are being developed today (e.g.: Airfish-8, WSH-500).

While the reverse delta wing planform is statically stable in ground effect, its lifting capacity is limited relative to conventional aircraft. A Gurney flap, used first by Daniel Gurney on a racing vehicle in the late 1960s, consists of a flat plate at 90° to the trailing edge of a wing (Jeffrey et al. 2000). This flap is most famously used to increase downforce on an inverted wing for racing applications, but has been a subject of several recent investigations on delta wings and reverse delta wing planforms as a means for lift augmentation.

1.2 STUDY MOTIVATION

There exists strong incentives to further research and development of Lippisch type WIG craft, as the reverse delta wing maintains pitch stability throughout the flight envelope without the significant weight and structural penalties of the large tailplane of the Ekranoplan-type WIG craft. The pitch stability achieved through the near constant pressure distribution on the lower surface of the reverse delta wing which leads to a significant advantage in the smaller sizing of the air/marine craft, evidenced by the use of Lippisch type craft as small passenger ferries or personal vehicles. Despite the economic advantage purported by WIG craft, and the Lippisch- type craft in particular, these craft remain in an experimental development phase, and the available aerodynamic research, either experimental or computational in nature, is limited. One key area of research is to augment the lift capabilities of the reverse delta wing using passive control mechanisms to increase the lifting capacity of the Lippisch-type WIG craft. The advantageous aerodynamic efficiency of WIG craft and the stability of the Lippisch-type planform necessitates a need for thorough research into reverse delta wings with various configurations. This study in part addresses this research gap by experimentally investigating the incorporation of passive control on a reverse delta wing in ground effect.

CHAPTER 2

LITERATURE SURVEY

This section will detail the relevant literature to this study, beginning with a description and review of ground effect. This will be followed by a general review of publications related to delta wings, a summary of reverse delta wings, and conclude with a review of literature on Gurney flaps, and Gurney flap-like strips.

2.1 GROUND EFFECT

An airfoil or wing flying within close proximity to the ground experiences favourable aerodynamic characteristics. As altitude is decreased, the dividing streamline moves rearward, leading to higher pressure flow on the lower surface, and accelerated flow at the leading-edge of the upper surface, resulting in a modified suction pressure distribution and a higher suction peak. The high pressure air beneath the wing acts as a dynamic air cushion. As ground clearance is further reduced, the flow underneath the lifting body may stagnate, leading to a large increase in pressure, known as RAM pressure. Further modifications to the flowfield in ground effect result from the restriction of the downwash, reducing the lift-induced drag, and from ground viscous dissipation and mirror effects increasing the effective span of the wing by pushing out the tip vortices. Further reductions in lift-induced drag result from the interaction of the tip-vortices with the ground. As a result of the increased lift force and decreased drag, the lifting body experiences a subsequent improvement in its aerodynamic efficiency, characterized as the lift-to-drag ratio, L/D, for steady-flight. Vehicles operating in ground effect may be referred to as Wing-in-Ground effect (WIG) craft. Several reviews of ground effect and WIG craft have been published, see for example the the reviews of Halloran and O'Meara (1999), Ollila (1980), and Rozhdestvensky (2006). These reviews, and prior research into ground effect has primarily been focused on Ekranoplan type WIG craft, rather than the Lippisch-type, due to the dominance of the Ekranoplan in Soviet military WIG craft and minimal academic or industry research into the reverse delta wing in ground effect. The stability of Ekranoplan wings in ground effect is however compromised by poor static longitudinal stability, resulting from a shifting center of pressure with ground proximity. In addition to aircraft, ground effect has also been investigated, both computationally and with limited experimental validation, as a possible means of providing aero-levitation for high speed train/rail transport systems, particularly by Cho et al. (2001), Han et al. (2005), and Moon et al. (2005). Extensive investigations have focused on the aerodynamic characteristics and flowfields of airfoils and wings with symmetrical and cambered profiles, in relation to both the development of WIG vehicles and racing car vehicles. While much early research encompassed the effects on two-dimensional flows such as that of airfoils (see Chen and Schweikhard 1985; Nuhait and Zedan 1993; Ranzenbach and Barlow 1994; Ranzenbach and Barlow 1996), numerous recent studies have incorporated three-dimensional wings and the characterization of whole flowfields and tip-vortex effects (such as Zhang and Zerihan 2003b, and Luo and Chen 2012). Extensive further research has been performed on inverted wings in ground effect, particularly in high-lift configurations. Research into delta wing planforms in ground effect is limited, and much more so for reverse delta wings, and will be discussed in Sections 2.2.2 and 2.3.2.

Pressure distributions and direct measurement of lift and drag forces using a force balance of both a symmetrical NACA 0015 airfoil and cambered NACA 4412 airfoil were obtained by Ahmed and Sharma (2005) and Ahmed et al. (2007) using a moving ground and the symmetrical and cambered airfoils, respectively. These investigators found an increase in upper surface suction with reducing ground clearance for the symmetrical airfoil, but decreasing suction for the cambered airfoil. While the drag coefficient for the cambered airfoil increased with increasing ground proximity, mostly as a result of a modified pressure distribution on the lower surface, the drag force on the symmetrical airfoil remained significantly more constant with decreasing ground clearance. For both airfoils, a large increase in the coefficient of pressure was observed on the lower surface, with the high pressure region extending to the trailing edge at higher angles of attack. An increased adverse pressure gradient was found from the pressure distribution measurements, indicating increasing wake size with ground proximity resulting from a promotion of flow separation on the upper surface. Notably, at a low angle of attack, in extreme ground effect, a converging-diverging passage is formed by the airfoil geometry resulting in suction pressure and a force reduction. The existence of this passage, and the induced height instability resulting from this phenomenon was confirmed by Luo and Chen (2012) on a NACA 0015 in ground effect with a static ground plane. A modified airfoil shape with a flatter bottom surface, a S-shaped airfoil, is suggested to minimize this force reduction. Further load-cell measurements by Luo and Chen (2012) found lift-curve slope dependency on ground proximity. Pressure measurements found a ramming effect, or local increase in surface pressure, for a certain range of incidence angles and ground proximities, however, pressure measurements by these authors are of limited use, due to the small number of pressure taps on the upper and lower surfaces.

Smoke trace tests performed by Jung et al. (2008) on a rectangular wing with NACA 6409 cross-section found tip vortex reduction in ground effect. A dynamometer test demonstrated increased aerodynamic efficiency from increased lift and decreased drag with decreasing ground clearance. The addition of endplates was found advantageous to increase ground effect. In a series of tests at the Marine Technology Center in Malaysia, Jamei et al. (2012) and Jamei et al. (2014) investigated a compound wing with the NACA 6409 cross-section, finding that similarly, placing the wing-tips closer to the ground through the use of anhedral had the effect of tip vortex reduction, further improving aerodynamic efficiency in ground effect. Little exploration of this flow phenomenon was performed, with only 6-axis force balance measurement results reported. Lee et al. (2010) solved the Reynolds-Averaged Navier-Stokes (RANS) equations on several wing-in-ground effect configurations using the Glenn Martin 21 airfoil cross-section, with varying anhedral angle and endplates. These investigators found that high pressure air is trapped beneath the wing when equipped with endplates in ground effect, as well as confirming a tip vortex reduction, thus augmenting lift and aerodynamic efficiency. Anhedral, on the other hand, was found to be more stable than the baseline wing in ground effect, albeit providing a lower lift-to-drag ratio increment than the endplate modification. Limited ground clearances were tested (10%-30% of root chord), and further mesh refinement may be necessary to resolvethe detailed flow characteristics.

Researchers at the University of Southampton (Zerihan and Zhang 2000, 2001; Zhang and Zerihan 2003a, 2003a, 2003b) investigated the aerodynamics of single and multiple element (high-lift configuration) inverted wings in ground effect, using a modified Tyrell 026 Formula 1 car front wing with endplates (modified NASA GA(W) profile, type LS(1)-0413). Force balance measurements and surface pressure measurements conducted with a rolling ground, at chord Reynolds numbers of $Re = 0.45 \times 10^5$ and $Re = 7.35 - 7.65 \times 10^5$ for the single element and multi-element configurations, respectively, found an increase in down-force with increasing ground proximity. A force reduction was observed at low ground proximities when the wing stalled due to boundary-layer separation at the trailing edge. The effect of transition fixing was found to be significant in this regard. Off-surface measurements performed using laser Doppler anemometry (LDA) and PIV found a turned wake with increasing ground proximity, due to boundary layer separation on the suction surface increasing the size of the turbulent wake. Earlier investigators hypothesized that boundary-layer merging may be responsible for a sudden stall of the airfoil (see Ranzenbach and Barlow 1994; Ranzenbach and Barlow 1996); the pressure distribution and moving ground boundary layer thickness found by the University of Southampton researchers dispute this assertion. Recently, Roberts et al. (2016) demonstrated Reynolds number dependency on the aerodynamic characteristics of the single element wing, while the multi-element and complex Formula-1 high-lift wing had reduced dependency. Using a rolling road facility and 6-component force balance, Roberts et al. (2016) found that the three tested models all featured distinct laminar separation bubbles, with size and location dependency on Reynolds number and ground proximity. With both decreasing ground clearance and Reynolds number, flow separation is promoted, from lower energy and greater viscous effects in the case of the Reynolds number, and an increased adverse pressure gradient with decreasing ground clearance.

2.2 DELTA WINGS

Delta wings have been extensively investigated for use in supersonic flight, due to their sharp leading edge and high sweep reducing drag in supersonic flight. Additionally, the low aspect ratio of delta wings allow for the greater manoeuvrability required by military fighters at high speeds. When landing and taking off, delta wings suffer from low lift-to-drag ratios and lift-curve slopes at the typical angles of attack used by rectangular wings. However, at moderate angles of attack, the flowfield of delta wings is characterized by a stable pair of nearly axisymmetric counter-rotating streamwise vortices, developed from the roll-up of the leading edge shear layer, and subsequent streamwise reattachment of these shear layers in the chordwise direction. These two high energy leading-edge vortices (LEV) provide non-linear vortex lift, increasing the static stall angle significantly. However, these leading-edge vortices are susceptible to breakdown over the wing with a further increase in the angle of attack, lowering lift and increasing drag force while inducing pitching and rolling moments which may compromise the stability of the aircraft, alongside undesirable unsteady effects and phenomena. Extensive research has been conducted into the vortex structure of LEVs and the flowfield of delta wings. Particularly, research has been focused on slender delta wings (sweepback angle greater than 55°) due to the wave-drag benefits afforded by their low-aspect ratio. In this present work, the delta wing is used as a means of comparison for the reverse delta wing, so a brief discussion of the flow and aerodynamic characteristics of delta wings will be reviewed. The research relating to slender and non-slender delta wings will first be covered, followed by a discussion of literature on delta wings in ground effect.

2.2.1 Delta Wings Outside of Ground Effect

Subsonic flow over delta wings is dominated by leading edge vortices, which are characterized by several distinct features. The primary vortex forms from the roll-up of the separated shear layer originating at the leading edge. The shear layer re-attaches along an attachment streamline, forming an attached primary vortex. A counter-rotating secondary vortex is formed from the separation of the spanwise flow induced by the primary vortex, forming outboard of the primary attachment line and underneath the primary vortex. Similarly, a tertiary vortex may form from the adverse pressure gradient causing spanwise secondary flow separation of the attached shear layer. A diagram of these vortices is presented in Figure 2.1 (a). On slender delta wings, the primary vortex structure is largely independent of Reynolds number (i.e. an inviscid phenomena) given sufficiently thin wings with separation fixed at a sharp leading-edge and sufficiently large Reynolds number to have a large magnitude of difference between the scale of the vorticity convection and diffusion, among other qualifications. A rounded leading-edge may however delay the formation of the leading-edge vortices from a delayed onset of flow separation (Lee and Ho 1990). The secondary and tertiary vortices are the result of boundary-layer separation, and are thus viscosity dominated in nature. The main effect of the secondary vortex is to displace the primary vortex inboard and upward, with increasing displacement with increasing Reynolds number. The primary vortex itself is composed of three regions, as shown in Figure 2.1 (b). The exceptional thesis work of Payne (1987), using Laser Doppler Anemometry (LDA) coupled with seven hole-pressure probe measurements and smoke-wire flow visualization, demonstrates the secondary vortical structures resulting from Kelvin-Helmholtz instabilities in the separated shear layer superimposed on the vortex, which feed vorticity into the vortex core. The thickness of the shear layer thus increases in the chordwise direction. The rotational core inside the shear layer, with a diameter of approximately 30% local semi-span, has a near continuous distribution of vorticity. A viscous subcore is found at the center of the vortical flow structure, where large gradients of velocity and pressure are observed. The viscous subcore, approximately 5% of the local semi-span in diameter, rotates as a solid body, with a diameter determined by the distance between peak tangential velocities (Nelson and Pelletier 2003)). Using crosswire measurements, Visser and Nelson (1993) found subcore axial velocities up to 2.5 times in excess of freestream, later confirmed via non-intrusive methods by other authors (Ol and Gharib 2003). Before breakdown, the leading-edge vortex may be represented as a superposition of a jet-flow and vortical flow.

Surface pressure suction peaks arise under the primary vortex cores, and the flow is further accelerated over the vortical flow structure, resulting in the vortex lift associated with delta wings, with this non-linear lift dominating the lift generation at moderate to high angles of attack until stalling at a significantly higher incidence than rectangular wings. The stalling of the delta wing is induced by the breakdown of these LEVs over the delta wing leading to fully separated flow over the upper wing surface. Vortex breakdown is the sudden divergence, disorganization or expansion of the vortex core diameter, and stagnation of the axial velocity and increase in dynamic pressure, resulting in a wake-like core post-breakdown (jet-like core before breakdown) and in some cases, axial flow reversal. With breakdown, the vortex fails to reattach, becoming incoherent and resulting in a turbulent flow, with breakdown location propagating upstream with increasing angle of attack and decreasing sweep angle until reaching the delta wing apex (Kohlman and W. H. Wentz 1971). The pressure gradient along the vortex axis plays a significant role in breakdown, with an increasingly adverse pressure gradient promoting the breakdown location. Before breakdown, the velocity field of the leading-edge vortex may be approximated by a swirling jet flow, with increasing wing incidence resulting in an increase in maximum axial velocity and peak tangential velocities, being up to three times freestream and 1.5 times freestream prior to breakdown, respectively. Post-breakdown, the tangential velocity is reduced with the peak value reduced to freestream, and the vortex subcore dilates, diffuses and becomes bulbous, growing in size from approximately 10% of the local semi-span to nearly 50% (Nelson and Pelletier 2003).

Vortex breakdown, first observed in the 1950's by Henri Werlé (Mitchell and Délery 2001), significantly alters the surface pressure distribution thus changing the forces and moments on the wing, and causing uncommanded responses in delta wing aircraft, limiting the effective manoeuvrability of such craft(Peake and Tobak 1983). Large bodies of work are dedicated to investigating vortex breakdown, however, the accurate prediction of vortex breakdown and the lift characteristics of the delta wing with an onboard vortex breakdown location remain elusive. The vortex size and breakdown are considered to be controlled through inviscid mechanisms (Lee and Ho 1990). However, several factors in addition to sweep and incidence angle have been found to affect vortex breakdown. Suction and blowing have been found to be effective in delaying vortex breakdown, while flap deployment and acceleration may push the breakdown location upstream (Gursul et al. 2007). Model thickness and leading edge geometry affect vortex breakdown position. Lowson and Riley (1995) replicated results from numerous investigators, finding geometry of the wing to be of critical importance in determining vortex breakdown location, specifically the apex geometry, while Reynolds number and tunnel effects/support-body interference proved to be of minor importance. A systematic experimental investigation by Kohlman and W. H. Wentz (1971), using slender sharp-edged delta wings with sweep angles varying from 45-85 degrees, found trailing edge geometry to have little impact on the vortex breakdown location. This is in addition to shear layer instabilities and cropping (of wing tips) (Payne 1987). Extremely slender delta wings may result in contact between the primary vortices, reducing vortical lift and inducing breakdown by preventing complete flow reattachment. Vortex breakdown on non-slender delta wings, here considered for wings with sweep angles below $\Lambda = 55°$, will be discussed below. The breakdown of LEVs was been found to take two forms by Lambourne and Bryer (1961) in early low-speed tests on flat plate delta wings, with these forms later hypothesized as two extremes on a continuum with flow conditions downstream of breakdown influencing the type of breakdown observed. The bubble type breakdown is seen as a stagnation point in the axial flow along the vortex axis around which the diverting streamlines form a flow structure similar to flow around a spherical half-body. Flow over the fore half is smooth and symmetric, while flow over the aft portion is irregular with vortex shedding as seen in flow around blunt bodies. The second breakdown form is the spiral type, where the core vortical flow forms a kink from a rapid deceleration, leading to a spiral-like flow which ultimately dissipates into large scale turbulence (Payne et al. 1988). Details on vortex breakdown on slender delta wings can be seen in the thorough work of Delery (1994). Still images from dye flow visualization of the two vortex breakdown types can be seen in Figure 2.1 (c).

Many attempts have been made to develop analytical solutions to predict vortex breakdown location and its impact on aerodynamic forces. Vortex breakdown has been found to be primarily influenced by the adverse pressure gradient and the swirl parameter (ratio of circumferential velocity to axial velocity), with several authors proposing that a critical swirl parameter of 1.12-1.41 (helix angle of 50°) as a necessary condition for breakdown (see Mitchell and Délery 2001). The conditions necessary for breakdown are thus determined by the interplay of vorticity convection and diffusion, with a change in this balance resulting in vortex expansion and a dynamic pressure rise coupled with axial flow deceleration. Theories of vortex breakdown fall into four dominant categories, although the full application and acceptance of these theories remains limited. These four classes of theories are a quasi-cylindrical approach, solution of the Navier Stokes equations, a critical state or critical swirl ratio, and hydrodynamic instabilities (Delery 1994).

For the leading-edge vortex to be stationary, Lee and Ho (1990) determined that a balance in the vorticity convection in the freestream and generation of vorticity from the wing surface shear layer must be developed, with the swirl angle being a measure of this balance. An adverse pressure gradient reduces the axial convection of vorticity, thus altering the balance and inducing vortex breakdown. Nelson and Visser (1990), using experimental x-wire measurements on slender delta wings, at selected angles of attack of 20° and 30°, measured the axial and azimuthal vorticity distributions. These authors found a circulation distribution which could be scaled by the local semi-span, growing linearly in the chordwise direction. The maximum vorticity was found at the location just preceding breakdown, with the maximum azimuthal vorticity remaining relatively constant upstream of breakdown, and becoming negative in the breakdown region. The development of the negative azimuthal vorticity is thus a further indication of the vortex breakdown location. Alternatively, given flow-field measurements, the measurement of bound circulation may provide an estimate of the lift-force through the Kutta-Jowkowski theorem, using the vortex span between leading-edge vortex core locations rather than the wing-span. In lieu of analytical closed form solutions, empirical relations or numerical computations may be used, however, vortex breakdown location is strongly dependant on minor geometric model details such as thickness, bevel, leading-edge radius, among others, as demonstrated by Jobe (2004). Jobe (2004) through a comprehensive review of 38 datasets of 65-degree swept delta wings compared alongside four empirical vortex breakdown location prediction methods and two Navier-Stokes computations, found the tested empirical methods to be insufficient and the Navier-Stokes methods to be effective for laminar flows only.

The non-linear lift generated by a delta wing, while the flow remains attached, and before vortex breakdown reaches the trailing edge, can be decomposed into two components, the potential flow lift and vortex lift. Several models exist for prediction of the vortex lift and characteristics, including Euler Equation methods, Navier-Stokes Equations at low Reynolds number ($< 10,000$), and a vortex lattice potential flow method (Payne 1987). Polhamus (1971) developed a leading-edge suction analogy to predict the lift and drag forces, resulting in the formulation of the following expression, where K_p and K_v are the potential flow lift and vortex lift constants, determined from correct application of potential flow lifting-surface theory, geometric boundary conditions, and a Kutta-type condition applied at the leading-edge:

$$C_L = K_p \cos^2(\alpha)\sin(\alpha) - K_v \sin^2(\alpha)\cos(\alpha) \tag{2.1}$$

For low to moderate angles of attack, such as those typical in most aircraft flight applications, this theory is sufficient to predict the aerodynamic lift and lift-induced-drag for delta wings while neglecting flowfield details, and assuming fully attached flow over the range of angles of attack considered with no vortex breakdown over the wing.

As described prior, non-slender delta wings (sweep angle, $\Lambda < 55°$) have a higher lift-curve slope relative to slender delta wings, courtesy of lift-curve slope dependency on sweep angle. Major variations are found in relation to non-slender delta wings as compared to their slender counterparts. The leading-edge vortices form at very low incidence and close to the wing surface, resulting in a strong interaction between the leading-edge vortices and the boundary-layer, with a dependence on Reynolds number in regards to the vortical flow parameters. The vortex breakdown over the delta wing begins at a much lower angle of attack, and is less abrupt than that of the slender delta wing. The vortex breakdown instead is of a shallow, conical form, resulting in a vortex breakdown region instead of a more precise chordwise location (Gursul et al. 2005). Contrary to the slender wing, the non-slender vortical flow is characterized by a dual primary vortex structure at low incidence, arising from the primary shear layer interaction with the secondary spanwise flow, which then splits into two primary vortices of the same vorticity sign. The attachment line is outboard of the wing centerline (symmetry plane), moving towards the centerline with increasing angle of attack, with streamlines forming the limiting case between the two attachment lines being approximately aligned to the original freestream direction. With an increase in angle of attack, the primary vortex becomes more prominent, moving inboard and away from the wing surface while the second primary vortex remains embedded in the separated shear layer (Gursul et al. 2005). Further increases in the angle of attack lead to the vortical structure resembling that of the slender delta wing. However, as a result of the interaction with the boundary-layer, the non-slender delta wing has a lower maximum lift coefficient and static stall angle than the slender delta wing (Gursul et al. 2005). Notably, with the non-linear vortex lift being dependant on the sweep angle, with a decrease in the sweep angle, the lift contribution from the vortical flow structure is lowered, and thus the onset of vortex breakdown (change in $C_L - \alpha$) is not clearly identifiable from force data (Gursul et al. 2007). Stereoscopic digital PIV results obtained at a low Reynolds number by Ol and Gharib (2003) found coherent leading-edge vortices even at low angles of attack not explored by previous authors (such as at 2.5°).

Several unsteady phenomena occur in the flow over slender delta wings, including shear layer instabilities, vortex interactions, vortex shedding, vortex wandering, and helical mode instabilities, which all play roles in the buffeting of slender delta wings (Gursul et al. (2005)). The vortex breakdown behavior itself is unsteady in nature, with significant variations in the chordwise vortex breakdown location, up to 10% chord for slender delta wings, and 40-50% for non-slender delta wings. Menke et al. (1999) investigated the characteristic time scales of the unsteady breakdown location and unsteady flow phenomena over the delta wing. Fluctuations in breakdown location consisted of quasi-periodic oscillations as well as high-frequency low amplitude displacements. The quasi-periodic oscillations result from the antisymmetric motion of breakdown arising from interactions between the primary vortical structures. A splitter plate placed on the centerline of the wing by Menke et al. (1999) suppressed these oscillations, with the effects explored using Laser Doppler Velocimetry (LDV) on delta wing models with sweep angles of 65° to 75° at Reynolds numbers ranging from 41,000 to 54,000. These investigators hypothesized that crossflow instabilities and streamwise instabilities are two mechanisms responsible for the interaction between the leading-edge vortices resulting in the unsteady location of the vortex breakdown.

Vortex control and lift enhancement and drag reduction methods have been investigated and proposed by numerous investigators. Dihedral (or anhedral) is primarily implemented for roll stability (or instability) and thus the effect of anhedral and dihedral on lift augmentation was investigated by Traub (2000) on a 75-degree delta wing. Using various experimental methods, this investigator found the primary impact of anhedral and dihedral to be to alter the LEV trajectory, bringing the vortex core towards the wing surface. Anhedral resulted in inboard movement and an increase in lift, while dihedral resulted in decreased lift and outboard vortex movement. Traub (2000) suggested that the anhedral did not significantly affect LEV strength, instead lift augmentation resulted from induced surface loading on an increased wing area from the altered vortex trajectory. Vess et al. (1986) performed an exploratory investigation with pressure surveys and flow visualization on the impact of apex fence deployment on delta wings. These investigators, with limited quantitative data (only 3 spanwise stations), found increased suction on the leeward wing surface. Buchholz and Tso (2000) furthered these findings through a comprehensive investigation, determining that the apex fences worked to trap the primary vortices on the suction surface, adding thickness and camber. A penalty of promoted vortex bursting with fence deployment was suggested, with a reduced lift-to-drag ratio observed. The impact of Gurney flaps for lift augmentation will be discussed below in Section 2.4. As an alternative to lift augmentation, drag reduction was achieved by Li and Wang (2003) by employing riblets on a low-sweep delta wing. Finally, flow control techniques of leading-edge vortices was reviewed by Gursul et al. (2007) and Mitchell and Délery (2001). Succinctly summarized, streamwise momentum injection (decreasing the swirl parameter) or a reduction of the adverse pressure gradient (via control surfaces, flexible wings, suction, etc.) may possibly be used to control or delay vortex breakdown.

Further detailed discussion of vortex flow and breakdown over delta wings can be found in the thesis work of Dogar (2012) and Ko (2017) and Pereira (2011).

2.2.2 Delta Wings Inside of Ground Effect

Research into delta wings in ground effect is much more limited than conventional wings and airfoils. Research is primarily limited to the impact on landing and take-off, particularly at high angles of attack to allow for short field take-off and landing (STOL) for military aircraft operating off the flight deck of an aircraft carrier. Experimental research and data can be found in Katz and Levin (1984), Lee et al. (1987), and Lee et al. (1989), with flight tests conducted at constant angles of attack (CAA) as reported by Schweikhard (1967), Baker et al. (1970), and Curry and Ownes (2003). The flight tests and experimental wind tunnel tests found lift increments obtained in ground effect. However, detailed flow-field investigations and comprehensive investigations of the phenomenon are limited, with prior research focused on aerodynamic loading and wing configurations.

Qu et al. (2015), Qin et al. (2015), and Qin et al. (2016) employed numerical investigations, using RANS and Delayed Detached Eddy Simulation (DDES) to investigate a 65-degree sweep sharp leading edge delta wing (VFE-2 model) in static and dynamic ground effect. The dynamic ground effect was characterized by adding a sink rate to the wing to simulate the landing performance of a delta wing aircraft. These investigators found that the lift, drag, and nose-down pitching moment increased with increasing ground proximity, with the major contributor being from the lower pressure surface, though the primary lift generation and drag production was still from the leading-edge vortices. A notable difference between the regular wing and the delta wing in ground effect is that the drag for the delta wing increased in ground effect. The pressure distribution obtained on the lower surface demonstrated global flow deceleration on the lower surface, with a spanwise flow component introduced and local acceleration around the leading-edge on the lower surface. The leading-edge vortices were strengthened in ground effect, with an acceleration of the axial core velocity in the leading-edge vortex before the vortex breakdown, and greater flow deceleration after vortex breakdown than the out of ground effect case. The introduction of dynamic ground effect was found to add a compression work effect at low ground clearances, further increasing pressure on the lower surface with little consequence on the vortical flow over-top of the delta wing. As a result of this increase in pressure, dynamic ground effect was found to further increase lift, drag, and nose-down pitching moment on the wing. Qu et al., Qin et al. (2015) and Qin et al. (2016), however used RANS and DDES on the ANSYS Fluent solver for the above-presented results, with minimal experimental validation. Limited data presented by Lee et al. (1989) found that in ground effect, the LEVs are strengthened but located further outboard, with flow visualization validating the expanded vortex core observed by Qu et al. (2015). However, measured force increments were reduced in the dynamic case, in contrast to Qin et al. (2016). An increase in sink rate may induce a lag in the vortex position relative to the wing surface, thus decreasing the lift coefficient.

2.3 REVERSE DELTA WINGS

2.3.1 Reverse Delta Wings Outside of Ground Effect

Investigations into delta wings and reverse delta wings began in earnest near the end of the first half of the 20th century, stemming from an extension of swept wings, such as the X-29, to fully deltoid planforms. A research memorandum from NACA, published in

1947, details an early experimental investigation into triangular planforms, with both swept-forward and swept-back wings with an aspect ratio of 2, tested at a Mach number of 1.53 and $Re = 7.5 \times 10^5$ (Vincenti et al. 1947). While the results are of limited use given that the accuracy of the presented results is disputable due to support-body interference and as the models were tested only to a 10° angle of attack, these investigators found a lower minimum drag of the reverse delta wing planform with a loss of leading-edge suction as compared to the delta wing. The lower minimum drag (at supersonic speeds) is due to the long runs of natural laminar flow achievable on the reverse delta wing, afforded by the unique geometry of the reverse delta wing. The receding width of the reverse delta wing avoids the attachment line and cross-flow instabilities (primary modes of transition) found in swept-wings. As the percent area as a function of chord is highest at the fore of the wing (i.e., 20% of the wing area is covered by a 10% chord run, 50% wing area at 30% chord run), the reverse delta wing minimizes skin friction drag as compared to the delta wing given that laminar boundary layer flow can be maintained over a larger portion of the wing surface.

The advantage of large laminar flow runs was exploited by Gibson and Gerhardt (1995), who proposed a supersonic transport (SST) using the reverse delta wing planform. The design was postulated from the application of the reciprocal flow theorem (see Flax 1949), wherein at sufficiently high Mach numbers, with the wing immersed in supersonic flow and the Mach wave behind the leading edge, the zero lift wave drag, lift-curve slope and induced drag are equal for forward and reverse flows given interchanged leading and trailing edges for a given wing. Gibson and Gerhardt (1995) performed subsonic wind tunnel testing on a variety of leading- and trailing-edge flap configurations (aspect ratio of 2, $Re = 1.4 \times 10^6$), and used inviscid Euler calculations to obtain chordwise pressure distributions for subsonic and supersonic flight conditions. Their results showed strong pressure gradients being confined to the trailing edge region of the reverse delta wing, as compared to the leading-edge region of the regular delta wing. At subsonic speeds, the lift-curve slope was independent of flow direction until the onset of flow separation. For the same lift coefficient, C_L, the drag coefficient, C_D, was found to be higher for the reverse flow case. Based on these results, Gerhardt (1996) patented this design on behalf of Northrop Grumman, incorporating varying combinations of trailing edge and leading edge flaps, as well as several proposed laminar flow control methods. The trailing edge flaps with swept hinge-lines could achieve large deflections before stall, with marked improvement in C_L, while drag reduction was achieved with leading-edge flaps. Due to the need for minimizing supersonic aircraft noise during takeoff and landing to allow for broader appeal of civil supersonic transports, a variation of this design was produced by Northrop Grumman for the NASA High Speed Research

Program, noting that the reverse delta wing planform achieved additional lift at low speeds (such as at takeoff and landing), reducing power requirements and thus noise (Norris 1998). Spanwise wing extensions were incorporated to make further use of the large percent area extent of laminar flow at the fore of the reverse delta wing.

Altaf et al. (2011) investigated the reverse delta wing as compared to a regular delta wing, using particle imaging velocimetry (PIV) in a low-speed tunnel to explore the vortical flowfield of a 75-degree sweep, 20-degree beveled reverse delta wing at a chord-Reynolds number of 3.82×10^5. These investigators found that, at the normalized streamwise coordinate of $x/c = 1.359$ and 3.418, the tangential velocity and vorticity of the delta wing was higher than the reverse delta wing at a particular angle of attack. Streamlines from Altaf et al. (2011) are presented in Figure 2.2. The vortex core size and circulation was found to increase with increasing angle of attack, with force balance measurements from a six-component force balance determining that the lift (or drag) of the delta wing was higher (or lower) than that of its reverse, although the lift-to-drag ratio of the delta wing was exceeded by the reverse case. Pressure distributions obtained via CFD computations found pressure gradients in agreement with Gibson and Gerhardt (1995).

The aerodynamics and vortical flowfield of a reverse delta wing was further explored by Lee and Ko (2016a), Lee and Ko (2016b), and Lee et al. (2017). Lee and Ko (2016a) investigated the streamwise structure and vortical flowfield generated by a slender reverse delta wing, for $0.1 \leq x/c \leq 1.5$ and $\alpha = 4° - 30°$, using PIV supplemented by force balance measurements and flow visualization. The reverse delta wing vortices, originating from the roll-up of the spanwise leading-edge vortex, were found to be located outboard and above the wing surface and characterized by an "arm-and-fist" flow pattern, with the arm and vortex growing with increasing chordwise station. In contrast to the delta wing, the reverse delta wing total circulation reached a local maximum at $x/c = 0.7$ at which point it became insensitive to x/c, as well, for $\alpha = 10°$, roll-up of the reverse delta wing vortex was completed by $x/c = 0.7$. Peak vorticity and tangential velocity occurred at $x/c = 0.3$, implying a spanwise leading-edge vortex filament diameter of 0.3c. Multiple spanwise vortex filaments (SVF), arising from the spanwise leading-edge vortex filament from the roll-up of the lower-wall shear layer at the leading edge, were identified for $\alpha < 14°$. At $\alpha = 20°$, the aft most SVF was found to be disrupted from their inherent instability and interaction with three dimensional flow arising from the trailing edges and the boundary layer flow. Further increases in incidence led to a large separated flow over the upper surface and diffusion of the reverse delta wing vortex.

The upper surface of the reverse delta wing thus does not contribute to lift beyond the attached potential flow regime, with the primary lift generation resulting from pressurization of the windward surface. The disruption of the reverse delta wings is benign in regards to the aerodynamic characteristics of the wing due to their outboard nature, as opposed to the significant vortex lift and drag generated by the leading-edge vortices of the delta wing.

Lee and Ko (2016b) further explored the impact of non-slenderness on the vortical flowfield and aerodynamic characteristics of a reverse delta wing, comparing a 50-degree sweep reverse delta wing against a regular 50-degree sweep delta wing and their slender 65-degree sweep counterparts. Force balance measurements revealed that relative to the non-slender delta wing, the non-slender reverse delta wing had higher C_L for $\alpha \leq 10^\circ$, then plateauing and gradually increasing to a static stall angle of 24°. A monotonic drag increase was observed with increasing angle of attack. These force balance measurements were coupled with flowfield measurements using PIV at $Re = 11,000$ to determine that the non-slender RDW vortex was located more outboard and further above wing surface, with a lower peak tangential velocity and vorticity, and became disorganized or diffused at a lower angle of attack ($\alpha = 16^\circ$) relative to the slender RDW. At angles of incidence exceeding $\alpha = 18^\circ$, a weak circulation-like flow with small patches of vorticity was observed, which occurred at $\alpha = 24^\circ$ for the slender case, resulting from interactions between the separated flow over the wing upper surface and the RDW vortex. This further suggests irrelevance of the RDW vortices in the wing stalling mechanism. Instead, the stalling of the reverse delta wing is due to the breakdown of the multiple spanwise vortex filaments on the wings upper surface, with this disruption or loss of coherence occurring earlier with a reduction in the sweep angle.

While the use of dihedral is common on low rectangular wings in conventional aircraft for roll stability, and anhedral is used to induce instability for greater manoeuvrability in some supermanoeuvrable fighter aircraft and high-wing configurations, some Lippisch-type WIG craft use anhedral tips to reduce hydrodynamic drag and to form a so-called "air tunnel" in the cavity between the wing and the ground. The freestream aerodynamic impact of anhedral on the reverse delta wing was explored by Lee et al. (2017), who investigated the impact of anhedral on aerodynamic forces and the vortical flowfield of the reverse delta wing. At a $Re = 4.06 \times 10^5$, force balance measurements found that for the same lift condition, with increasing anhedral the drag coefficient increased, and the addition of anhedral led to decreased aerodynamic efficiency and lift production. From PIV measurements, the investigators found an increasingly inboard and upward movement of the RDW vortices with increasing anhedral, though these vortices had increased vorticity and tangential velocity relative to the planar wing, leading to a more well-defined and concentrated vortex at a higher incidence angle.

Recently, reverse delta wings have been investigated as a means of wing-tip vortex alleviation. The impact of the downwash and turbulence generated by a leading aircraft's wing-tip vortices severely impacts airport takeoff rates, as well as the wing-tip vortices producing undesirable lift-induced drag. Lee and Su (2012) performed 7-hole pressure probe measurements on a NACA 0012 wing with a full chord slender reverse half delta wing (RHDW) mounted on the squared tip, finding a weaker tip-vortex with lower vorticity may be achieved through the use of the RHDW, reducing the lift-induced drag. However, this reduction is coupled with increased separated wake flow and a profile drag penalty from the increased wing area, with little change in total drag. For the same lift condition as the clean wing, the RHDW equipped wing had the same drag coefficient, thus demonstrating feasibility of the use of the reverse delta wing in wing-tip vortex alleviation.

Lee and Pereira (2013) further considered the impact of oscillation on the passive control of the wing-tip vortex, using a full chord half delta wing (HDW) and RHDW. Hot-wire anemometry was used on a NACA 0012 wing oscillating at a reduced frequency of $\kappa = 0.09$. While the HDW induced vortex breakdown and diffused the tip vortex, the RHDW equipped wing-tip vortex remained concentrated, albeit with reduced strength and extent. Outboard vortex displacement relative to the baseline wing was observed in both configurations, though the RHDW vortex was much more greatly displaced upward, indicating viability as a means for avoidance of blade-vortex interaction in rotating blades (such as a helicopter rotor blades). From these promising results, various HDW wing configurations were further considered by Lee and Choi (2015), with varied slenderness, deflection and root chord lengths tested. A non-slender, reduced root chord half-delta wing improved the degree of diffusion, and demonstrates the use of small chord HDWs for wing-tip vortex alleviation while minimizing weight and structural penalties.

In contrast to the tip-mounted delta wings and reverse delta wings employed by these investigators, Altaf et al. (2016) used a full 69-degree sweep reverse delta wing as a wake vortex alleviation add-on to a NACA 23012 half-span wing. The reverse delta wing was mounted on top of the wing at the tip, at an angle of incidence of 30°. Similar to the tip-mounted case, the add-on explored by Altaf et al. (2016) reduced the tangential velocity, vorticity levels, and circulation of the wing-tip vortex, as determined by PIV measurements, with mostly benign aerodynamic characteristic changes noted from force-balance measurements supplementing the vortical flowfield investigation. A reduction in the aerodynamic efficiency relative to the baseline configuration was observed. Besides impacting the wing-tip rollup process due to partially blocking the flow from the lower surface to the upper surface at the wing-tip, the authors proposed that the vortex produced by the reverse delta wing interacts with the wing-tip vortex, exciting instabilities from counter-rotation and vortex co-rotation, modifying the roll-up accordingly to alleviate the hazard (Altaf et al. 2016).

2.3.2 Reverse Delta Wings Inside of Ground Effect

Little archived publications about reverse delta wings in ground effect are available, in spite of several current WIG craft utilizing the Lippisch-type planform. Urquhart et al. (2006) investigated a Lippisch-type WIG craft in ground effect using a representative model, with a static ground plane and three-component force balance. These investigators found an increase in the lift-to-drag ratio in ground effect due to the lift increase outweighing the observed drag increase. However, the model used had a cylindrical mounting strut with no aerodynamic fairing which contributed significantly to the measured drag. Improved experimental results were subsequently found by Musaj and Prince (2008), with a 5% scale model of the AVCEN Jetpod airtaxi wing, a forward- and backward-swept wing (W-shaped) with a NACA 2412 section (no twist). Musaj and Prince (2008), using a static ground plane with a three-component force balance, found a similar increase in the lift-to-drag ratio with increasing ground proximity, due to an increase in the lift coefficient and little variation in drag with reducing ground clearance. A static ground plane is disadvantageous as the boundary layer growth on the ground plane is not representative of typical atmospheric conditions (except for a strong headwind). Results at extreme ground proximity must thus be treated with caution due to boundary layer interference. Musaj and Prince (2008) used STARCCM CFD code, similar to Altaf et al. (2011), for a numerical investigation with the Wieselsberger method of images used for a symmetry plane boundary condition, confirming the dynamic air cushion generated underneath the WIG craft, as well as an increase in leading edge suction. An increment in spanwise flow was noted, suggesting an increase in effective span and thus a reduction in induced drag. An increased tendency for trailing edge separation was observed. Some near-wake numerical results were validated with horizontal pressure-rake measurements, but no detailed flowfield experimental measurements were obtained to validate the numerical pressure distribution and wake results, especially results obtained for the ground vortex development and boundary layer separation noted by the authors.

Beyond determining variable aerodynamic loading in ground effect, stability of aircraft must be evaluated and considered as well. Irodov (1974) developed a stability criterion for wing-in-ground effect for longitudinal static stability. The Irodov stability criterion for the longitudinal static stability of a lifting body operating in ground effect, asserts that the aerodynamic center of height (ACH) must be ahead the aerodynamic center of pressure (ACP) (Irodov 1974). Yang et al. (2009) compared representative configurations for the Lippisch-type and Ekranoplan-type WIG craft with numerical simulations, finding the reverse delta wing planform to be longitudinally statically stable in ground effect, with an optimal pressure distribution on the windward surface. The designers of the WSH-500, a prototype WIG craft, found inherent stability from sea-trials on their prototype vehicle (Lee et al. 2012). Prior flights of reverse delta wing WIG craft have been observed to be stable with increasing ground proximity, unlike the rectangular wing planforms (Ekranoplan-type WIG craft). Additionally, cambered wings may experience a negative lift (or suction) at close ground proximity due to a converging-diverging passage being created underneath the wing, further inducing an height instability in cambered rectangular wings. The longitudinal stability of a reverse delta wing with anhedral was computationally investigated by Wang et al. (2013), finding that an anhedraled wing operating in ground effect had upstream ACH movement and downstream ACP movement, improving stability. However Wang et al. (2013) did not provide supporting experimental evidence, and limited computational results.

No other published or archived publications on the reverse delta wing in ground effect are available, to the author's best knowledge.

2.4 PASSIVE CONTROL VIA GURNEY FLAPS OR GURNEY FLAP-LIKE STRIPS

While variations on the Gurney flap have been thought to be employed earlier, the premier application was by their namesake, Daniel Gurney, in the 1960's on racing car wings to increase downforce. Liebeck (1978) performed a canonical experimental study, finding a large lift increase with the application to a Newman airfoil, shifting the lift-curve upward and leftward. Liebeck (1978) suggested that the height of the flap be below 2% of the chord to reduce the impact on drag, and presented a hypothetical flow structure at the trailing edge of the airfoil equipped with a Gurney flap. That flow structure consisted of a downturned wake, with two counter-rotating vortices. A separated flow region was located upstream of the flap on the leeward surface. This hypothesized flow structure for Gurney flaps on rectangular wings has since been validated by numerous authors and widely accepted. A schematic of this flow structure is presented in Figure 2.3 (a). Since Liebeck (1978), Gurney flaps have been extensively studied and catalogued in typical rectangular wing configurations, and in a few cases, as lift enhancement on delta wings at subsonic speeds.

While the time averaged flow structure consists of the two counter-rotating vortices, the instantaneous flow structure may consist of a Kármán vortex street similar to flow past bluff bodies. A comprehensive study by Jeffrey et al. (2000) using spectral analysis through LDA coupled with smoke-wire flow visualization found a von Kármán vortex street at the trailing edge. This instantaneous flow structure of alternatively shed vortices, had Strouhal numbers of approximately 0.15 for 2% and 4% Gurney flaps. Time averaged results matched the prediction made by Liebeck (1978). Force measurements found the wing equipped with Gurney flaps had both sharper stall characteristics and stall promotion, however negligible alteration in the slope of the lift-curve was observed. Surface pressure measurements indicated that a reduction in separation (from trailing edge suction) at the trailing edge reduced pressure recovery requirements, thus extending the linear attached potential flow regime of the lift-curve, increasing the maximum lift coefficient. A further time resolved analysis via PIV was conducted by Troolin et al. (2006), finding two vortex shedding modes on a NACA 0015 airfoil equipped with a Gurney flap. The principal mode found was the von Kármán vortex street, with a secondary mode found to be a result of the shedding of the recirculating fluid in the area immediately upstream of the flap. From a comparison of the typical case and the configuration where this area is filled in, Troolin et al. (2006) suggested that the periodic expulsion of the vortex formed in the upstream cavity may be responsible for a portion of the lift increment resulting from Gurney flap application. Maughmer and Bramesfeld (2008) used surface-pressure distributions and an analysis of the wake-momentum deficit on a Gurney flap equipped airfoil, finding a linear relationship between Gurney flap height, chordwise location and the lift increment. Zerihan and Zhang (2001) found that by fitting a modified NASA GA(W) profile wing, type LS(1)-0413, and testing with a moving ground and boundary layer suction, that the addition of 1.45% chord and 2.90% chord Gurney flap increased C_L at zero incidence, increasing maximum lift with little effect on the static stall angle. The wake size was found to be larger with the Gurney flap, and increase in extent at a greater rate than the flap-free case. When tested inside of ground effect as an inverted wing, Zerihan and Zhang (2001) found that the Gurney flaps increased the lift, though the smaller flaps increased lift disproportionately more than their larger counterpart. Increasing ground proximity increased lift, similar to increasing incidence in the freestream, although flow separation on the suction surface was promoted with onset at close ground proximities below 20% of chord, causing sharper stalling characteristics.

The lift enhancement induced by the Gurney flap on the rectangular wing is a result of the altered Kutta condition at the trailing edge, with an off-surface stagnation point (Wang et al. 2008). An effective increase in camber is induced by the downward turned flow at the trailing edge, and an effective airfoil extension is a result of the counter-rotating vortices in the near-wake creating the off-surface stagnation point. These vortices delay flow separation from the trailing edge on the leeward surface, thus increasing overall suction and resulting in incremental loading over the wing surface (Jeffrey et al. 2000). These flow phenomena have the effect of increasing bound circulation, and thus an overall increase in the lift coefficient is observed (Wang et al. 2008). The dynamic pressure loss (flow deceleration) on the upstream face increases static pressure on the lower surface, further increasing lift. A theoretical model was developed by Liu and Montefort (2007) which modelled the lift augmentation as a camber-like effect, with agreement found between both numerical and experimental data.

The typical height used for Gurney flaps is $\leq 2\%$ of the root chord, with large increases in drag observed for heights beyond 2%. Niu et al. (2010) predicted, by solving the unsteady two-dimensional Navier-Stokes equations with a force-element theory as applied to a NACA 4412 airfoil equipped with a Gurney flap, an increase of lift at a Gurney flap height of 2% of the wing chord and a non-significant increase in drag. This led to an optimum lift-to-drag ratio at a flap height of 2% of the chord. Giguère et al. (1997) performed a series of tests on an airfoil with flap heights ranging from 0.5-5% of chord. A flow-based scaling was suggested to determine beneficial Gurney flap heights, where an increase in the lift-to-drag ratio was observed at the same angle of attack with increasing strip height. The local boundary layer thickness was used to normalize the flap height, with the evidence from Giguère et al. (1997), as well as from other authors, suggesting that the Gurney flap should be fully immersed in the boundary layer to result in an increased lift-to-drag ratio. The beneficial height for the Gurney flap as compared against boundary-layer thickness is presented in Figure 2.3 (b). Consequently, the pressure distribution on the Gurney flap itself, found by Jeffrey et al. (2000) suggests that the drag increase is primarily due to pressure drag on the surface of the flap. Alternatively, Meyer et al. (2006) introduced wake stabilization in lieu of a splitter plate on a bluff body, by adding slits, holes, and vortex generators into/onto Gurney flaps on FX73-CL3-152 and HQ-17/14.38 airfoils (laminar glide profile, high lift airfoils), experimentally determining force values from a 6-component force balance. These modifications lowered drag through the reduction or elimination of the wake instability and via disturbing the periodic wake flowfield in the two-dimensional case.

Several researchers have extended the implementation of Gurney flaps to delta wings for lift augmentation at low angles of attack and for an investigation of the effect of Gurney flaps on the leading-edge vortices. Greenwell (2010) performed a parametric study on low-speed wind tunnel data, investigating the aerodynamic characteristics of delta wings with sweep angles of 40° to 70° equipped with Gurney flaps. Greenwell (2010) found that the lift increment achieved from the employment of the Gurney flaps was a result of a modification of the attached flow potential lift, rather than the vortex lift. The drag penalty from the Gurney flaps resulted from a bluff body wake correlating to the relative frontal area of the flap, and was found to coincide with the conclusions of Giguère et al. (1997), i.e. that the Gurney flap should be less than the local boundary-layer thickness. However, unlike the cambered 2-D airfoil, the Gurney flap on the 3-D wing had little evidence of an effective camber effect, with symmetrical drag polars and minimal change in the vortex lift component. Similar results are found by Traub and Galls (1999), in which leading- and trailing-edge flaps were added to a 70-degree swept delta wing, with off surface flow visualization and flowfield surveys. Leading-edge flaps, employed from the lower surface, increased the maximum lift coefficient and post-stall lift force, while the trailing-edge Gurney flap results coincided with the conclusions found by Greenwell (2010). The increase in the minimum drag coefficient resulted from the increased wake extent and lower wake stagnation pressure. Li and Wang (2003) applied Gurney flaps to a 40-degree swept non-slender delta wing, determining optimum performance at a flap height of 1% of root chord, and in a similar manner to the application of the Gurney flaps to the rectangular wing/airfoil, a shift in the lift-curve upward and leftward with little change in slope. Serration on the Gurney flap was introduced by Li et al. (2002) on a cropped non-slender delta wing (40-degree sweep), finding an increased aerodynamic efficiency with the serration. This coincides with the assertion that the drag increment is correlated to the projected surface area of the flap, with the larger serrated flap being close in aerodynamic performance with the smaller, non-serrated flap. Surface pressure measurements, along with vapor and oil-film and force measurements by Buchholz and Tso (2000) found a promotion of vortex breakdown with increasing Gurney flap height, which may contribute to the drag increment as well as reducing aerodynamic efficiency from reduced vortex lift at higher angles of attack.

The impact of Gurney flaplike strips on a 65-degree sweep slender reverse delta wing with a 15-degree bevel was investigated by Lee (2016), with the impact on the aerodynamic loading and vortical flowfield determined through force-balance measurements ($Re = 4.06 \times 10^5$) and non-intrusive PIV measurements ($Re = 1.1 \times 10^4$), supplemented with flow visualization techniques and 7-hole pressure probe measurements at $x/c = 1.01$ at $\alpha = 16^\circ$. Three primary configurations were considered, being leading-edge strips in the up or down orientation and side-edge (or trailing-edge) strips. The addition of the leading-edge strips lead to a lower than baseline C_L in the pre-stall α regime, and higher C_L post-stall. In the downward configuration, the leading edge strips delay stalling and increase the maximum lift, similar to leading-edge flaps on conventional wings, while the leading-edge strips in the upward configuration reduced drag from a smaller wake-momentum deficit in the separated wake behind the reverse delta wing. However, these configurations had a lower aerodynamic efficiency relative to the baseline wing. In contrast to this, the impact of the side-edge strips caused a leftward shift of the lift-curve as well as reduction of flow leakage from the pressure surface of the wing. This loss of crossflow leakage led to further pressurization of the windward surface, and an increase in the lift coefficient over the clean wing case, although the maximum lift coefficient and static stall angle were found insensitive to further increases in strip height ($h_{SES} = 1.5\%, 3\%$). The reverse delta wing equipped with side-edge strips however had a higher profile drag and extent of separated flow in the wake. Regardless, the lift increment outweighed the drag increment, and the lift-to-drag ratio of the side-edge strip equipped RDW improved over the clean wing configuration. In terms of vortex flow parameters, Lee (2016a) found that the reverse delta wing vortex moved inboard and closer to the wing surface when the side-edge strips and leading-edge strips in the downward configuration were added. Alternatively, the side-edge strips increased circulation (and thus vortex strength), approximately corresponding to the increased lift generation, further indicating along with Lee and Ko (2016a) that the use of the Kutta-Jowkowski theorem with the reverse delta wing vortex core span may be used for lift correlation, although the outboard nature of the reverse delta wing vortices signals their impertinent role in lift generation.

The use of the side-edge strips on the reverse delta wing prove promising as a means of passive control for lift augmentation. Particularly, due to the advantages of the reverse delta wing planform in ground effect due to the improved longitudinal and height stability, further research on passive control of reverse delta wings in ground effect is warranted.

2.5 OBJECTIVE

As is evidenced by the above review of reverse delta wing literature, there is limited research on reverse delta wings, particularly in ground effect, necessitating the need for further research into the aerodynamic characteristics of reverse delta wings as employed within ground effect. Operating in ground effect improves aerodynamic efficiency, and the Lippisch-type planform has been found to be statically stable in ground effect, albeit with a reduced lift generation or carrying capacity as compared to conventional aircraft. This presents an obstacle to widespread adoption of WIG craft. In particular, the objective of this study is to investigate passive control for lift augmentation via Gurney flaplike strips on a reverse delta wing in ground effect, using force balance measurements on a variety of wing models, varying the anhedral angle, cropping, and slenderness of the wing. This study forms a basis for understanding the aerodynamic loading of a reverse delta wing planform with passive control in ground effect.

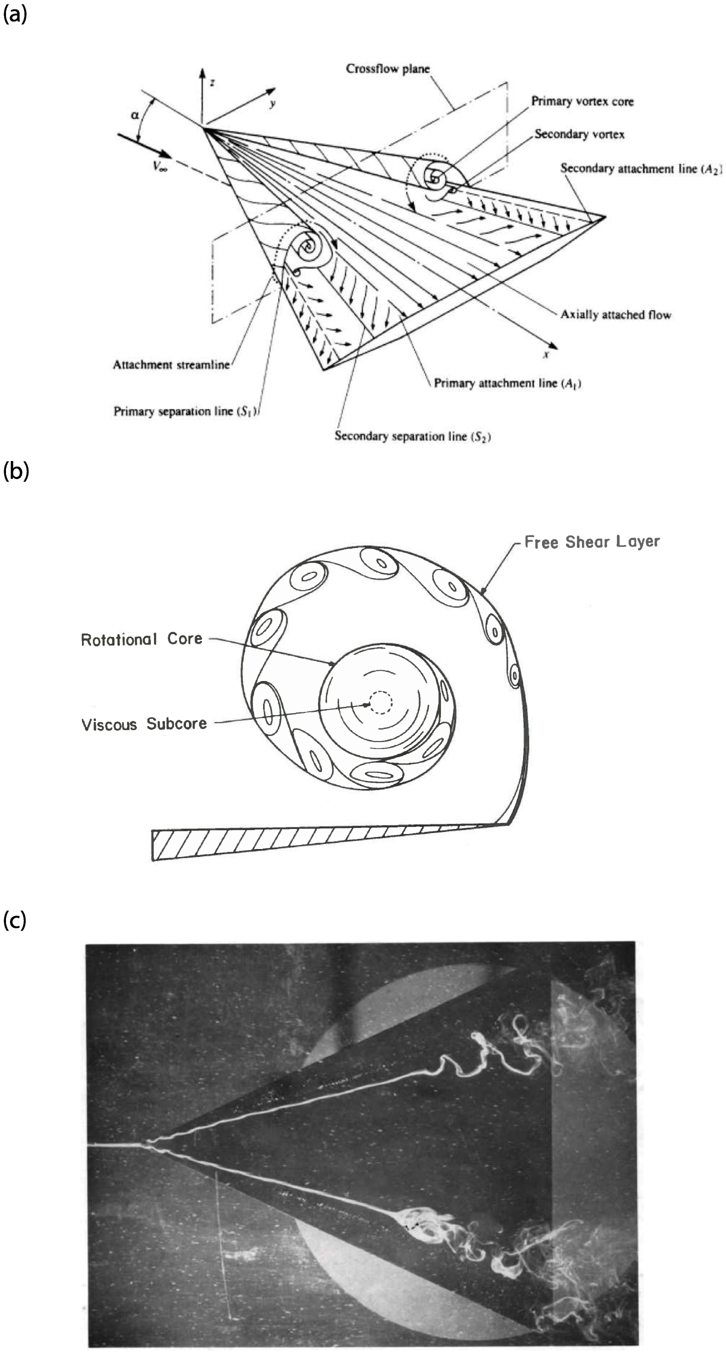

Figure 2.1: View of the leading-edge vortices over a sharp-edged delta wing: (a) schematic view (Rahman et al. 2013), (b) detailed vortex view, indicating three vortex regions (Nelson and Pelletier 2003), (c) breakdown observed via dye-flow visualization, upper is spiral type, lower breakdown is bubble type (Lambourne and Bryer 1961).

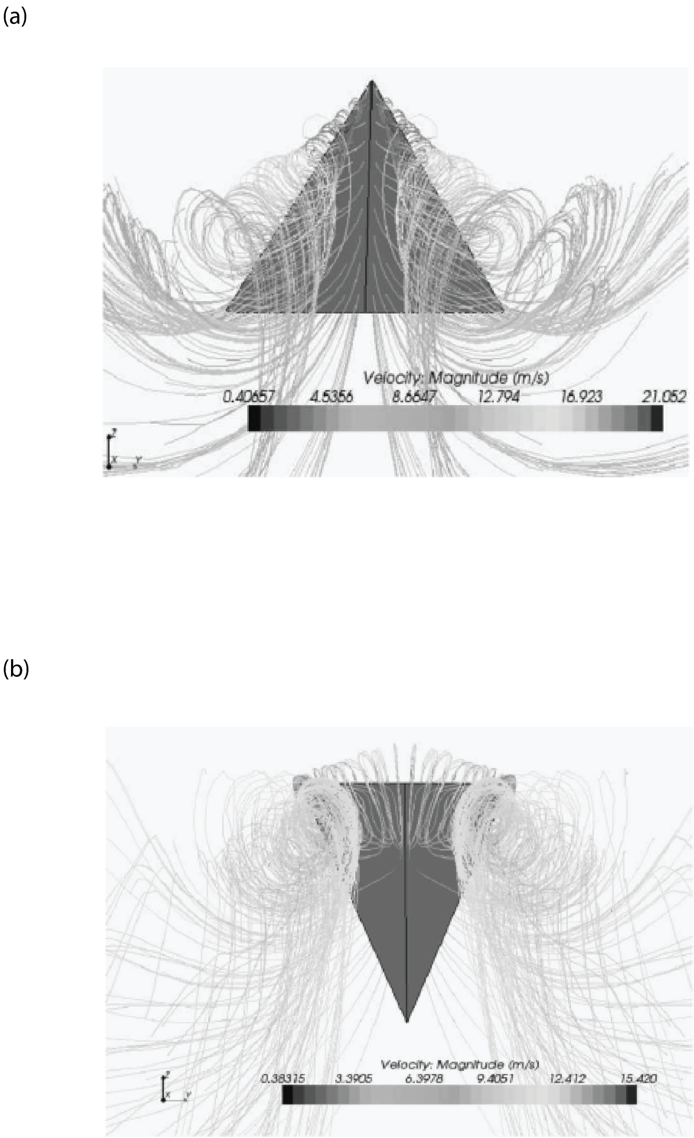

Figure 2.2: Streamlines at $\alpha = 30^\circ$ over a: (a) delta wing, (b) reverse delta wing (Altaf et al. 2011).

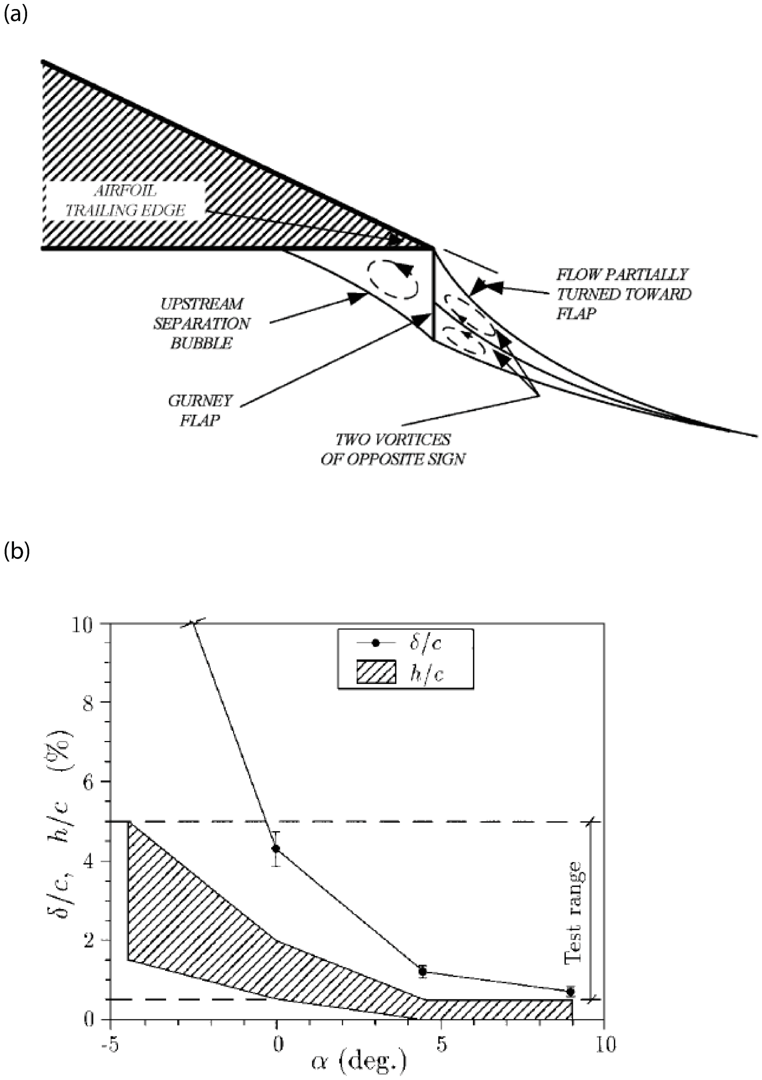

Figure 2.3: Gurney flap on a rectangular wing: (a) schematic diagram (Wang et al. 2008) (b) range of beneficial Gurney flap heights as a function of chord length (h/c), as compared against the boundary layer thickness (Giguère et al. 1997).

CHAPTER 3

EXPERIMENTAL METHODS AND APPARATUS

The methods and techniques used for this study are presented here. First, the flow facilities will be discussed, followed by a description of the experimental apparatus, experimental procedure and test wing models. This chapter concludes with a presentation of the experimental uncertainty.

3.1 FLOW FACILITY

This study was conducted in the *Joseph A. Bombardier* wind tunnel at the Experimental Aerodynamics Lab in the Department of Mechanical Engineering at McGill University. This suction-type tunnel, shown in Figure 3.1 (a)-(b), has a measured turbulence intensity of 0.05% at 35 m/s freestream velocity, and is equipped with a combined honeycomb (10-mm) and three anti-turbulence screens (2-mm ea.) for inlet flow conditioning. Following a 3.3 m, 10:1 contraction ratio inlet contraction, the test section is $0.9m \times 1.2m \times 2.7m$, followed by a 9.1 m 2-stage diffuser into an acoustic silencer for noise attenuation, giving a total tunnel length of 19 m. The tunnel is powered by a 2.5 m diameter fan rated at 125 hp, with 16 blades. A schematic diagram of the wind tunnel is presented in Figure 3.2.

3.2 EXPERIMENTAL APPARATUS

To determine the aerodynamic forces generated by the test wing models, an externally mounted two-component force balance was used in the *Joseph A. Bombardier* wind tunnel. The force balance, attached to the center of the wind tunnel floor, uses two linear variable DCDT-differential transformers (model Sanborn 7DCDT-100 LVDT) to measure applied force. These LVDTs are attached to a rectangular plate centered in a rotating circular disk, to allow for changing angle of incidence. Still images of the rotating connection plate and LVDTs can be seen in Figure 3.1 (c)-(d). The two axes of the force balance are aligned to the normal and axial directions, with the relationship between the normal and axial forces to lift force and drag force as a function of angle of attack, α, as follows:

$$L = N\cos(\alpha) - A\sin(\alpha) \tag{3.1}$$

$$D = N\sin(\alpha) + A\cos(\alpha) \tag{3.2}$$

Each test model is mounted to the force balance using a mounting cylinder and attachment arm, with a mounting bracket welded to bottom of each model. A 0.5-in (1.27 cm) flat Plexiglas sheet, measuring $0.88m \times 1.35m$, with a 25-degree bevelled leading edge was used as the solid boundary for the ground-effect measurements. A pitot-static tube was used to determine flow speeds, connected to a Honeywell DRAL 501-DN differential pressure transducer. This pressure transducer has a maximum head of $50mm$ of H_2O, and was calibrated to the fan speed. A detailed view of the experimental set-up used for the two-component force balance is presented in Figure 3.1 (e)-(f) and Figure 3.3.

The data acquisition system (DAQ) consisted of a 16-channel, 16 bit NI-6259 A/D board, connected to a Dell Dimension E100 PC with a NI BNC-2110 connector box, which converted the analog voltage outputs of the two LVDTs and the pressure transducer to digital inputs for a custom built Labview program on the Dell PC.

3.3 TEST WING MODELS

All wing models were made from thin iron steel plate, with a thickness of $t = 1.5875mm$ $(1/16'')$. The pitching axis was located at $0.5c$ for all test models, where c represents the wing chord. The wings were carefully bent to create the desired anhedral angles ($\delta_A = 8°, 15°, 22°, 30°, 45°$). The wing surface area (S) was not increased for the non-planar models, thus the projected surface area (S) for the anhedraled wings was lowered relative to the original planar wing surface area (S_{org}). The anhedraled models were tested at the angle of attack at which the trailing edge of the model is parallel to the ground, hereafter referred to as its effective angle of attack in ground effect, or α_{eff}. The cropped reverse delta wings were created by removing the rear planform at a percentage of the root chord. The crop percentages tested in this study are 20%, 30%, and 40% of root chord. A schematic of the baseline reverse delta wing and delta wing models is shown in Figure 3.4 and Figure 3.5. The geometric parameters of the baseline delta wing and reverse delta wing for the slender and non-slender cases are given below in Table 3.1. Slender delta wings are considered here for sweepback angles (Λ) greater than 55°. The aspect ratio (AR) is defined as the ratio of the wing span, b, to the wing chord.

All wing models were fabricated at the McGill University, Faculty of Engineering Machine Shop from iron steel sheet metal. The iron steel plate was cut using a shear and bent to the desired anhedral angle with a brake. A steel mounting bracket of $12.7mm \times 12.7mm \times 1.5875mm$ was then welded onto the bottom of each wing, with two drilled holes for bolt insertion, so as to affix the test model to the experimental apparatus (as shown in Figure 3.3). No painting or surface treatment was performed. Measurement uncertainties arising from the fabrication process are listed in Table 3.2.

Λ	Cropping (%)	δ_A	c (mm)	b (mm)	t/c (%)	α_{eff}	S (cm^2)	AR	S/S_{org} (%)
65°	0	0°	356.0	329	0.45	N/A	580.26	1.87	N/A
		8°	356.5	324	0.44	3.66°	548.86	1.91	94.59
		15°	355.0	316	0.45	6.85°	520.69	1.92	89.73
		22°	354.0	304	0.45	9.99°	491.80	1.88	84.76
		30°	356.0	283	0.45	13.27°	416.50	1.92	71.78
		45°	355.5	231	0.45	18.96°	204.81	2.61	35.30
	20	0°	284.0	328	0.56	N/A	546.81	1.97	94.23
	0.3	0°	250.0	328	0.64	N/A	528.56	2.04	91.09
		8°	250.0	326	0.64	3.66°	516.89	2.06	89.08
		15°	248.5	318	0.64	6.85°	502.28	2.01	86.56
		30°	250.5	285	0.63	13.27°	421.32	1.93	72.61
	40	0°	213.0	330	0.75	N/A	496.14	2.19	85.50
50°	0	0°	318.0	527	0.50	N/A	827.33	3.36	N/A
		15°	318.0	507	0.50	12.33°	763.73	3.37	92.31
	30	0°	222.0	527	0.72	N/A	756.40	3.67	91.43
		15°	222.0	510	0.72	12.33°	718.66	3.62	86.86
42.5°	0	0°	292.0	631	0.54	N/A	912.03	4.37	N/A
	30	0°	202.0	632	0.79	N/A	831.34	4.80	91.15

Table 3.1: Geometric parameters of test models.

The test models used are shown in Figure 3.6. A schematic of the reverse delta wing model in and out of ground effect is shown in Figure 3.7, identifying cropping, anhedral angle δ_A, distance between the ground and trailing edge h, and side-edge strip height h_{SES}.

The side-edge strips were made out of thin aluminum strips of thickness of a maximum thickness of 1.56 mm, with constant heights of 2%, 4% and 6% of the root chord. They were attached perpendicularly to the model's lower surface at the side-edges and trailing edges. Two configurations with side-edge strips were tested in the freestream, a closed configuration and an open configuration. Due to the anhedral and cropping on the reverse delta wing, the effective implementation of the side-edge strips on the cropped reverse delta wings required the closure of the open aft planform when side-edge strips were attached to the wing to prevent flow from escaping through the tunnel and opening created anhedral and cropping. This closure was achieved by placing, on the lower wing surface, a thin sheet of aluminum of identical thickness to the side-edge strips perpendicular to the surface, thus effectively closing the opening created by the cropping and anhedral. All testing performed with the side-edge strips on the cropped and anhedraled reverse delta wing was done with the closure of the rear planform on the lower wing surface. The impact of the closure alone (without the additional application of the side-edge strips) is further detailed in Section 4.1.5. A schematic diagram showing the installation of the side-edge strips and rear planform closure is shown in Figure 3.7.

The tests were performed at chord Reynolds numbers of $Re = 3.82 \times 10^5$, $Re = 3.79 \times 10^5$, and $Re = 3.76 \times 10^5$, for the $\Lambda = 65°$, $\Lambda = 50°$, and $\Lambda = 42.5°$ wing models, respectively.

3.4 EXPERIMENTAL PROCEDURE

The force balance was calibrated in situ using a calibration weight set, with weights ranging from $0-2kg$, resulting in a maximum force of approximately $19.62N$ measured by each LVDT. To calibrate the force balance, incremental weight was added in tension to the mounting cylinder (shown in Figure 3.3), resulting in an approximately linear relationship (within 1%) between the voltage output of the LVDT and applied mass (or force). The tension force was applied in-line, or parallel, to each LVDT, resulting in two linear calibration curves for the two LVDTs. These curves thus correspond to the relationship between the normal and axial forces in Equations 3.1-3.2, and the voltage output from each LVDT measured by the DAQ.

The drag generated by the model support system (mounting cylinder and attachment arm) was corrected for by measuring the drag force of the support system without the test model attached, and subtracting the resulting force from all measurements. The velocity measured by the pitot-static tube was found to correlate strongly with the model angle of attack and ground clearance, corresponding to a modification of the blockage of the wind tunnel test section. Thus, to account for blockage, the local velocity (at time of force measurement) as measured by the pitot-static tube described prior (shown in Figure 3.3) was used in lieu of the freestream velocity of the tunnel for lift and drag coefficients (normalization of the LVDT force measurements). No other blockage or experimental apparatus drag corrections were applied.

Once the test model was securely attached to the experimental apparatus and the wind tunnel operating at the desired velocity, measurements of the normal and axial forces and instantaneous velocity were performed. 3° measurement intervals were used for the angle of attack, except around stalling where measurements were taken at 1° intervals to capture the static stall angle of attack. When in ground effect, at each angle of attack, ground proximity was set at each angle using the appropriate gauge block for each wing model, with the flat Plexiglass sheet being hand moved to the required location. Guide rails (shown in Figure 3.3) kept the ground parallel to freestream. For each ground proximity, which ranged from $0 - 60\% h/c$, ground proximity was held constant while angle of attack was varied in the same manner as out of ground effect measurements. After every change in angle of attack (and ground proximity when in ground effect), the flow was allowed to stabilize and reach its time-averaged steady-state condition, with approximately 2-3 seconds before the voltage output from the pitot-static tube and LVDTs were acquired by the DAQ. The voltages were sampled at 1000 samples per second, for 40 seconds, resulting in 40,000 samples total for each measurement, which were then averaged over the sampling duration. Finally, each voltage was then converted using its respective calibration curve to the normal and axial forces for the LVDTs, and the local or instantaneous velocity for the pitot-static tube. The normal and axial forces were changed into lift and drag forces via Equations 3.1-3.2, the drag correction was applied as per the prior description, and the resulting forces normalized into lift and drag coefficients with the local velocity used to account for blockage as per the described blockage correction procedure. All results presented in this work are in the form of lift and drag coefficients.

3.5 UNCERTAINTY ANALYSIS

The uncertainty for each experimental variable is listed in Table 3.2. The maximum uncertainty in the lift and drag coefficients are ± 0.025 and ± 0.012 for C_L and C_D, respectively. These values were determined following the procedure as outlined in Moffat (1998). Additional sources for experimental error may be from bending deflection of the wing support arm, which was not accounted for in this experiment. Additionally, the experimental set-up required a slot in the ground beneath the wing, to allow for the cantilevered support arm and ground to move freely. The impact of the slot was minimized by applying a covering over the slot between each measurement.

Parameter	Uncertainty	Operating Range
Model thickness, t	± 0.01 mm	1.59 mm
Model chord, c	± 0.5 mm	292.1-355.6 mm
Model span, b	± 0.5 mm	328.6-633.0 mm
Model angle of attack, α	± 0.5°	0°-50°
Model sweep angle, Λ	± 0.5°	42.5°, 50°, 65°
Model anhedral/dihedral angle, δ_A	± 0.5°	0°-45°
DAQ Board	± 0.15 mV	0-10 V
J. A. Bombardier wind tunnel velocity	± 0.2 m/s	12-15 m/s

Table 3.2: Details of the contributions to the measured uncertainty from the experimental set-up parameters.

Figure 3.1: The *Joseph Armand Bombardier* wind tunnel. (a) Outlet with fan and acoustic silencer, (b) inlet of the wind tunnel with visible honeycomb flow straightener, (c) linear variable differential transformers, (d) rotating attachment plate for variable α, (e) experimental set-up inside test section, (f) close up of experimental set-up.

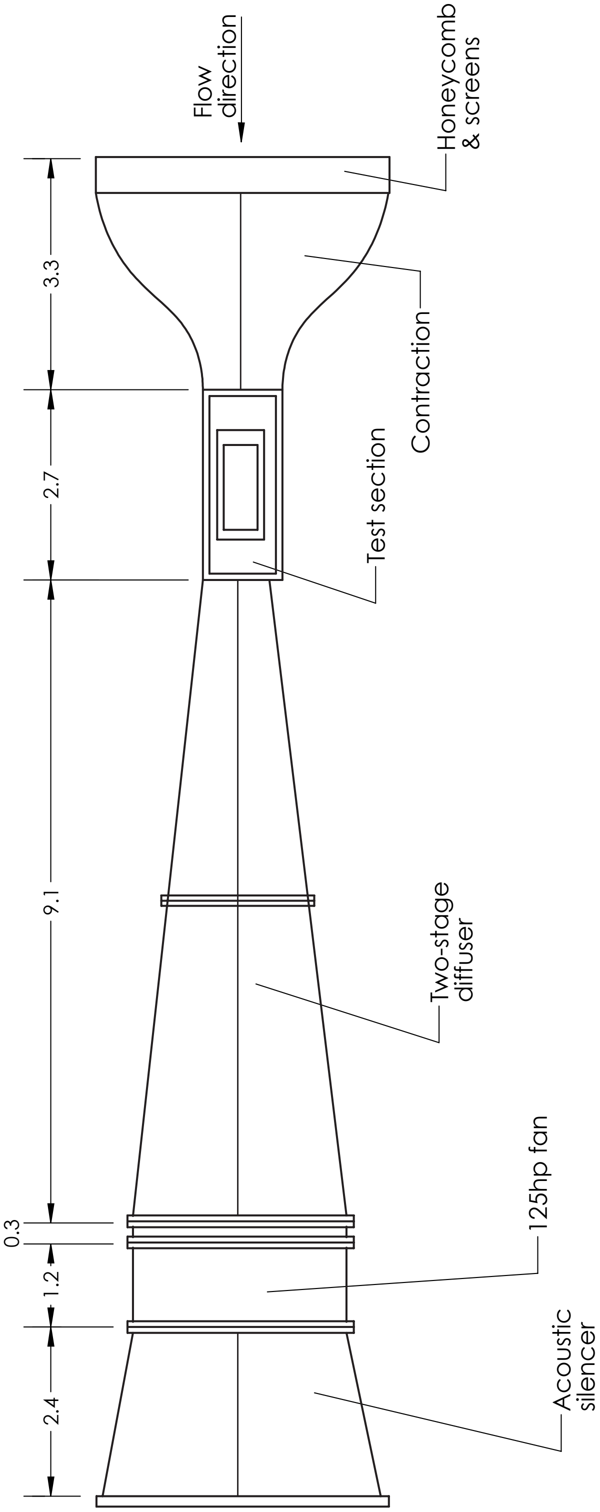

Figure 3.2: Schematic diagram of the *Joseph A. Bombardier* wind tunnel.

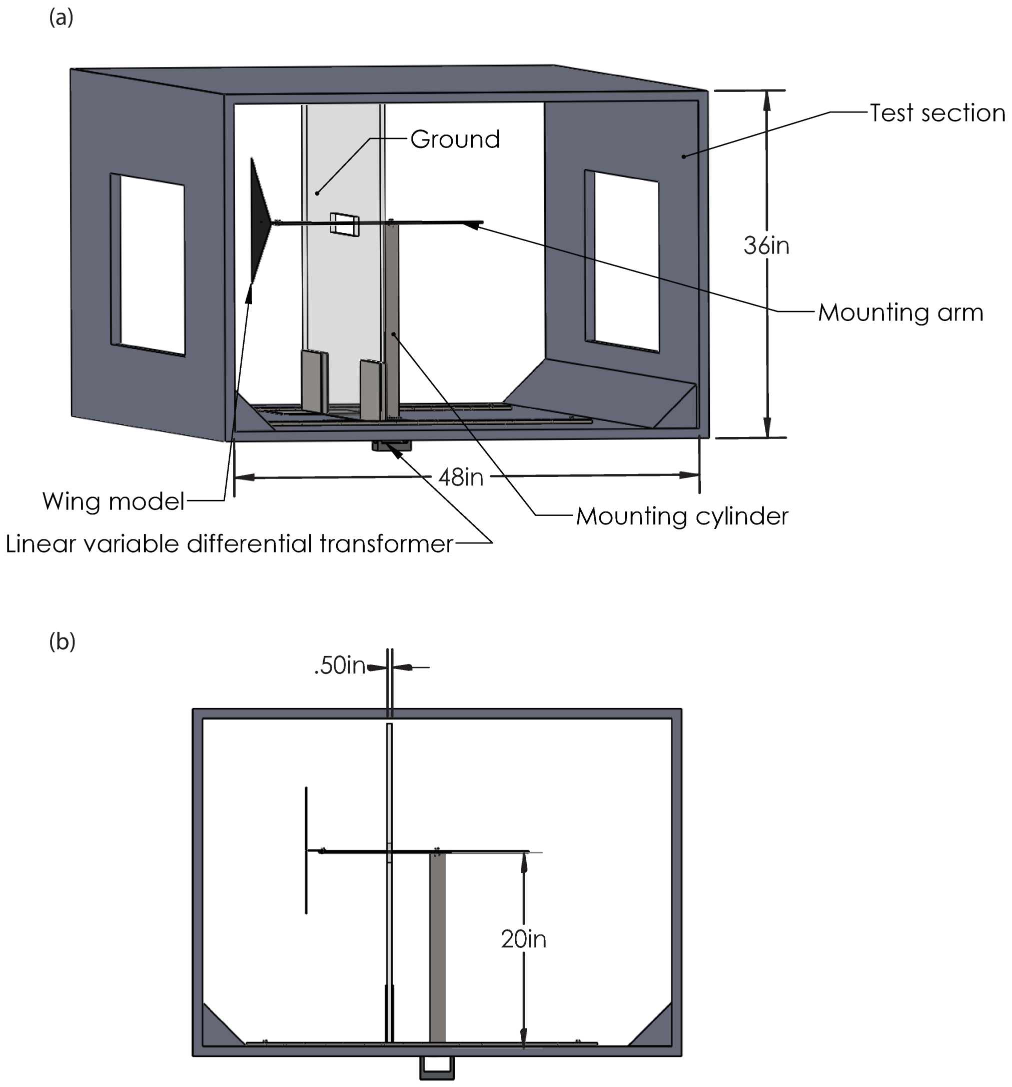

Figure 3.3: The wind tunnel test section, with force balance measurement experimental setup with: (a) isometric view, (b) front view.

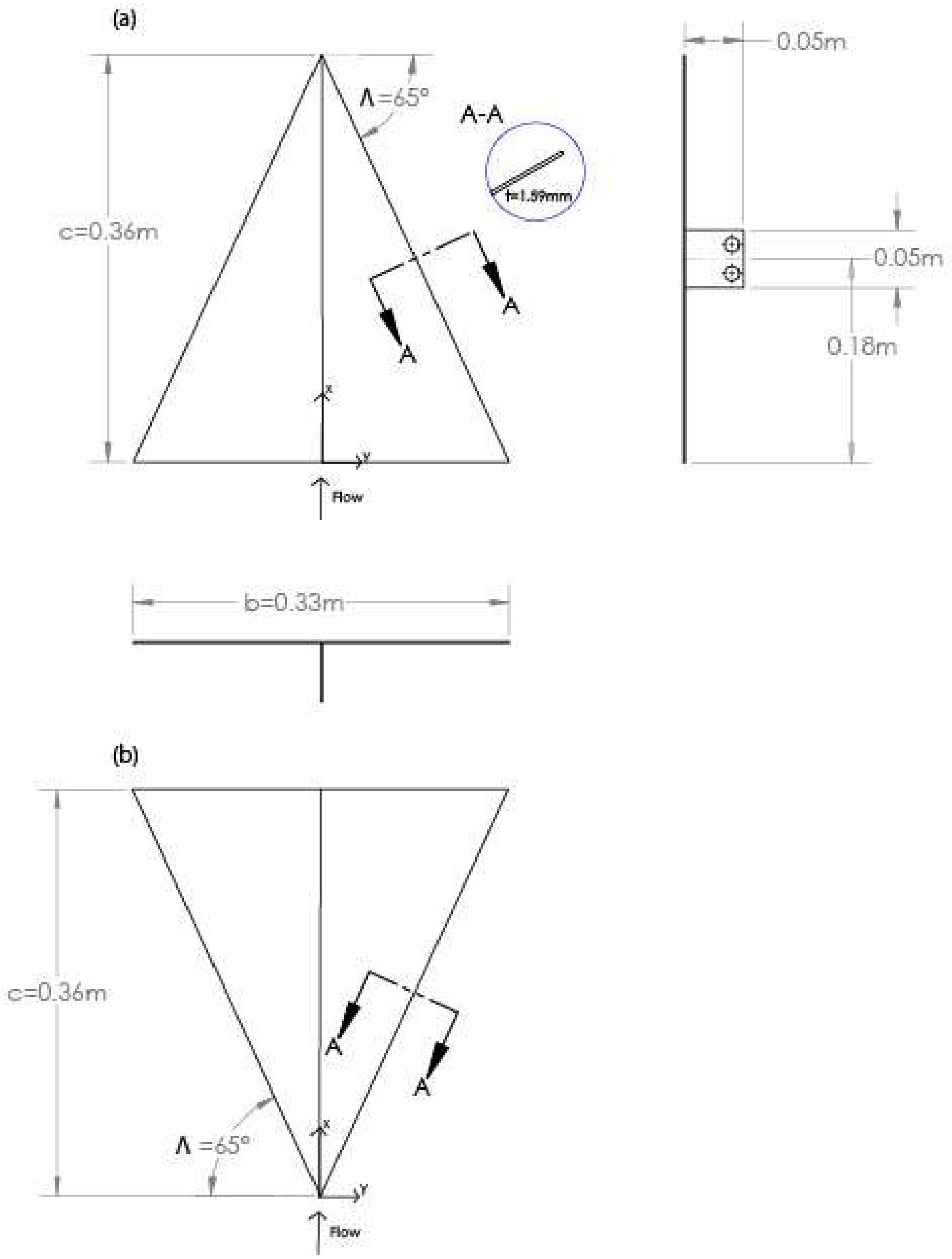

Figure 3.4: Schematic diagram illustrating the baseline slender, with no anhedral, cropping, or passive control: (a) reverse delta wing and (b) delta wing.

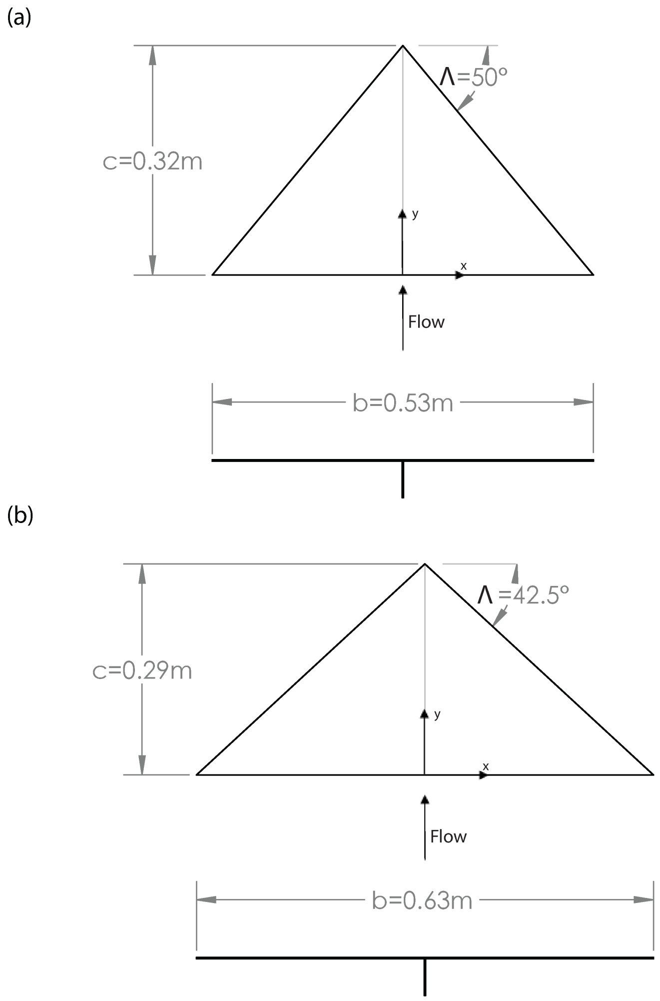

Figure 3.5: Schematic diagram illustrating the baseline non-slender reverse delta wings, with no anhedral, cropping, or passive control: (a) $\Lambda = 50°$ and (b) $\Lambda = 42.5°$.

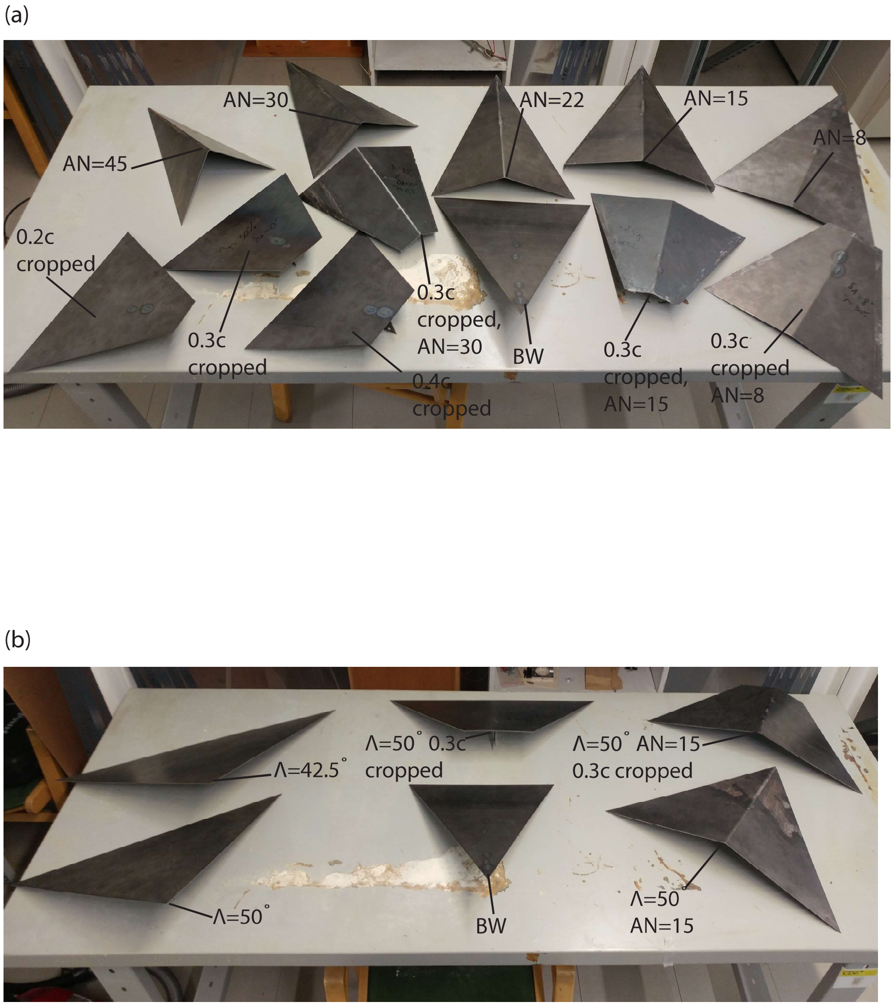

Figure 3.6: Images of the test models used. BW denotes the 65-degree sweep, non-cropped, non-anhedraled wing as the baseline wing. (a) Slender, (b) non-slender, slender BW included for visual comparison.

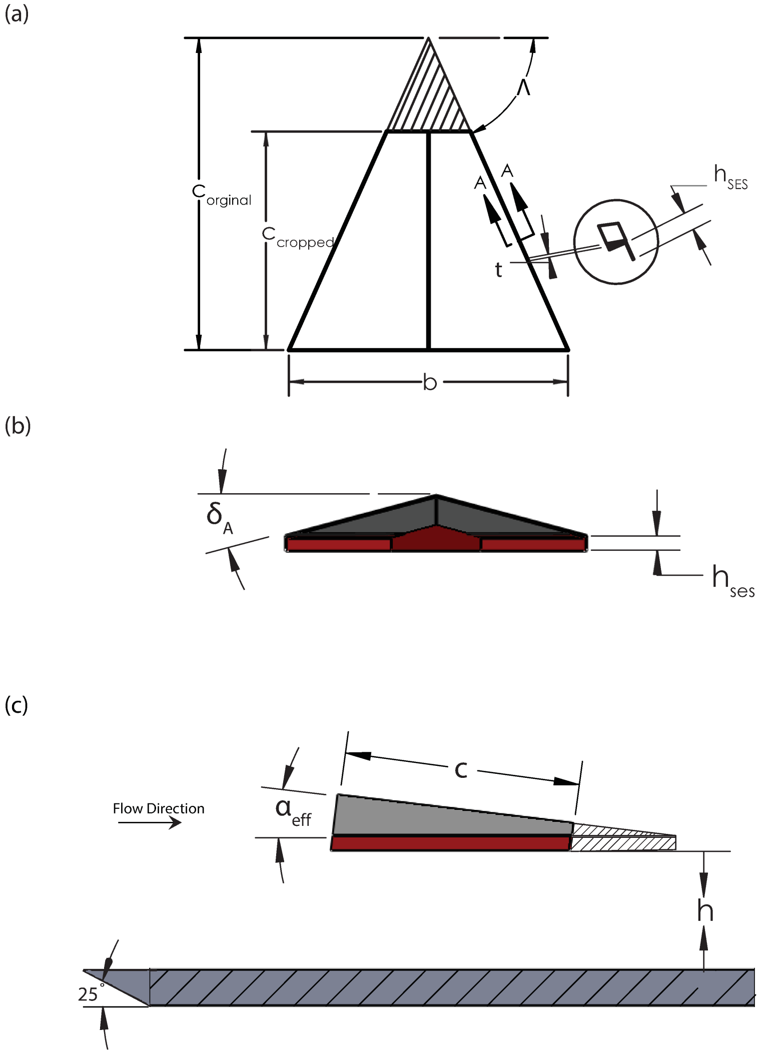

Figure 3.7: Schematic diagram of the reverse delta wing with anhedral, cropping, and side-edge strips. Shading was added to the front and side views for clarity. (a) Top view, (b) front view with rear planform closed off, (c) side view in ground effect.

CHAPTER 4

RESULTS

In this chapter, the results of the force balance measurements of the aerodynamic loading of the delta wing and reverse delta wing are discussed. Firstly, the results outside of ground effect are analyzed, for slender and non-slender cases. The inside of ground effect results are then discussed, broken into two further subsections, covering the baseline case inside ground effect, non-slender cases, cropped and anhedral cases, and concluding with the analysis of the passive control cases inside ground effect.

4.1 OUTSIDE OF GROUND EFFECT

This section will discuss all outside of ground effect measurements, with an emphasis on the effect of cropping, anhedral, and the addition of the side-edge strips so as to serve as a clear comparison for the altered aerodynamics inside of ground effect.

4.1.1 Baseline Slender Delta and Reverse Delta Wings

The results obtained from force balance measurements for the baseline delta wing and reverse delta wing with a sweep angle of $\Lambda = 65°$ are presented in Figure 4.1, denoted as DW65 and RDW65, respectively. Also included in Figure 4.1 are the results for the non-slender cases, for $\Lambda = 50°$ and $\Lambda = 42.5°$, denoted as DW50, RDW50 and RDW42, which will be discussed in Section 4.1.2. The delta wing configuration of the $\Lambda = 42.5°$ model was not tested in this work due to time limitations with the flow facility, and due to the RDW42 model being tested to validate drawn conclusions on non-slender reverse delta wing performance in ground effect. For validation of experimental results, plotted on Figure 4.1 are the results of Altaf et al. (2011) for a 75-degree sweep delta wing and reverse delta wing at a chord Reynolds number of $Re = 3.82 \times 10^5$. The present experimental results for DW65 and RDW65 agree reasonably well with this data when considering the differences in the sweep angle.

Figure 4.1 (a) shows that for $\alpha < 14°$, the lift coefficients for the baseline slender reverse delta wing and regular delta wing are approximately equal, i.e., the $C_L - \alpha$ curve slopes and C_{L0} values are approximately of equal value. This is as expected given that for slender delta wings and reverse delta wings at these low angles of attack, the lift production is dominated by attached potential flow, and the leading-edge vortices (LEVs) on the delta wing are absent or contribute little to the delta wing lift. For $\alpha \geq 14°$, the LEVs of the delta wing grow in strength and the non-linear vortex lift component contributes more to the total lift, increasing the lift generation of the delta wing over that of the reverse delta wing. The RDW65 has a delayed stall relative to DW65, with a static stall angle, α_{SS}, of 38° compared to that of 34° for the delta wing, although due to the increased non-linear vortex lift of the delta wing, the maximum lift coefficient, C_{Lmax}, for the delta wing exceeded that of the reverse delta wing, being 1.26 and 1.17, respectively. The stalling of the delta wing is primarily induced by the breakdown of the leading-edge vortices progressing upstream over the wing with increasing angle of incidence, while the stalling of the reverse delta wing is induced by the breakdown of the multiple spanwise vortex filaments (SVFs) over top of the wing (see Lee and Ko 2016a). The delayed stalling of the reverse delta wing relative to the delta wing and the outboard location of the vortices suggest that the reverse delta wing vortices do not contribute to the lift generation of the reverse delta wing, and while their size and strength may be related, they are not directly responsible. The disruption of the RDW vortices and SVFs beginning by $\alpha = 18° - 20°$ (see Figure 3 of Lee and Ko (2016a)) over the wing while stalling is delayed to a much greater incidence, further indicates that the primary lift generation for the reverse delta wing comes from the static pressure rise on the lower surface, while the upper wing surface is a primary source of drag through wake generation. The geometry of the reverse delta wing may be responsible, as the trailing edges recede inboard faster than the vortices generated at the apices of the wing travel downstream and inboard. These vortices are thus unable to directly interact with the wing due to their outboard location. Instead, the primary lift generation is from the windward wing surface for the RDW (Lee and Ko 2016a). The surface area of the reverse delta wing recedes faster than the chord progression, so that at 20% chord, there is 33.38% surface area, while at 50% chord there is 70.91% surface area. As compared directly to the delta wing, there is a greater surface area on the wing that is exposed to broad regions of constant pressure on the lower surface, with larger gradients confined to the trailing edge, as can be observed in Figure 9 in Altaf et al. (2011). These pressure gradients being confined to the trailing edge region allows the development of the multiple SVFs on the upper surface. As well, these confined gradients suggest that moderate rear planform cropping may have only a small aerodynamic penalty, and is investigated further in Section 4.1.3 below. Presented in Figure 4.1 (c), the drag coefficient of the reverse delta wing follows closely to that of the delta wing until the LEVs develop on the upper surface of the delta wing, contributing to profile and pressure drag. Thus, at higher angles of attack, the drag production from the delta wing exceeded that of the delta wing at the same angle of attack. Figure 4.1 (d) reveals that in the high-lift regime, for the same value of lift of the reverse delta wing and delta wing, the drag of the delta wing is lower than that of the reverse delta wing, due to the LEVs significantly increasing lift generation. Notably, the lift-to-drag ratio of the reverse delta wing is comparable to that of the delta wing, despite the reduced lift.

4.1.2 Baseline Non-Slender Wings

The non-slender delta and reverse delta wings, with $\Lambda < 65°$, have significantly different aerodynamic characteristics than their slender counterparts, as evidenced by the force balance measurement results presented in Figure 4.1. The cropped results and anhedraled results in the freestream will be later discussed in Section 4.1.3-4.1.4 alongside their slender counterparts. The variation of lift coefficient with angle of attack presented in Figure 4.1 (a) demonstrates an increase in the $C_L - \alpha$ curve slope with decreasing sweep angle, i.e., a non-slender delta wing and reverse delta wing have steeper lift-curve slopes. The 50-degree non-slender delta wing, DW50, had a sharper stall as compared to the more gradual stalling characteristics of the slender RDW65 and DW65. DW50 had a C_{Lmax} of 0.9886 at $\alpha_{SS} = 21°$. The leading-edge vortices form closer to the wing surface with reducing sweep angle, resulting in a promoted stall of the non-slender delta wing due to the interaction with the boundary-layer flow (Gursul et al. 2005). While the leading-edge vortex may have increased circulation and strength with a reduction in sweep, its trajectory with increasing angle of attack brings it closer to the wall shear layer, which may cause further instabilities resulting in a sudden vortex breakdown. Interestingly, unlike the slender RDW65 and DW65, DW50 and RDW50 have non-equal lift slopes and lift coefficients below $\alpha = 9°$, with the RDW50 having increased lift compared to its regular delta wing counterpart. A reduction in sweep with RDW42 led to a further increase in lift for $\alpha \leq 9°$. For $9° < \alpha < 24°$ and $9° < \alpha < 30°$ for RDW50 and RDW42, respectively, the lift coefficient gradually increases to C_{Lmax}, while beyond 24°(RDW50) or 30°(RDW42) the lift coefficients gradually decrease. This very gradual stalling provides a maximum lift coefficient of $C_{Lmax} = 0.7657$ (RDW50) and $C_{Lmax} = 0.7540$ (RDW42). The increased lift of the non-slender reverse delta wing, over both its slender and regular delta wing counterparts at low angles of attack, may be in part a result of the increased wing surface area at the fore part of the wing, and increased surface area overall (see Table 3.1).

Notably, unlike the slender models, and the non-slender delta wing, the drag for the non-slender reverse delta wings increased monotonically, even while lift plateaued (see Figure 4.1 (c)). Due to this monotonic increase, the drag for RDW50 and RDW42 is higher than the slender RDW65 for $\alpha < 18°$, and lower for $\alpha > 18$. This corresponds approximately to the incidence angle at which the lift coefficient of RDW65 exceeds that the non-slender RDWs ($\sim \alpha = 18°$). Due to the increased lift generation below, and decreased drag production above, $\alpha = 18°$, the lift-to-drag ratios of the non-slender reverse delta wings, RDW42 and

RDW50 are lower than that of RDW65. Notably, the planar reverse delta wings tested in this study have $C_L/C_{D_{max}}$ at an incidence angle of $\sim \alpha = 6°$, with the maximum lift-to-drag ratio of RDW42 larger than that of RDW50, due to the increased lift generation below $\alpha = 9°$. The maximum lift-to-drag ratio was 2.58 and 2.74 for the RDW50 and RDW42, respectively. Surprisingly, as seen in Figure 4.1 (d), for a given drag coefficient in the low-α regime, the lift coefficients are approximately equal, and the relationship is nearly linear in contrast to the slender RDW. For a given lift condition in this regime, the drag coefficients are approximately equal for slender and non-slender baseline wings.

4.1.3 Effect of Rear Planform Cropping

Planform cropping is advantageous in that it reduces the weight of the wing, and may do so with minimal aerodynamic performance penalties. The impact of planform cropping on a slender reverse delta wing is presented in Figure 4.2 (a)-(g), for 20%, 30%, and 40% reductions in chord, or 5.76%, 8.91%, and 15.50% reductions in wing surface area, with the coefficients normalized by the original non-cropped surface area (S_{org}). Figure 4.2 (a) reveals that the lift-curve slope is approximately equal below $\alpha = 12°$ for all three cropped wings as compared against the baseline reverse delta wing (full planform, no anhedral). At $\alpha = 12°$ for the 40% cropped RDW, significantly reduced lift generation after $\alpha = 15°$ and stall promotion ($\alpha_{SS} = 27°$) suggests the flow separation is significantly enhanced. The other two cropped models (20% and 30%) continue to closely match the baseline RDW before prematurely stalling, with stall angles of 36° and 34° for the 20% and 30% cropped wings, respectively. C_{Lmax} is reduced for all three cropped wings, decreasing by 9%, 11%, and 36%, for the 20%, 30%, and 40% cropped wings, respectively. The stall promotion and reduced maximum lift indicates that the planform cropping leads to enhanced backflow from the trailing edge region enhancing disruption of the SVFs, with disruption occurring at lower angles of attack than the baseline case. Figure 4.2 (e) compares the lift coefficient of the cropped and non-cropped wings (i.e., $\Delta C_L = \frac{C_{LCW} - C_{LBW}}{C_{LBW}}$), where CW denotes the cropped wing and BW the baseline wing. The 20% and 30% cropped RDWs have little deviation in their lift generation until the onset of their respective stalling regimes, while the 40% cropped wing has significantly reduced lift beyond $\alpha = 15°$. Moderate removal, i.e. less than 0.3c of the aft portion of the reverse delta wing, did not significantly reduce the lift below $\sim \alpha = 30°$. This indicates that the majority of the lift generation occurs not only on the lower surface of the wing, but prior to approximately $x/c = 0.7$, or 70% of the root chord of the baseline wing.

The reduced chord of the cropped RDW and straight trailing edge is thus hypothesized to promote back flow and the influence of the trailing edge region on the upper wing surface. This suggested increase in disrupted flow around the trailing and side edges for the cropped reverse delta wing has an impact on the drag characteristics and the overall aerodynamic performance. Similar to the lift coefficient, the drag coefficient trend for the cropped wings follow closely to the baseline case, however with increased drag due to the likely increased disrupted flow at the trailing edge (Figure 4.2 (c)). An increased disrupted flow would result in a larger adverse pressure gradient and thus separated flow over the cropped upper surface, with a greater wake size and extent. This is a possible cause for the overall increase in drag for $\alpha = 15°$. As cropping reduced both chord length and surface area, with increasing crop percentage, the lift and drag coefficients decreased, normalized by the baseline wing area (before planform cropping). While the largest reductions in C_L and C_D were seen for the 40% cropping, the 20% and 30% cropping had small lift and drag penalties. For all three cropped wings, the overall lift-to-drag ratio and $C_L/C_{D_{max}}$ was reduced, with significant losses in efficiency below $\alpha = 10°$. The lowest maximum reduction in aerodynamic efficiency was achieved by the 30% cropped reverse delta wing. With a reduction of chord length by 30%, the C_L/C_D was reduced by a maximum of 34%, and above $\alpha = 10°$ the 30% cropped RDW C_L/C_D was consistently less than 10% lower than the baseline RDW. From these results, 30% cropping was selected for further study in ground effect.

The impact of non-slenderness on the cropped reverse delta wing is presented in Figure 4.1 (a)-(d). From the above findings, only 30% cropping is considered, with $\Lambda = 50°$ & $\Lambda = 42.5°$. For both non-slender wings, the lift coefficient is approximately equal to the non-slender baseline below $\alpha = 12°$ and $\alpha = 9°$ for RDW50 and RDW42, respectively. However, significant reduction in C_L is seen above these angles of incidence, likely due to the reduction in surface area. Notably, C_{Lmax} remains at the same angle of attack as the non-cropped wing, indicating that the lift generation reduction is due to lower planform area, with little change in overall aerodynamic characteristics. Similarly, likely due to decreased surface area, C_D decreased relative to the baseline RDW50 and RDW42, leading to similar lift-to-drag ratios, unlike the slender case. These results indicate that the introduction of cropping has minor impact on the already likely fully separated flow over the non-slender reverse delta wing at even moderate angles of attack for the non-slender case. In short, planform cropping, below 30% of root chord, is beneficial to reverse delta wings in that it can reduce the weight of the wing with minimal aerodynamic penalty in typical flight regimes, for both slender and non-slender cases.

4.1.4 Effect of Anhedral

The impact of varying the anhedral angle on the RDW65 is presented in Figure 4.3. The lift and drag coefficients were normalized by the baseline reverse delta wing surface area before the introduction of anhedral, as indicated in Table 3.1. Figure 4.3 (a) reveals that for a given α, with increasing δ_A, C_L was found to decrease relative to the baseline RDW65, likely in part due to the reduction in projected wing area, decreasing the slope of the $C_L - \alpha$ curve. C_D was found to decrease below the baseline RDW65 for $\delta_A \geq 22°$, yet notably was close to the baseline wing for $\delta_A \leq 15°$. The drag reduction may be due to three factors: (i) the anhedral geometry produces components of force in the spanwise direction on the lower surface, partially reducing pressure drag, (ii) a wake reduction from a change in the separated flow behavior over the upper wing, (iii) lower projected surface area from anhedral. For the same C_L, C_D increases with increasing δ_A (see Figure 4.3 (d)), as the anhedraled model operates at a higher angle of attack for the same lift condition. While for increasing δ_A, C_{Lmax} decreased, the static stall angle was not affected. With the significant reductions in lift, the lift-to-drag ratios of the anhedraled wings decreased relative to the baseline wing, with $C_L/C_{D_{max}}$ decreasing significantly with increasing δ_A.

Included in Figure 4.3 (a)-(d) are the cropped wing models with anhedral (hollow symbols representing cropped configurations), with $\delta_A = 22°$ and $\delta_A = 45°$ not tested in the cropped configuration. C_L and C_D are normalized by the original planform surface area, before anhedral and cropping (see Table 3.1). Only 30% rear planform cropping was investigated, as per the results of Section 4.1.3. The lift and drag forces follow closely to the trend observed for the non-cropped wings, with the stalling angle and maximum lift deceased by the cropping. With increasing δ_A, a decrease in C_L was observed, and for $\delta_A \geq 30°$ ($\delta_A = 22°$ was not tested) a reduction in drag was observed, similar to that of the non-cropped planform.

The force balance measurement results for the non-slender reverse delta wing with anhedral, and with cropping is presented in Figure 4.1 (a)-(d), presenting the impact of reducing the sweep angle to $\Lambda = 50°$ from the slender configuration. The anhedral angle tested for the non-slender configuration was $\delta_A = 15°$. Figure 4.1 (a) reveals that, similar to the slender RDW, the introduction of anhedral yields a reduced $C_L - \alpha$ slope relative to the non-anhedraled wing, both with and without cropping. However, the non-slender anhedraled reverse delta wings have a softer transition from this linear potential lift to the plateaued lift coefficient for $\alpha > 12°$. As a result, the non-slender reverse delta wing C_L became insensitive to the anhedral for $\alpha = 15°$(non-cropped) or $18°$(30% cropped). An invariant

α_{SS} and C_{Lmax} between the anhedraled and non-anhedraled non-slender reverse delta wings suggests the presence of fully separated flow over the upper surface non-slender reverse delta wing in this lift regime which is relatively insensitive to the introduction of the 15° anhedral in a manner similar to the introduction of rear planform cropping. However, C_D is reduced with the introduction of the anhedral, similar to the slender case, with the lift-to-drag ratios collapsing in the moderate to high-α regime, although the anhedraled C_L/C_D is slightly improved over the non-slender baseline wing in this regime. Consequently, for a given C_L, the C_D of the non-slender anhedraled wing is approximately that of the non-anhedraled counterpart (see Figure 4.1 (d)).

With the significant lift reduction observed for the $\delta_A = 45°$ anhedraled wing, this wing was not studied with passive control inside or outside of ground effect.

4.1.5 Addition of Side-Edge Strips

With the analysis of the out of ground effect results for anhedral and cropped reverse delta wings presented in Section 4.1.3 and Section 4.1.4, this section will deal with establishing the impact of side-edge strips on reverse delta wings in the freestream. The addition of side-edge strips to the $\delta_A = 15°$ reverse delta wing is presented in Figure 4.4. The change in the lift coefficient resembles that of the deployment of conventional trailing edge flaps. The lift slope has been shifted leftward and upward, so as to produce a higher lift at each angle of attack with increasing strip height. Additionally, this means there is a non-zero lift at $\alpha = 0°$. This behaviour also somewhat resembles that of trailing edge Gurney flaps on wings and airfoils. The addition of the side-edge edge strips to the reverse delta wing induces a camber-like effect, as well as alleviating cross-flow leakage from the high pressure lower surface to the low pressure upper surface, thus increasing the static pressure on the lower surface of the wing and entrapping high pressure fluid beneath the reverse delta wing (Lee 2016). Since the main lift generating mechanism for the reverse delta wing is the static pressure rise on the lower surface, with the equipment of the Gurney-like flaps there is an increase in stagnated flow beneath the wing coupled with a corresponding static pressure rise and increase in C_L (Ko 2017).

The lift coefficient with varying strip height on the $\delta_A = 15°$ model (non-cropped) is presented in Figure 4.4 (a). Despite the increased C_L with increasing h_{SES}, C_{Lmax} was marginally improved with the addition of the side edge strips, increasing by 5%, 2%, and 1%, for 2%, 4%, and 6% h_{SES} over the $\delta_A = 15°$ clean wing, respectively, where the clean wing refers same model without side-edge strips (or $h_{SES} = 0\%$. Stalling was promoted with the wing stalling at 36°, 35°, and 34° for the addition of 2%, 4%, and 6% strips, respectively, versus

38° without SES. This is likely due to promoted flow separation with increasing strip height, contributing to a larger wake or low pressure zone downstream of the flap, thus increasing the adverse pressure gradient acting upon the upper surface. Due to this likely increased separated flow, the lift coefficients for the SES cases approximately collapsed for $\alpha \geq 24°$, thus resulting in the minimal change in C_{Lmax} and a lowered α_{SS} as aforedescribed. The greatest lift augmentation by the SES is achieved at lower angles of attack, particularly below $\alpha = 12°$. At higher angles, closer to stalling, the addition of the SES provides minimal increases to the lift coefficient.

For typical application of Gurney flaps, the height of the flap is less than the local boundary layer thickness, so as to not extend past the boundary layer and increase drag from exposure to freestream flow. Figure 4.4 (c) shows that with increasing h_{SES}, the SESs cause an increase in C_D, likely from the constrained high pressure fluid flow beneath the wing and an increasingly adverse pressure gradient enhancing the disruption of the spanwise vortex filaments and increasing the extent of separated flow. As a result of the increased drag observed, the lift-to-drag ratio of the RDW with the SES is below that of the clean wing case for $h_{SES} > 2\%$ and $\alpha \geq 6°$ (Figure 4.4 (b)). An increased C_L/C_D is observed in the low-α regime due to the significantly increased lift over the clean wing configuration at low angles of attack.

As described prior, cropping of the rear planform of the RDW reduces C_{Lmax}, and promotes stalling (i.e. α_{SS} is reduced). The results of the addition of side-edge strips to the $\delta_A = 15°$, 30% cropped, reverse delta wing are presented in Figure 4.5. Similar to that of the non-cropped case, with passive control added to the anhedraled RDW, the lift coefficient slope remains linear for $\alpha < 12°$. Notably, C_L remains close to the non-cropped wing for most angles of attack, up to approximately 30°. The lift-curve shifts left, and follows closely to that of both the non-cropped and baseline anhedraled wing without SES, until approximately $\alpha = 12° - 15°$. C_{Lmax} however remained similar (though slightly lower) than the non-cropped wing, and stalling is promoted from the cropping. Stalling occurred at 36° for the 2% wing, $34 - 35°$ for the 4% wing, and 32° for the 6% cropped wing. For contrast, the anhedraled wing ($\delta_A = 15°$) without cropping stalled at $\alpha_{SS} = 38°$ while the 30% cropped RDW with the same δ_A stalled at $\alpha_{SS} = 36°$. At higher angles of attack, the benefit of increasing the SES height diminishes, and the lift coefficient becomes increasingly insensitive to increasing h_{SES}, similar to that of the non-cropped wing. Both the cropped and non-cropped cases had similar drag coefficients in the freestream, except for $h_{SES} = 2\%$, which for the 30% cropped $\delta_A = 15°$ model followed closely to the 4% strip (see Figure 4.4 (c) and Figure 4.5 (c)). Drag increased in the same manner as the non-cropped model, with C_D increasing with increasing incidence and h_{SES}. The incremental lift and drag coefficients over the 30% cropped baseline wing ($\Delta C_L = (C_L - C_{LBW})/C_{LBW}$, $\Delta C_D = (C_D - C_{DBW})/C_{DBW}$) are presented in Figure 4.5 (e)-(f), demonstrating large, non-linear, incremental increases with reducing α.

The effect of the side-edge strips was found to be an increase the static pressure on the lower surface of the wing through constrained fluid flow (entrapment), and thus, due to the geometrical "opening" created when anhedral and cropping are introduced to a reverse delta wing, the placement of a metal strip in the gap created was required to prevent fluid escaping through the opening. Presented in Figure 4.5 is the effect of closing off of the rear portion of the lower wing surface, denoted by the ◆ symbol, and referred to hereafter as the closed configuration. All cropped and anhedraled wing models with side-edge strips were tested in the closed configuration. The closure of the rear portion of the lower wing surface can be seen schematically in Figure 3.7 (b), and is described in Section 3.3. The clean wing configuration refers to the same test model without this closure or the application of side-edge strips. An increase in the lift-curve slope is observed, however, unlike the addition of the SESs, closing off of the rear planform does not resemble that of conventional Gurney-flaps, or an induced camber effect. There is approximately zero lift force at $\alpha = 0$, however, from the increased lift-curve slope, C_{Lmax} has increased to 1.055, an increase of 7% over the clean-wing cropped, anhedraled configuration ($\delta_A = 15°$, 30% cropped), while α_{SS} has remained similar at $36° - 37°$. Evidently, as seen in Figure 4.5 (e), ΔC_L is approximately equal to that of the clean configuration. However, drag is increased at low angles of attack (see Figure 4.5 (f)), where an increase of 66% over the cropped $\delta_A = 15°$ RDW65 was observed at $\alpha = 0°$ for the closed wing, while the clean-wing variant was 19%. Thus, in the low-α regime, the closed configuration has a reduced lift-to-drag ratio over the clean, non-cropped wing. The closing of the rear planform is advantageous above $\alpha \geq 15°$, as the lift increment outweighs the drag increment (for $\delta_A = 15°$).

Figure 4.6 shows the impact of anhedral angle on the reverse delta wing equipped with side-edge strips ($h_{SES} = 2\%, 4\%$) for the 30% cropped reverse delta wing. Figure 4.6 (a) and (c) reveal that for a given α, C_L and C_D increase with decreasing δ_A and increasing h_{SES}. Comparing the 2% and 4% strip heights against all three tested anhedral angles, the 4% strip had a lower C_{Lmax} and α_{SS} than the 2% strip further indicating that increasing h_{SES} resulted in a greater extent of flow separation. In the same manner, in the high-C_L regime, for a given C_D, C_L increases with decreasing h_{SES} and δ_A (see Figure 4.6 (d)). At low angles of attack, below $\alpha = 12°$, the C_L for the SES equipped models are all above the baseline wing (30% cropped planar RDW65) and their respective clean wing configurations. Above $\alpha = 12°$, the lift of the $\delta_A = 30°$ SES equipped model is lower than baseline, while the drag coefficient follows closely to the baseline case, thus indicating that the $\delta_A = 30°$ model is not advantageous in freestream except at low angles of attack. Shown in Figure 4.6 (b), increasing δ_A and h_{SES} decreased the aerodynamic efficiency. The incremental change in lift and drag over the baseline configuration, presented in Figure 4.6 (e)-(f), for the cropped, anhedraled, reverse delta wings, demonstrate that large increments in lift (and drag) are obtained at low angles of attack, with the increment in lift increasing with decreasing angle of incidence, increasing h_{SES} and decreasing δ_A. This suggests that by promoting the entrapment of high-pressure fluid flow by the SES and with minimal anhedral, large increases in lift can be obtained, particularly at low α. Notably, there is an increase in the lift-to-drag ratio of the SES anhedraled wings over their clean configuration at low angles of attack.

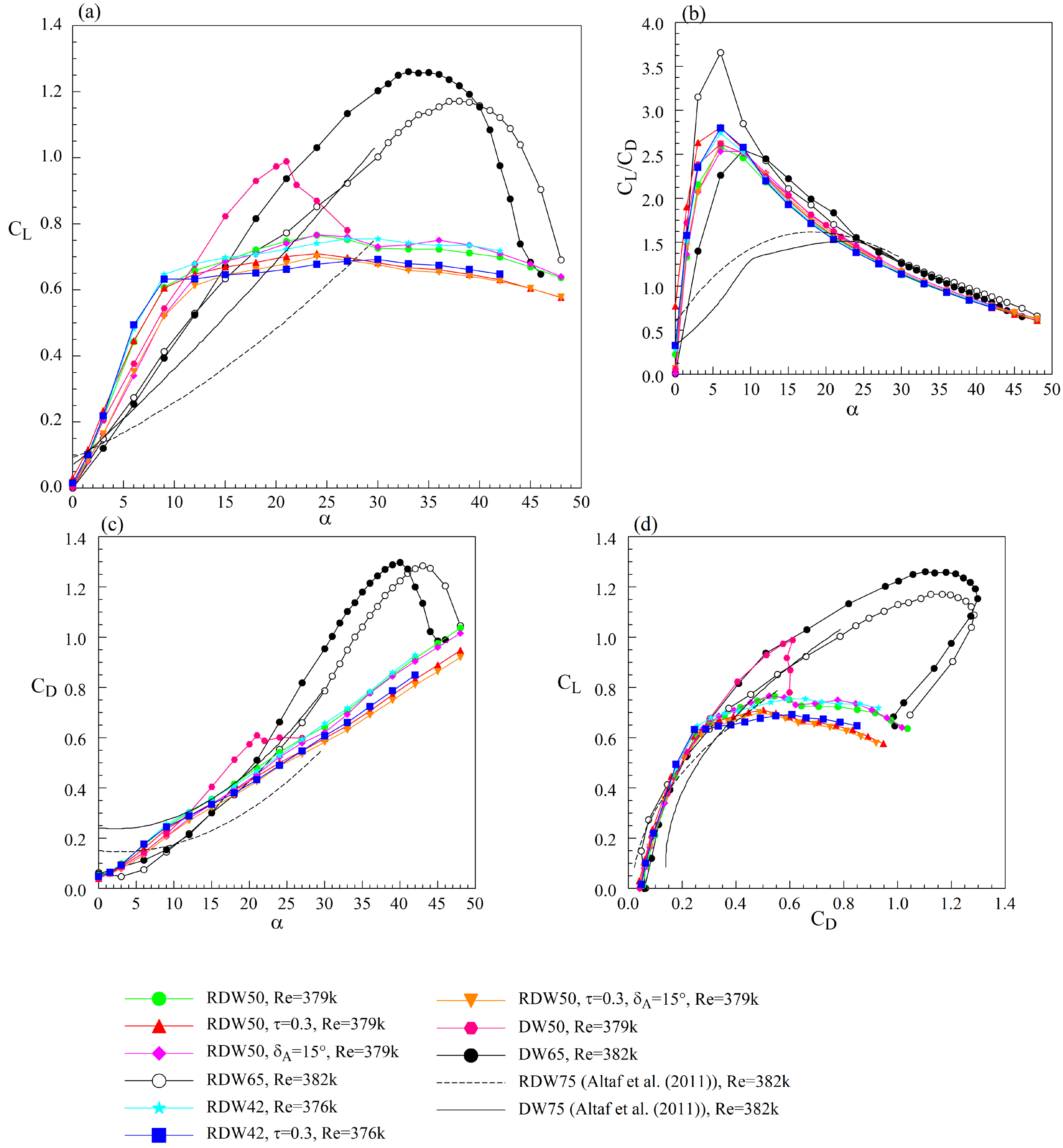

Figure 4.1: The impact of anhedral ($\delta_A = 15°$) and rear planform cropping (30%) on the aerodynamic coefficients of the non-slender reverse delta wing ($\Lambda = 50°, 42.5°$) outside of ground effect, presented alongside the baseline slender ($\Lambda = 65°$) and non-slender ($\Lambda = 50°, 42.5°$) delta wing and reverse delta wing results. The cropped and anhedraled coefficients are normalized by the original non-cropped, planar, wing surface area. Results for a $\Lambda = 75°$ slender model from Altaf et al. (2011) are included for comparison. The horizontal axes for (e)-(f) begin at $\alpha = 3°$ due to asymptotic behavior resulting from very small baseline values.

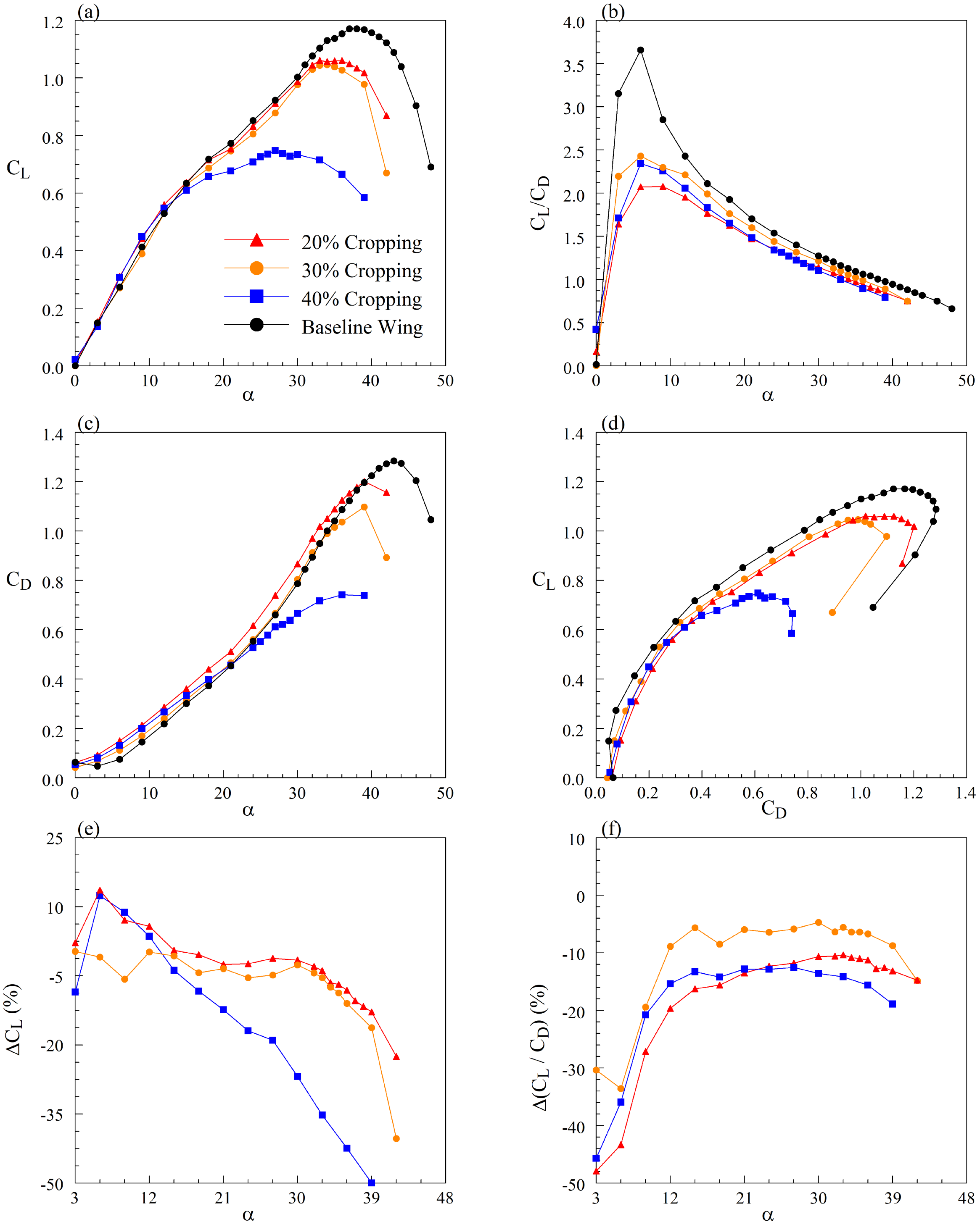

Figure 4.2: Impact of rear planform cropping on the aerodynamic coefficients of a slender reverse delta wing outside ground effect ($\Lambda = 65°$). (a)-(d) Coefficient curves, (e)-(f) lift and lift-to-drag ratio increments over baseline configuration. $\Delta C_L = (C_{LCW} - C_{LBW})/C_{LBW}$, where BW denotes the baseline non-cropped wing, and CW denotes cropped wing. $\Delta C_L/C_D$ follows similarly. Coefficients for the cropped wing models are normalized by the surface area of the non-cropped RDW65.

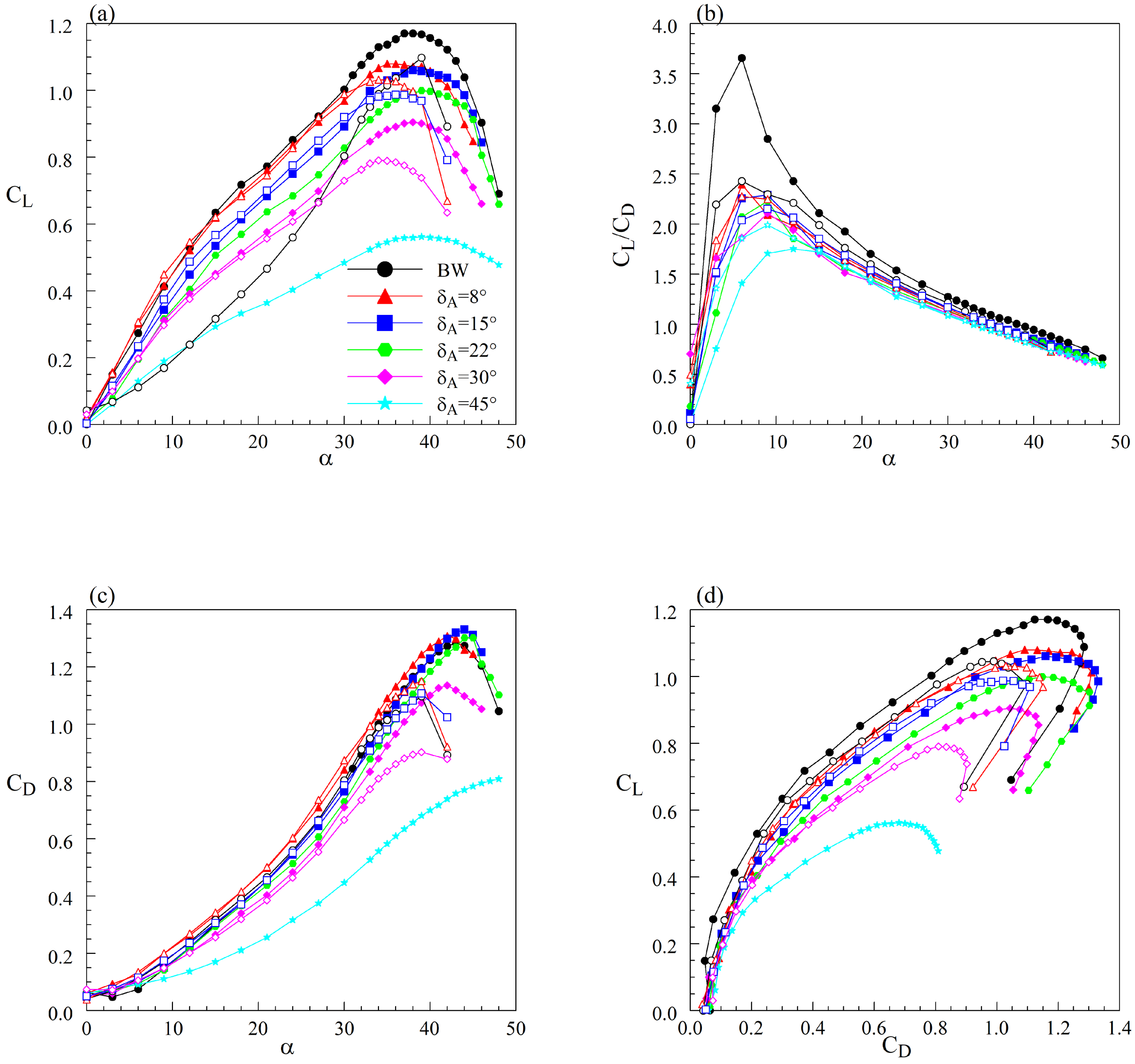

Figure 4.3: Impact of anhedral angle on the aerodynamic coefficients of a reverse delta wing outside of ground effect. Hollow symbols denote results for the 30% cropped planform. BW denotes the baseline wing, or the planar, non-cropped slender reverse delta wing. Coefficients for the anhedraled models are normalized by the surface area of the baseline reverse delta wing.

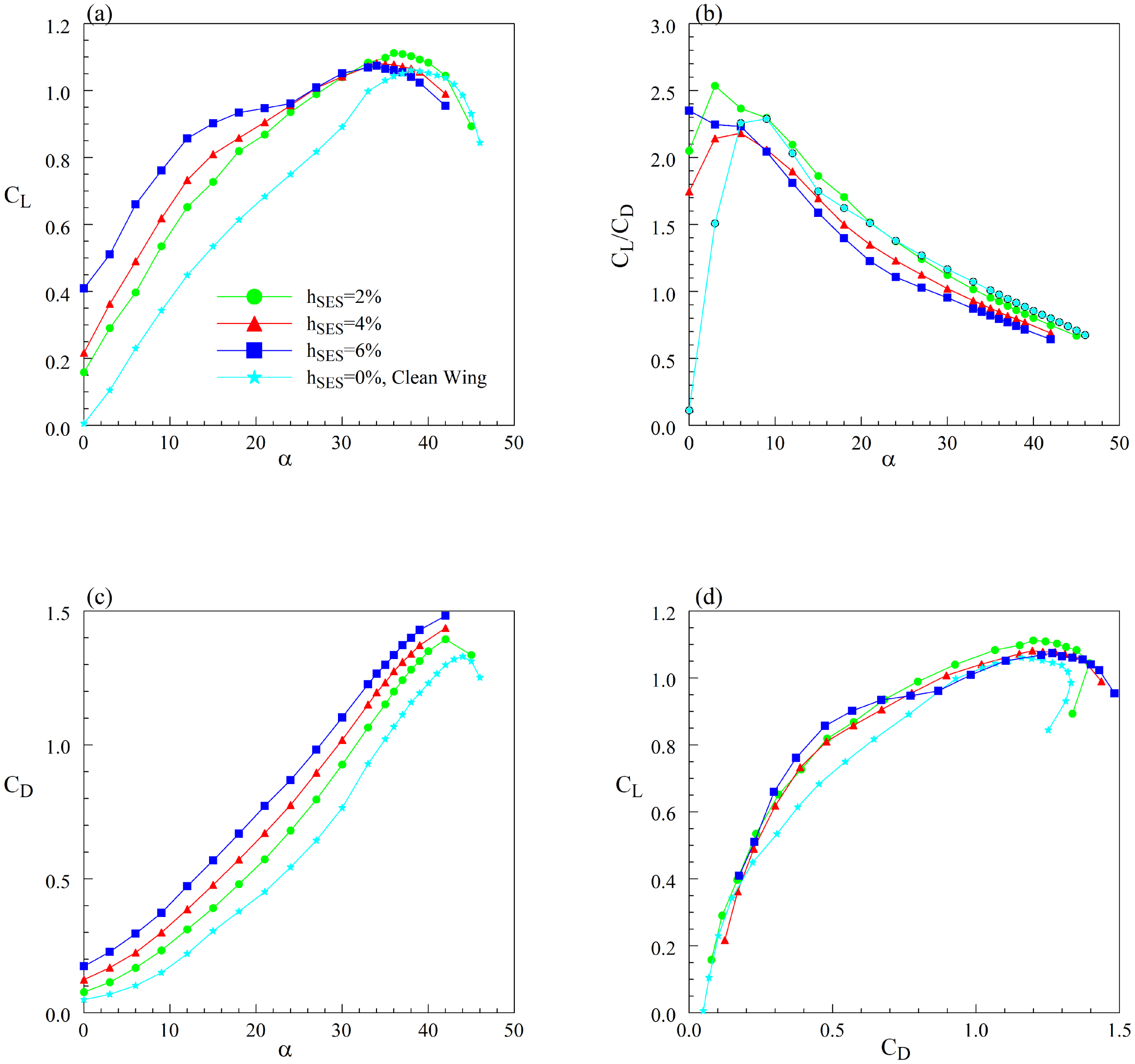

Figure 4.4: Impact of varying SES height on the aerodynamic coefficients of a $\delta_A = 15°$ reverse delta wing outside of ground effect. All coefficients are normalized by the surface area of the baseline, planar (non-anhedraled) slender reverse delta wing (see Table 3.1).

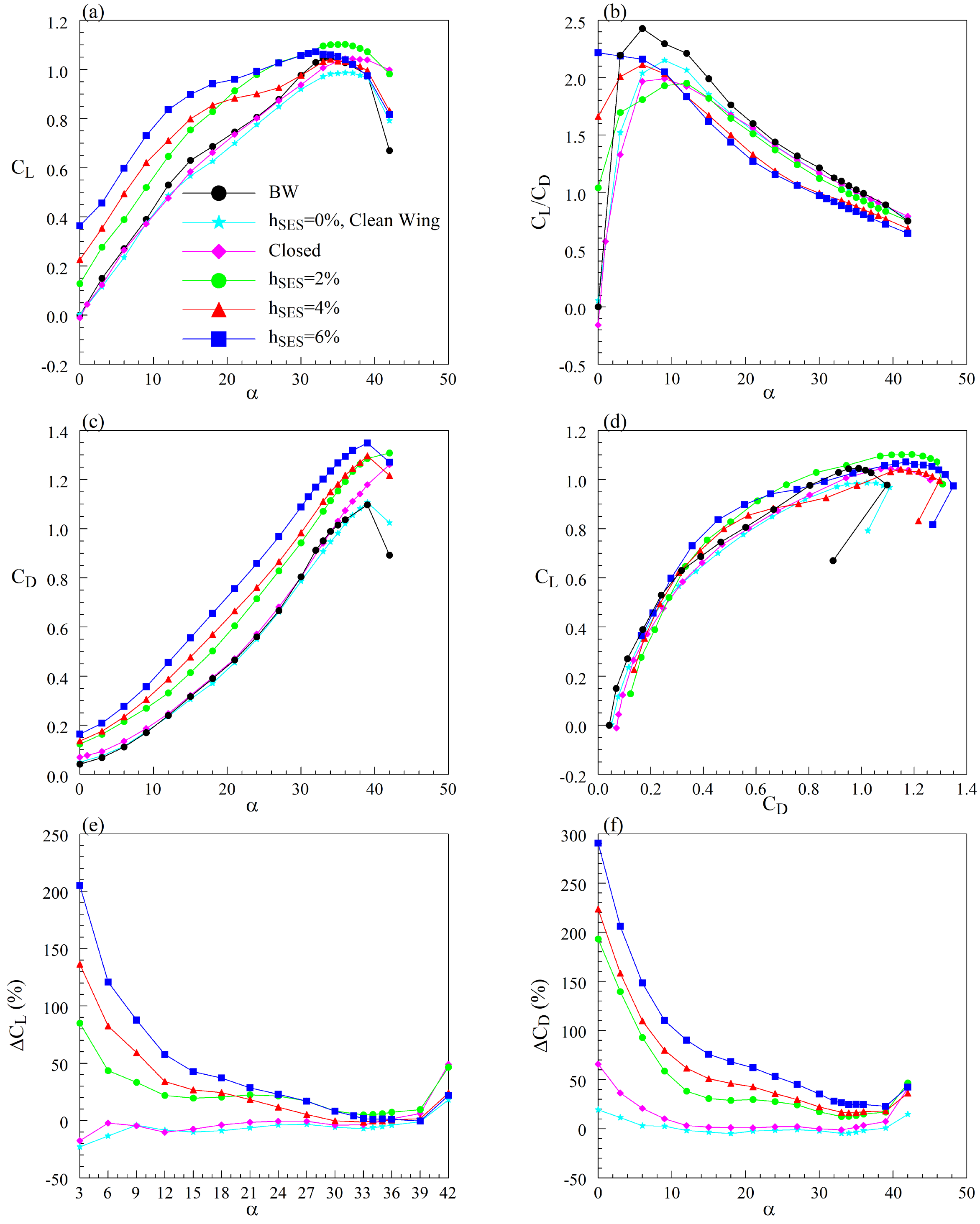

Figure 4.5: Impact of SES height on the 30% cropped, $\delta_A = 15°$ reverse delta wing outside of ground effect. BW denotes the baseline wing (30% cropped, $\delta_A = 0°$ RDW65). (a)-(d) Coefficient curves, (e)-(f) lift and drag increments ($\Delta C_L = (C_L - C_{LBW})/C_{LBW}$, ΔC_D follows similarly). All coefficients are normalized by the surface area of the baseline RDW65. Clean wing refers to the$\delta_A = 15°$, 30% cropped model, while closed indicates closure of the aft lower planform. The horizontal axis for (e) begins at $\alpha = 3°$ due to asymptotic behavior resulting from very small baseline values.

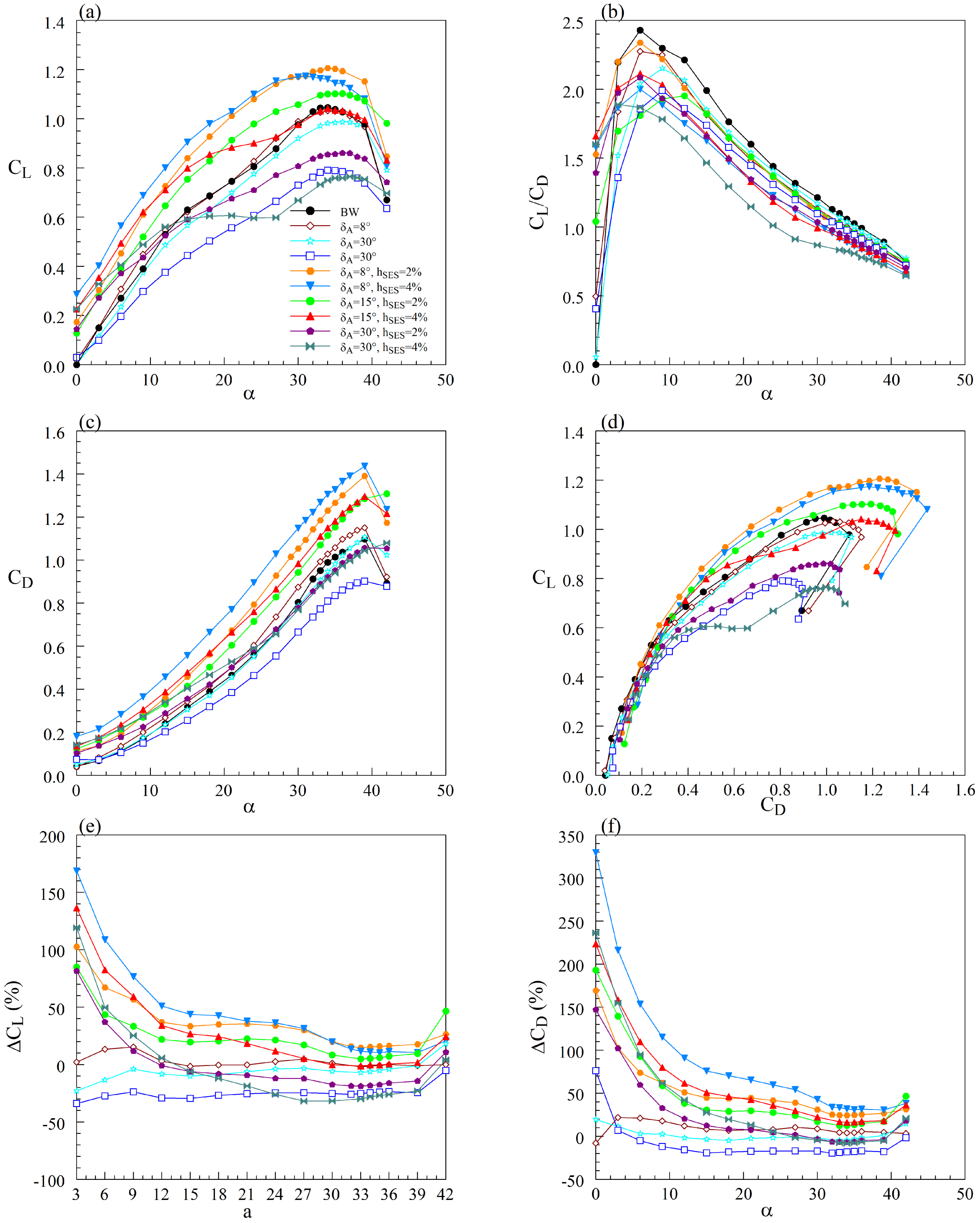

Figure 4.6: Impact of SES and anhedral angle on the 30% cropped reverse delta wing outside of ground effect. BW denotes the baseline wing (30% cropped, $\delta_A = 0°$ RDW65). (a)-(d) Coefficient curves, (e)-(f) lift and drag increments ($\Delta C_L = (C_L - C_{LBW})/C_{LBW}$, ΔC_D follows similarly). All coefficients are normalized by the surface area of the baseline RDW65. The horizontal axis for (e) begins at $\alpha = 3°$ due to asymptotic behavior resulting from very small baseline values.

4.2 INSIDE GROUND EFFECT: RDW AND DW

In this section, the impact of ground proximity on the slender and non-slender reverse delta wing and delta wing will be discussed.

4.2.1 Baseline Slender Wings in Ground Effect

The in ground effect results for the baseline slender delta wing and reverse delta wing are presented in Figure 4.7 and Figure 4.8, respectively. In ground effect, the delta wing continues to outperform the reverse delta wing, with freestream conditions being approximately reached at $h/c = 0.6$ for the delta wing, and $h/c = 0.4$ for the reverse delta wing. With increasing ground proximity, the C_L and C_D increase for both baseline models may be due to an increase in static pressure on the lower surface from ground effect, and to a lesser extent for the delta wing, to an increase in the strength of the LEVs. An increased $C_L - \alpha$ curve slope is observed in Figure 4.7 (a) and Figure 4.8 (a), as a result of the static pressure and RAM pressure in ground effect. At the lowest ground clearance, a leftward shift in the $C_L - \alpha$ curve is observed, characteristic of an increase in camber or flap deployment on rectangular wings, possibly a result of the boundary layers of the wing and the fixed ground merging at extremely low ground clearances.

Earlier stalling is observed for both wing models, with α_{SS} decreasing with decreasing h/c. Stall promotion for the delta wing is likely due to the promotion of the breakdown of the LEVs, and for the reverse delta wing from enhanced disruption of the SVFs, in both cases resulting from the increased adverse pressure gradient. Figure 4.7 (a) reveals a 5° maximum stall promotion for the baseline delta wing ($\alpha_{SS} = 30°$), and Figure 4.8 (a) demonstrates a 3° promotion for the reverse delta wing ($\alpha_{SS} = 35°$). C_{Lmax} for the delta wing increased to a maximum of 1.42 (1.26 in freestream), versus 1.18 (1.17 in freestream) for the reverse delta wing, both at $h/c = 0.01$, the lowest ground clearance achievable for the experimental set-up used. Below $\alpha = 9°$, the reverse delta wing and delta wing C_L in ground effect are approximately equal, while this was true for $\alpha = 12°$ outside of ground effect, implying a promotion of the development of the LEVs vortex lift in ground effect, possibly due to accelerated flow over the upper surface.

The ΔC_L increments shown in Figure 4.7 (e) and Figure 4.8 (e), the incremental lift increase in ground effect over the freestream value, demonstrate that the delta wing lift increment is higher than that of the reverse delta wing. This further supports the conclusion that the delta wing LEVs are strengthened with increasing ground proximity, increasing the vortex lift component relative to OGE conditions. The lift increment for both baseline models, for $h/c \leq 20\%$, increases non-linearly with decreasing incidence angle. The greatest lift increment is at the lowest ground clearance and lowest angle of attack, a result of the RAM pressure on the windward surface. For both models, this is primarily in the trailing-edge region, with the regular delta wing geometry particularly advantageous in this regard due to its greater percent area extent in the trailing edge region. This, combined with the aforementioned strengthened LEVs is the likely cause of the greater lift increment of the regular delta wing as compared to the reverse delta wing. Finally, the variation of C_L at a fixed angle of incidence, with varying ground proximity is presented in Figure 4.7 (f) and Figure 4.8 (f). For both baseline wing models in ground effect, there is a non-linear decrease in lift force with increasing h/c. At higher angles of attack both models become increasingly insensitive to changing ground proximity, a result of both the separated flow over the upper surfaces and stalling of the respective models, but which may be to a larger extent due to a large portion of the wing being out of the influence of ground effect at large angles of attack, except for the trailing edge region. This implies that the largest benefit with ground effect, is in the low-α regime, at low h/c.

The models may not have reached freestream C_D values at $h/c = 0.6$ in this experiment due to a possible overcorrection of the drag coefficient from removing the drag from the wing support-body system, as at a high angle of attack, and/or a high ground clearance, the fixed ground plane is nearer the cylinder in the centre of the wind-tunnel (see Figure 3.3 (a)), which may reduce drag on the cylinder from the cylinder acting in ground effect. However, C_D follows the C_L trend for both wings (see Figure 4.7 (c) and Figure 4.8 (c)), with the drag increments (not presented here) for the delta wing exceeding that of the reverse delta wing, which may be due to the increased strength of the LEVs increasing the induced-drag of the delta wing, and the increased RAM pressure in the trailing edge region. The increased drag coefficient with decreasing h/c is a distinctly different result than that typically observed for rectangular wings in ground effect. C_L/C_D for both baseline wings is reduced relative to the out-of-ground effect baselines (see Figure 4.7 (b) and Figure 4.8 (b)), however, while at moderate to high angles of attack ($\alpha > 24^\circ - 27^\circ$) the lift increment for the delta wing is offset by its drag increment and the lift-to-drag ratios collapse. At low angles of attack, the reverse delta wing C_L/C_D is higher than that of the delta wing in ground effect, and in particular, $(C_L/C_D)_{max}$. For example, at $h/c = 0.1$, $(C_L/C_D)_{max} = 2.61$ for the reverse delta wing, and 2.17 for the regular delta wing. In the low-α regime, at low h/c, there is an increase in C_L/C_D, demonstrating the need to operate at low ground clearances and angles of attack to optimize the benefits of ground effect (greatest lift and aerodynamic efficiency increments).

4.2.2 Cropped Reverse Delta Wings in Ground Effect

As discussed in Section 4.1.3, moderate rear planform cropping of the reverse delta wing ($\leq 30\%$) outside of ground effect did not significantly reduce the lift or increase the drag over the baseline wing, prior to premature stalling. The cropped RDW inside ground effect, at varying ground proximities is shown in Figure 4.9. For reference, the results for the 10% h/c baseline non-cropped RDW65 is included for comparison in Figure 4.9 (a)-(d). As expected, the lift-curve slope of the cropped wing increases with increasing ground proximity, although at a higher rate than the non-cropped wing likely due to increased ground proximity from a smaller root chord, thus causing a greater C_L at low ground clearances and angles of attack. With increased proximity however, the drag increased considerably, which may be due to both the RAM pressure increase and an increased wake extent from enhanced SVF disruption caused by the three-dimensional flow induced by the cropping. Freestream conditions are reached by $h/c = 60\%$ for the cropped model in ground effect. Unexpectedly, at low angles of attack with close ground proximity, for $h/c \leq 10\%$ for $\alpha = 0°$, and $h/c \leq 5\%$ for $\alpha = 3° - 6°$, there is a diminishing benefit of decreasing ground clearance, and in the case of $\alpha = 0°$, there is actually a force reduction (see Figure 4.9 (e)). This is in contrast to the higher incidence angles, where with increasing ground proximity the lift force increases non-linearly with decreasing ground clearance and with increasing angle of incidence until stall. As well, this contradicts the findings of the baseline wing in ground effect in the low-α regime at low ground clearances, where significant increases in lift for $\alpha > 3°$ and negligible change for $\alpha = 0°$ were observed (Figure 4.8 (f)).

The cropped RDW65 stalled earlier than the baseline wing and the cropped wing outside of ground effect, with α_{SS} decreasing with increasing ground proximity. However, unlike the non-cropped wing, an increase in C_{Lmax} for the cropped RDW65 can be observed with increasing ground proximity, with an increase of 8% for $h/c = 10\%$. This further implies that due to the increased ground proximity permitted the planform cropping resulted in an increase in the impact ground effect over the baseline wing, while a weight reduction is additionally achieved from the removal of a portion of wing. While an increase in C_D with increasing ground proximity was observed, the lift-to-drag ratio was approximately equal to the cropped wing in the freestream (4.9 (b)). The increased lift in ground effect for the cropped model resulted in, at a fixed lift coefficient in the high lift regime, a drag reduction with increasing ground proximity as the wing is able to operate at a reduced angle of attack to achieve an equivalent C_L (see Figure 4.9 (d)). The reduction in pressure and profile drag from the reduced incidence outweighs the increased drag from the enhanced separated flow resulting from the ground induced adverse pressure gradient.

4.2.3 Anhedraled Reverse Delta Wings in Ground Effect

The effect of anhedral on the non-cropped reverse delta wing in ground effect is presented in Figure 4.10. For each anhedral angle, with the trailing edge parallel to the ground and with an effective angle of attack as reported in Table 3.1, the lift and drag coefficients decrease non-linearly with increasing ground clearance until reaching freestream values at approximately $h/c = 60\%$ (Figure 4.10 (a) and (c)). At this fixed angle of attack, α_{eff}, C_L was found to increase greatly below $h/c = 10\%$ with maximum values reached at the lowest testable ground clearance, thus amplifying the effect observed at low angles of attack and ground clearance for the baseline reverse delta wing. With increasing anhedral up to $\delta_A = 30°$, the lift coefficient increased greatly in ground effect for $h/c \leq 10\%$. C_L for $\delta_A = 45°$ was below $\delta_A = 30°$ in ground effect, likely due to the significant reduction in surface area and higher effective angle of attack outweighing the benefit of the further increase in anhedral.

The relationship between lift and drag in ground effect for the anhedraled models was approximately linear (Figure 4.10 (c)), and at a fixed C_L, drag increased with increasing anhedral. The lift and drag increments over the same configuration in freestream is shown in Figure 4.10 (e)-(f). The largest increment for both lift and drag over the same configuration in freestream is seen for the $\delta_A = 15°$ reverse delta wing. A maximum increase over freestream for C_L and C_D of 269% and 193% for the $\delta_A = 15°$ model was observed at $h/c = 0.01$. In terms of the lift-to-drag ratio (see Figure 4.10 (d)) however, despite the significant increase in lift at with decreasing ground clearance, the corresponding increase in C_D led to a marginal improvement in C_L/C_D except in extreme ground effect ($h/c \leq 10\%$). The highest lift coefficient achieved was $C_L = 0.983$ for $\delta_A = 30°$, and the highest drag coefficient recorded was $C_D = 0.491$ for $\delta_A = 45°$, both at $h/c = 0.01$ while the greatest C_L/C_D ratio is for $\delta_A = 15°$. This suggests that there is some optimum anhedral angle or geometry for lift augmentation while maintaining the aerodynamic efficiency in ground effect. Notably, as the anhedral angle increases, the effective angle of attack increases when keeping the trailing edge parallel to the ground. At low ground clearances, the cavity formed may thus further trap the air under the wing, forming a quasi "air tunnel" geometry. The increase in lift with increasing anhedral and ground proximity suggests the RAM pressure and "air tunnel" is responsible for the increase in static pressure, in addition to the effects of the ground. The increased drag coefficient may be a result of an increase in extent of the separated flow in ground effect, in addition to the pressure drag resulting from the "air tunnel" effect.

The effect of anhedral on the cropped reverse delta wing in ground effect, each at their respective α_{eff}, is presented in Figure 4.11. C_L and C_D follow similar trends to their non-cropped counterparts, albeit at a lower magnitude at low ground clearances (see Figure 4.11 (a) and (c)) for C_L and at most ground clearances for C_D. The reduced lift coefficient may be a result of two factors: (i) reduced surface area of the cropped model reducing impact of static pressure rise on lower surface, (ii) an open aft planform section that doesn't prevent higher pressure flow leakage at the trailing edge. The reduced drag coefficient may be due to the lower pressure drag and from a reduced extent of separated flow (from this leakage) as compared to the non-cropped model. The reduction of C_L and C_D with the introduction of cropping contradicts the results of the non-anhedraled wing. This suggests that the RAM pressure increase and formation of the "air tunnel" like effect of the non-cropped anhedraled RDW overwhelms the increased ground proximity of the cropped model (due to its reduced root chord).

The lift increment over the equivalent configuration outside of ground effect, presented in Figure 4.11 (e), shows large increments in ground effect of the cropped, anhedraled wings, with a maximum lift increment of 230% found for the $\delta_A = 8°$ cropped wing, similar to that of the non-cropped wing, which achieved 269% over its equivalent freestream configuration. The maximum increment in both cases was achieved for the $\delta_A = 8°$ and $\delta_A = 15°$ models, both cropped and non-cropped. The lift-to-drag ratio is increased over the non-cropped configuration and freestream conditions at low ground clearances (see Figure 4.11 (b)). For both the non-cropped and cropped configurations, the greatest overall lift-to-drag ratio is observed for the $\delta_A = 15°$ configurations. The increased lift and C_L/C_D generated by the anhedraled RDW in ground effect at low angles of attack, here α_{eff}, and low h/c indicate that efficient flight is achieved in these flight regimes for WIG craft, and while rear planform cropping may reduce lift generation, weight reductions and improved aerodynamic efficiency counteract these losses. The equipment of side-edge strips as a passive control mechanism may further augment lift generation and enhance the "air tunnel" like effect observed here, and will be explored in detail in Section 4.3.

4.2.4 Impact of Non-Slenderness on DW and RDW in Ground Effect

The impact of non-slenderness was explored in ground effect, and is discussed in the following paragraphs. The results for the non-cropped, non-anhedraled, 50-degree swept delta wing in ground effect are presented in Figure 4.12. The force balance results for the non-cropped, non-anhedraled reverse delta wings in ground effect are presented in Figures 4.13-4.14.

Figure 4.12 (a) and (c), and Figure 4.13 (a) and (c) demonstrate that for the baseline non-slender wings, C_L and C_D increased with decreasing h/c, with maximum coefficients occurring at $h/c = 1\%$. As h/c decreased, for $\alpha \leq 9°$ the C_L-α slope increased for both the non-slender reverse delta wing and delta wing, leading to increased C_L with increasing ground proximity. Figure 4.12 (h) and Figure 4.13 (h) present C_L as a function of h/c, for DW50 and RDW50, respectively. Freestream values are observed at 40% ground clearance for the regular delta wing, and at 60% for the reverse delta wing, indicating a greater extent of influence the ground effect on the reverse delta wing than the regular delta wing, in contrast with the results observed for the slender baseline wings in ground effect (see Section 4.2). Notably, at low h/c, there is an evident non-zero lift force for the non-slender reverse delta wing at $\alpha = 0°$, in a manner similar to a leftward shift of the $C_L - \alpha$ curve with the introduction of camber on rectangular wings or the employment of trailing-edge flaps. Due to this non-zero intercept, unlike outside of ground effect, and unlike the slender wing, the non-slender reverse delta wing and delta wing do not have approximately equal lift coefficients below $\alpha = 9°$. Thus, below $\alpha = 9°$, the non-slender reverse delta wing outperformed the non-slender delta wing in terms of lift. An hypothesis for the cause of this unexpected finding may be that the non-slender reverse delta wing may accelerate flow over the upper surface in extreme ground effect from a flow restriction on the lower surface, thus creating a suction pressure on the upper surface. This finding, while possible to attribute to experimental error, is consistent for the non-slender reverse delta wings tested, and not reproducible on the slender configuration, casting doubt on sources of experimental error. Further study may elucidate either the source of error or the mechanism behind the phenomenon, including studies with a moving ground.

Further distinctions between the slender and non-slender cases are evident. The slender delta wing was seen to have a promotion of stall, with a reduced α_{SS} relative to the freestream conditions, while the non-slender delta wing had delayed stalling in ground effect, with an increase in α_{SS} to 24° at extreme ground proximity from 21° in freestream conditions. This may be a result of the separated-layer thinning on the non-slender delta wing in ground effect from flow acceleration over the upper surface, as well as from upward primary vortex movement in ground effect. The 50-degree non-slender RDW instead can be seen to have a promotion of stalling in ground effect (see Figure 4.13 (a)). The increase in $C_L - \alpha$ curve slope with increasing ground proximity led to the maximum lift coefficient increasing in ground effect for both the regular and reverse 50-degree swept delta wings. The slender reverse delta wing was observed to have little change in C_{Lmax} with ground effect (see Figure 4.8 (a)). For example, an increase of 36% and 30% at $h/c = 0.01$ in C_{Lmax} relative to freestream for DW50 and RDW50, respectively was found. The stalling trend for the DW50 remained sharp in ground effect, while the RDW50 had a gradual increase in C_L from approximately $\alpha = 9°$ to approximately $\alpha = 24°$ before plateauing. Notably, unlike the out of ground effect case, the RDW50 model remained near C_{Lmax} longer before gradually tapering off beyond $\sim \alpha = 39°$.

Force balance measurement results for the 42.5-degree swept wing are presented in Figure 4.14. A limited number of test cases were studied due to experimental constraints. With further decrease in sweep angle, from $\Lambda = 50°$ to $\Lambda = 42.5°$, the $C_L - \alpha$ slope further increased, leading to improved lift of RDW42 over RDW50 over the angles of incidence tested, except for the extreme ground proximity case $h/c = 1\%$ where the lift generated by RDW50 and RDW42 were approximately equal. For the two ground proximities tested until $\alpha = 36°$ ($h = 0.1c$ and $h = 0.2c$), there is a marked increase in C_{Lmax}, dissimilar to the freestream case, where the lift generation of RDW50 and RDW42 were close for $\alpha > 12°$. As the primary lift generation for the RDW is from the lower wing surface, and with ground effect the increase in pressure is primarily on the lower surface from the RAM effect, it is suggested that the increase in wing surface area at the front of the planform is partially responsible for the increase in the C_L increment more so than the freestream case. Ground effect is exploited further by the lower swept non-slender RDW from this surface area increase at the fore of the planform. Additionally, the chord is reduced, allowing the 42.5-degree swept RDW to be closer to the ground than the 50-degree wing. Further testing of stall characteristics and lift forces in the high-α regime with varying ground proximities may provide further clarity.

C_D for RDW50, DW50, and RDW42 followed a similar trend in ground effect to their freestream counterparts (see Figure 4.12 (c), Figure 4.13 (c) and Figure 4.14 (c)), with C_D for the reverse delta wings increasing monotonically with α, and C_D for the delta wing increasing non-linearly until reaching a local maximum when the delta wing stalls. An increase in drag production is observed with increasing ground proximity which may be a result of an increase in pressure drag corresponding to the increase in lift, as well as from an increasingly adverse pressure gradient promoting separated flow over the wing's upper surface. C_D for the RDWs exceeds that of DW50 below $\alpha = 12°$ (RDW50) and $\alpha = 15°$ (RDW42), at approximately the same angle of incidence as freestream conditions. For RDW50, DW50, and RDW42, the drag coefficient increased with increasing ground proximity, although notably, the drag force lowered to approximately the freestream minimum drag coefficient at $\alpha = 0°$, unlike C_L for the RDW50 and RDW42. In general, C_D for RDW42 exceeded that of RDW50, except at the extreme ground proximity of $h/c = 0.01$. While the drag force increased with ground proximity, the increase in lift out-performed that of the drag for both the reverse and regular non-slender delta wings, leading to improved C_L/C_D in ground effect, which is in contrast to the slender RDW65 and DW65 (see Figure 4.7 (b) and Figure 4.8 (b)). In the low-α regime, the C_L/C_D for RDW42 exceeded that of RDW50, likely due to the increase in ground proximity achieved by the reduced chord of the RDW42, while the inverse trend was observed in the moderate-α regime, due to increased drag of the RDW42 over that of RDW50. The lift-to-drag ratios collapsed in the high-α regime for all three non-slender wings, approximating their freestream values.

As presented in Figure 4.12 (e), Figure 4.13 (e) and Figure 4.14 (e), ΔC_L increases non-linearly with decreasing α and h/c for the non-slender delta and reverse delta wings, though the reverse delta wing increment is much larger. The greatest increments in C_L were found in the low-α regime for low ground clearances, sharply increasing for $\alpha \leq 9°$ and $h/c \leq 20\%$. The RDW50 reached a maximum increment over freestream values of 130% at $\alpha = 3°$ and $h = 0.01c$, while the RDW42 and DW50 increased by 115% and 80%, respectively, at the same ground clearance and angle of attack. Thus, the 50-degree swept reverse delta wing had the largest lift increment over freestream conditions of the three non-anhedraled, non-cropped, non-slender wings tested in ground effect. Similar to ΔC_L, ΔC_D, increased non-linearly with decreasing α in the low-α regime and for $h/c < 40\%$, though behaviour at extremely low-α is inconclusive (Figure 4.12 (g), Figure 4.13 (g), Figure 4.14 (g)). Figure 4.13 (f) and Figure 4.14 (f) reveal that for the non-slender wings reverse delta wings, there is an increase in the lift-to-drag ratio over their OGE counterparts, with increasing efficiency with decreasing α. In general, maximum $\Delta \frac{C_L}{C_D}$ was achieved at $h = 0.1c$, except at low angles of attack due to the non-zero lift at low h/c and α as aforementioned. These non-slender wings had minimal change in efficiency (i.e. $< 10\%$) for $\alpha > 6° - 9°$, indicating that significant increases in lift may be observed in ground effect with minimal change in efficiency at most angles of attack, with large improvements below $\alpha = 9°$, in a manner similar to their slender counterparts.

The RDW50 non-slender reverse delta wing was then cropped at 30% of the root chord length. Note that the RDW42 wing was not tested further beyond its baseline case in ground effect (i.e., no cropped or anhedraled variants were tested). The results from the force balance measurements are presented in Figure 4.15. The 30% cropped RDW65 at $h/c = 10\%$ is included for reference. Figure 4.15 reveals consistent trends with wing cropping as the slender case. An increase in magnitude of the lift and drag coefficients relative to the non-cropped configuration was observed in ground effect was observed for $\alpha > 12°$ and $h < 0.2c$. This is likely due to the cropped wing being closer to the ground from a reduced root chord, increasing the effect of the ground on the wing's lower surface. Notably, unlike the slender case, at close ground proximities, i.e. $h/c \leq 0.1$, the cropped non-slender wing did not have increased lift and drag coefficients relative to its non-cropped counterpart. This reinforces the hypothesis that the increase in lift and drag for the RDW50 at low angles of attack and in close ground proximity is due to its significantly increased planform area, outweighing the effect of increased ground proximity as the cropped wing is closer to the ground. The static pressure rise on the non-cropped wing surface may thus outweigh the increase in lift from the RAM pressure increase observed on the cropped model. Presented in Figure 4.15 (d)-(e) are the lift and drag increments of the cropped RDW50 over the same wing in the freestream. For $h/c \leq 0.4$, there is an increase in both ΔC_L and ΔC_D with increasing ground proximity and angle of incidence. While the non-slender reverse delta wing stalls in the freestream at a low angle of attack, the saddle-like increment curves inside ground effect suggest that the pressure rise on the lower surface is responsible for the increased C_{Lmax} and delayed α_{SS}, similar to the non-cropped wing (see Figure 4.13 (e) and (g)). The lift-to-drag ratios for the cropped RDW50 (see Figure 4.15 (b)) increase with increasing ground proximity in the low-α regime, and collapse into a small range of values for $\alpha > 12°$, indicating that at lower angles of attack the impact of ground effect is more beneficial, similar to the non-cropped case. The lift-to-drag ratios approximate freestream in the moderate- to high-α regimes. Thus, cropping of both the slender and non-slender reverse delta wing leads to significant weight reduction advantages, with minor lift and drag penalties outside of ground effect and inside of ground effect.

The impact of anhedral on the non-slender reverse delta wing is shown in Figure 4.16, for an anhedral angle of $\delta_A = 15°$, selected based on the X-114 aircraft and slender RDW results. Both the cropped (30%) and non-cropped anhedraled RDWs are shown alongside the RDW65 $\delta_A = 15°$ model for comparison. Each test model is at its effective angle of attack, α_{eff}, which corresponds to the angle at which the trailing edge of the model is parallel to the ground (see Table 3.1). In a manner similar to the slender reverse delta wing in ground effect, the anhedraled wing sees a larger impact of ground proximity on the lift and drag forces than the non-anhedraled model, with an increase in C_L and C_D for $h/c < 20\%$. Here, the non-cropped anhedraled configuration has larger lift and drag forces in ground effect than the 30% cropped model, suggested to result from the increase in the “air tunnel” effect as fluid flow is trapped/stagnated in the cavity beneath the non-cropped, anhedraled RDW translating dynamic pressure to a static pressure rise on the windward surface of the wing. While the cropped non-slender reverse delta wing may be closer to the ground, the leakage of high pressure flow at the rear of the planform is suggested to outstrip the increase in RAM pressure, causing the non-cropped anhedraled wing to have a higher lift coefficient in ground effect than the cropped model, in addition to the loss of surface area as described prior. Notably, the relationship between C_L and C_D is nearly linear, as Figure 4.16 (d) reveals, with maximum increments of lift and drag over the freestream case of 76% and 70% observed for ΔC_L and ΔC_D at $h/c = 0.01$, respectively, for the non-cropped anhedraled RDW50. However, the C_L improvement overwhelms that of the C_D penalty, resulting in an improved lift-to-drag ratio relative to the outside of ground effect configuration, and to the baseline non-slender configuration in ground effect (see Figure 4.16 (b)). The addition of anhedral in ground effect on the non-slender reverse delta wing rendered an improved lift-to-drag ratio relative to the freestream equivalent configuration, and the baseline RDW50 in ground effect.

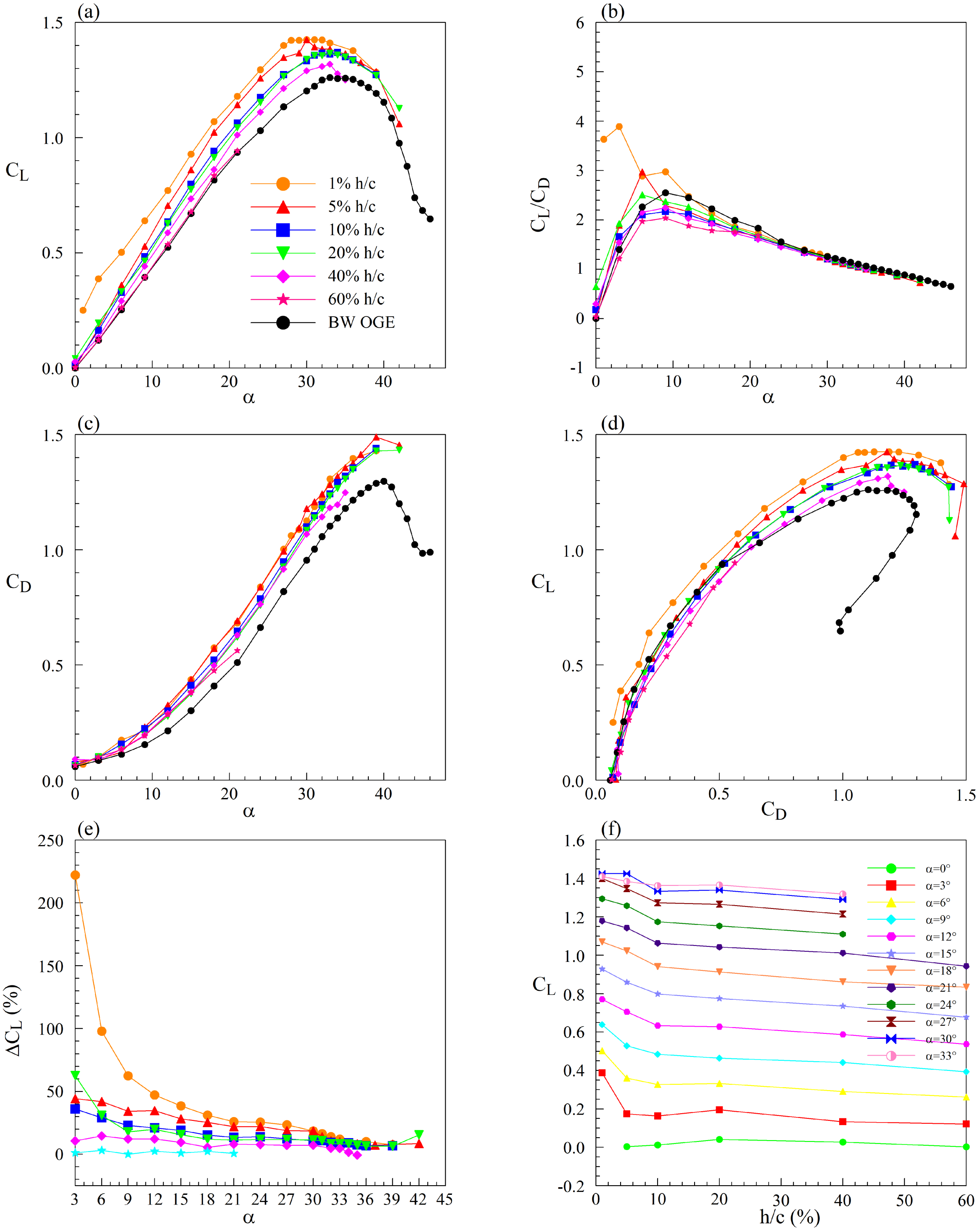

Figure 4.7: Impact of ground proximity on the slender delta wing. Baseline slender delta wing (denoted BW) out of ground effect (OGE) included for comparison. (a)-(d) Coefficient curves, (e) lift increment ($\Delta C_L = (C_L - C_{LBW})/C_{LBW}$), (f) variation with ground proximity. The horizontal axis for (e) begins at $\alpha = 3°$ due to asymptotic behavior resulting from very small baseline values.

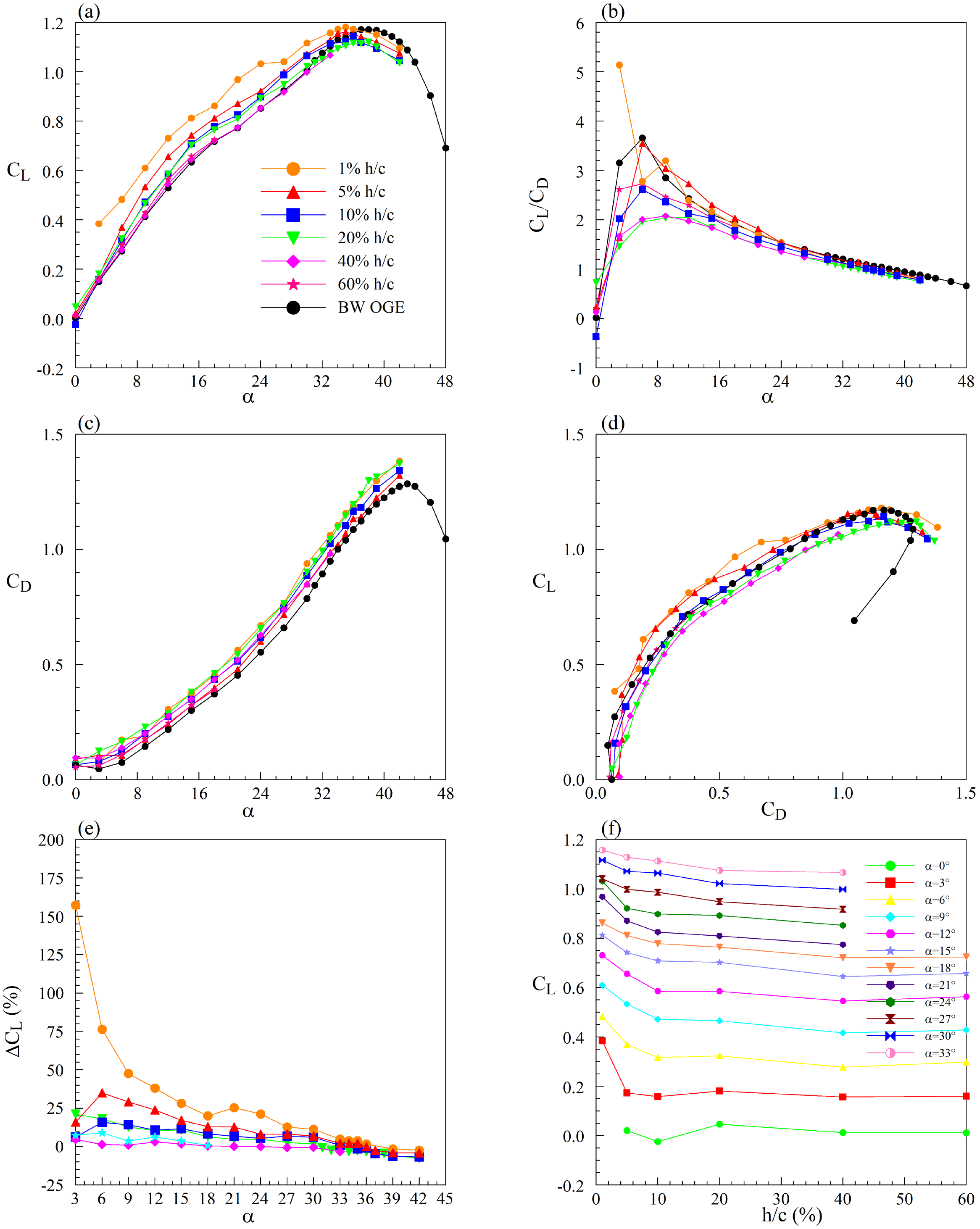

Figure 4.8: Impact of ground proximity on the slender reverse delta wing. Baseline slender reverse delta wing (denoted BW) out of ground effect (OGE) included for comparison. (a)-(d) Coefficient curves, (e) lift increment ($\Delta C_L = (C_L - C_{LBW})/C_{LBW}$), (f) variation with ground proximity. The horizontal axis for (e) begins at $\alpha = 3°$ due to asymptotic behavior resulting from very small baseline values.

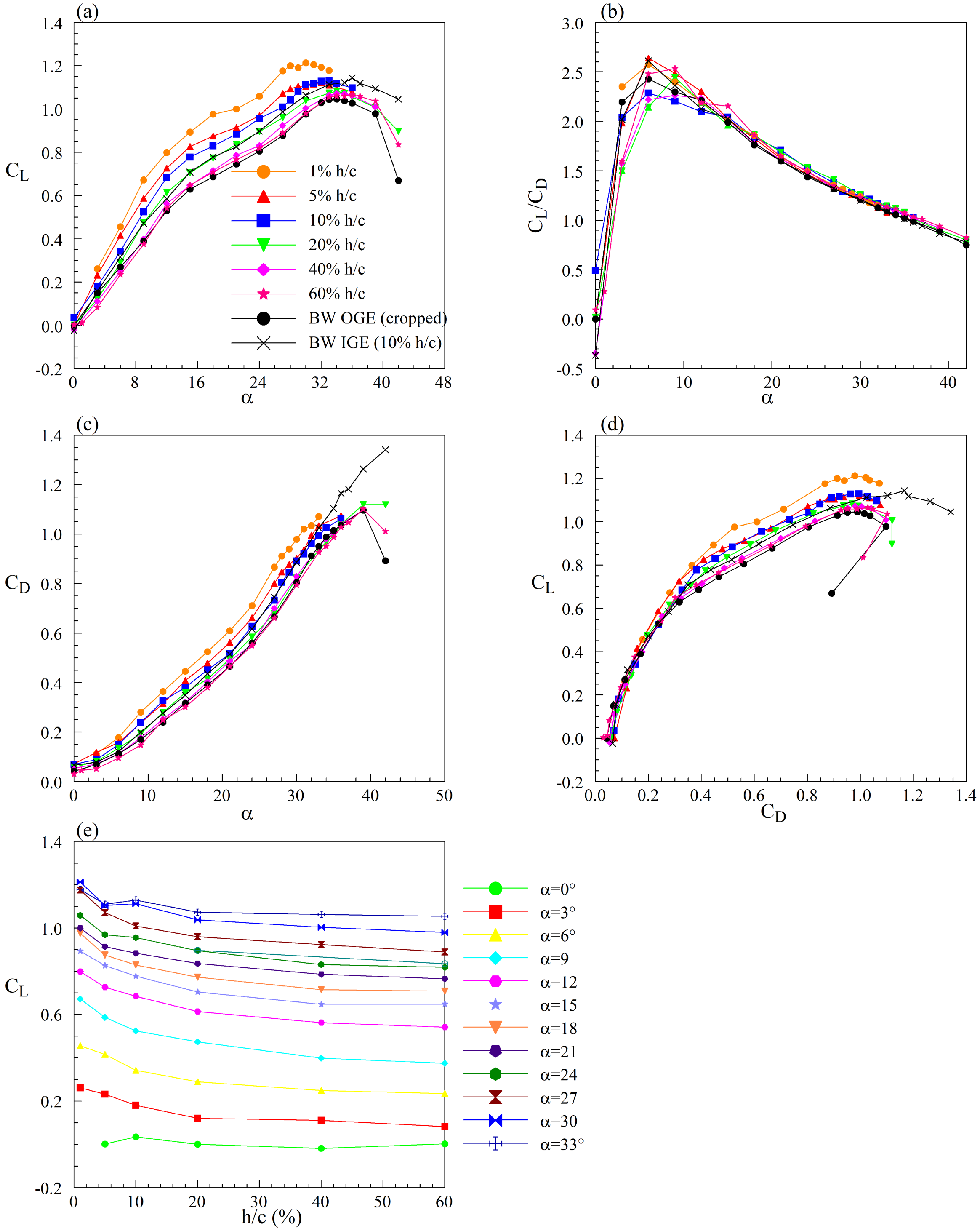

Figure 4.9: Impact of a 30% cropped planform on the slender RDW in ground effect: (a)-(d) coefficient curves, (e) variation with ground proximity. 10% h/c non-cropped RDW included for comparison, BW denotes the baseline RDW65 (non-cropped), with OGE and IGE denoting out and in ground effect, respectively. All coefficients are normalized by the surface area of the baseline RDW65.

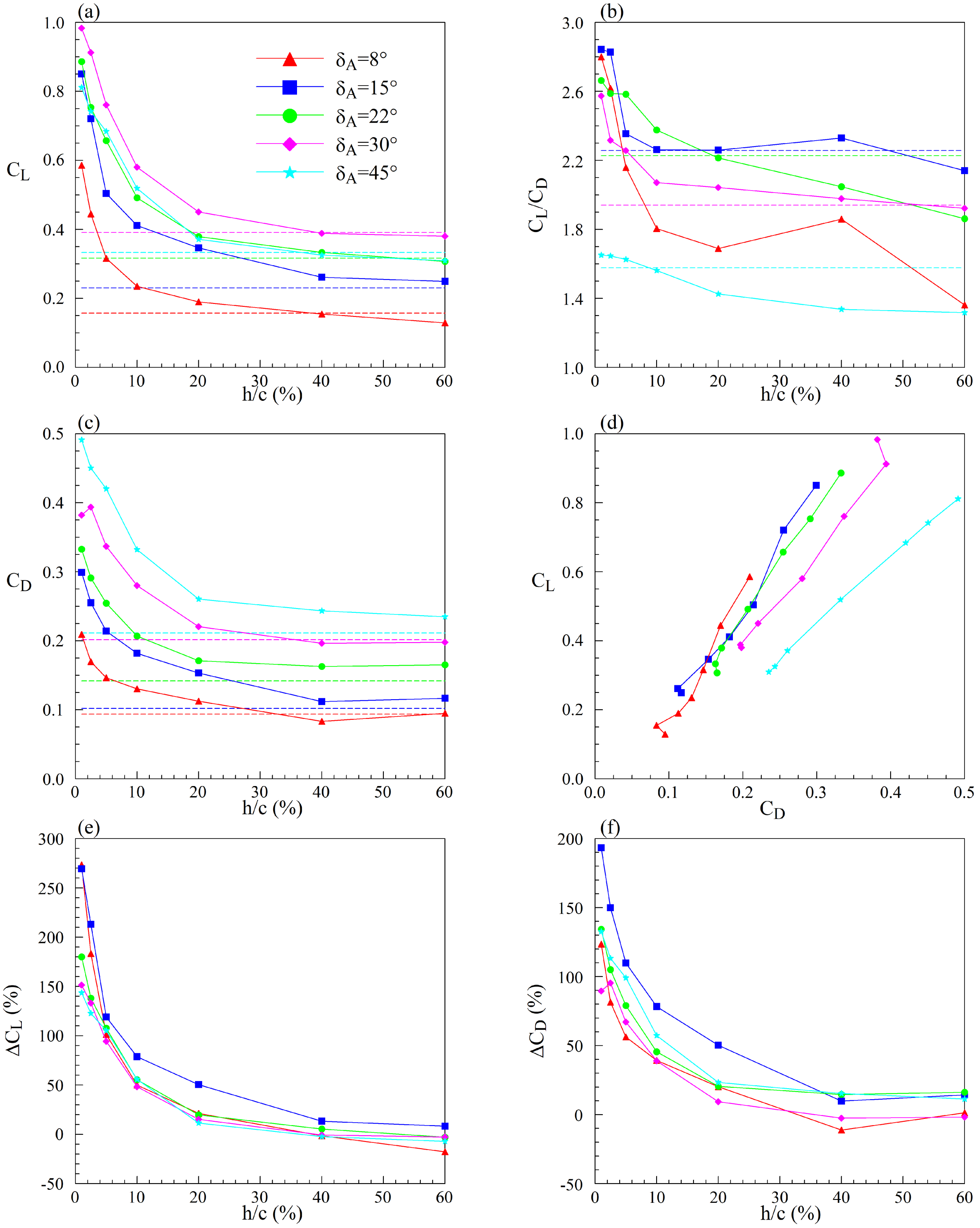

Figure 4.10: Impact of anhedral angle on the slender RDW in ground effect, at the angle of attack at which the trailing edge is parallel to the ground: (a)-(d) coefficient curves, (e)-(f) increment over the equivalent outside of ground effect (OGE) configuration or $\Delta C_L = (C_{L_{GE}} - C_{L_{OGE}})/C_{L_{OGE}}$. ΔC_D follows similarly. GE denotes the in ground effect results. Dashed lines denote OGE results. All coefficients are normalized by the surface area of the original, planar RDW65.

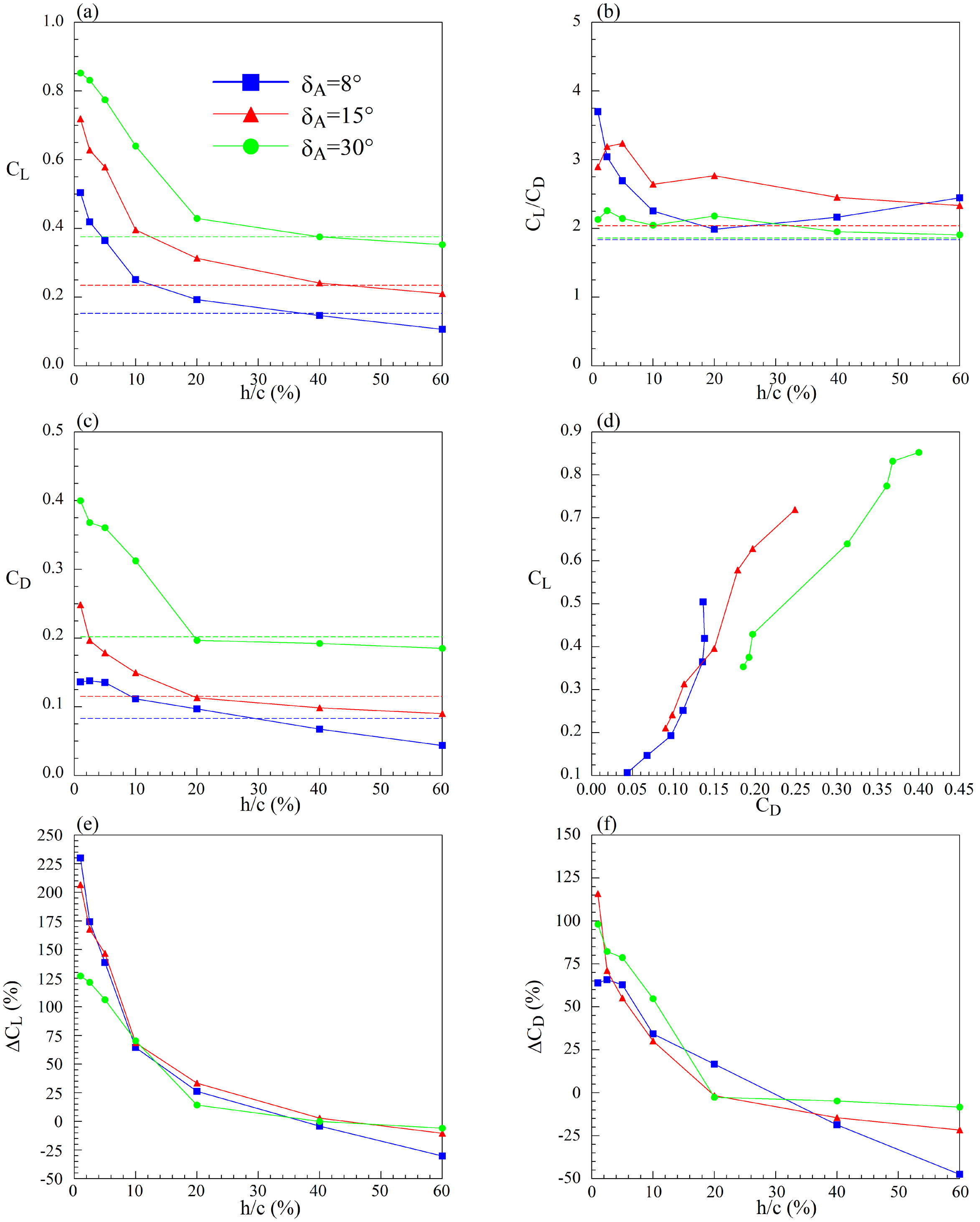

Figure 4.11: Impact of anhedral angle on the 30% cropped slender RDW in ground effect, at the angle of attack at which the trailing edge is parallel to the ground: (a)-(d) coefficient curves, (e)-(f) increment over the equivalent outside of ground effect (OGE) configuration or $\Delta C_L = (C_{L_{GE}} - C_{L_{OGE}})/C_{L_{OGE}}$. ΔC_D follows similarly. GE denotes the in ground effect results. Dashed lines denote OGE results. All coefficients are normalized by the surface area of the original, planar, non-cropped RDW65.

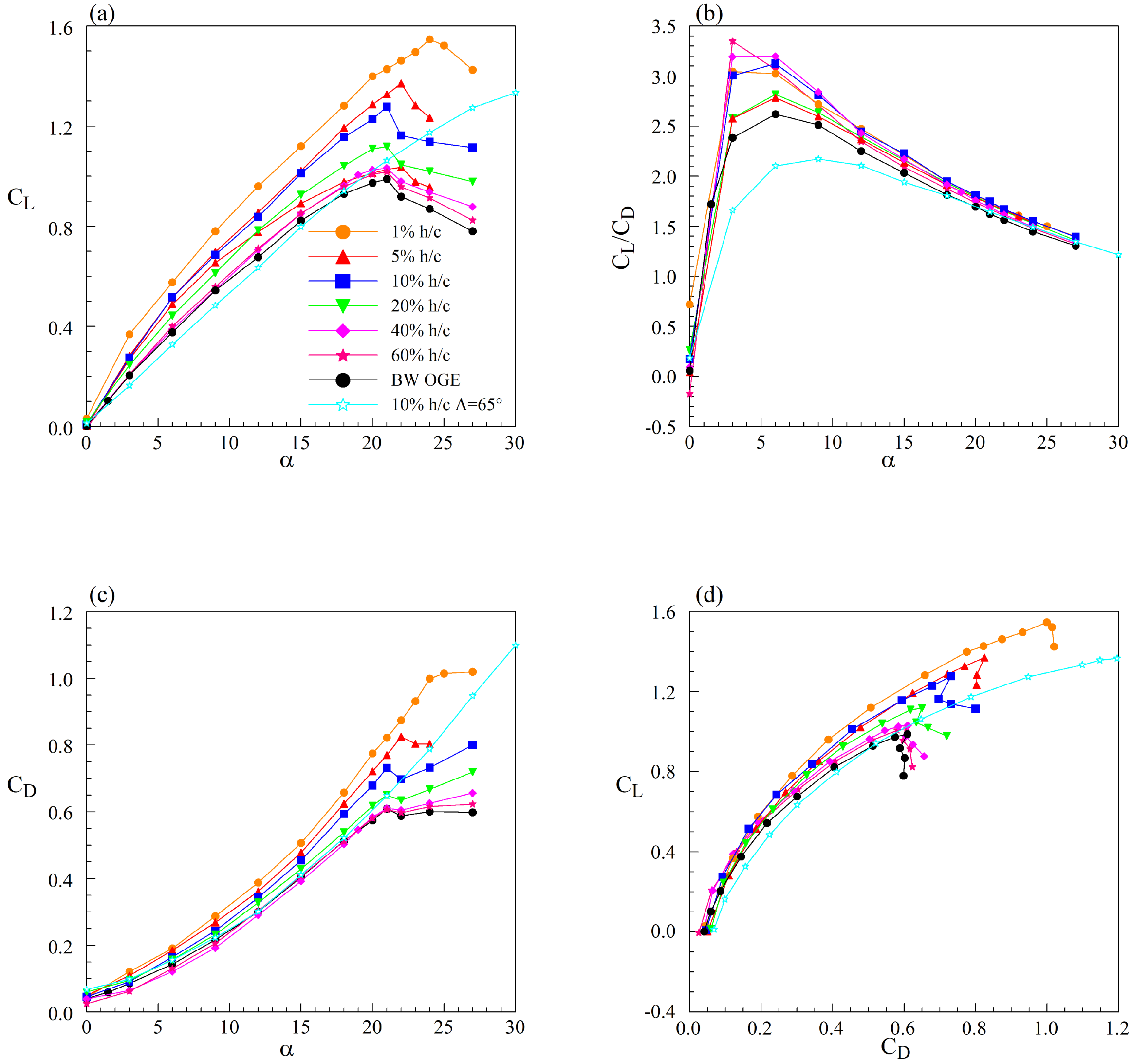

Figure 4.12: Impact of ground proximity on the $\Lambda = 50°$ delta wing. DW50 outside of ground effect (OGE) is denoted as the baseline wing (BW). DW65 at 10% h/c is included for comparison. (a)-(d) Coefficient curves, (e)-(g) increments over BW OGE where $\Delta C_L = (C_{L_{GE}} - C_{L_{OGE}})/C_{L_{OGE}}$ with GE denoting the in ground effect results and ΔC_D and $\Delta C_L/C_D$ following similarly, (h) variation of C_L with ground proximity. The horizontal axes for (e)-(g) begin at $\alpha = 3°$ due to asymptotic behavior resulting from very small baseline values.

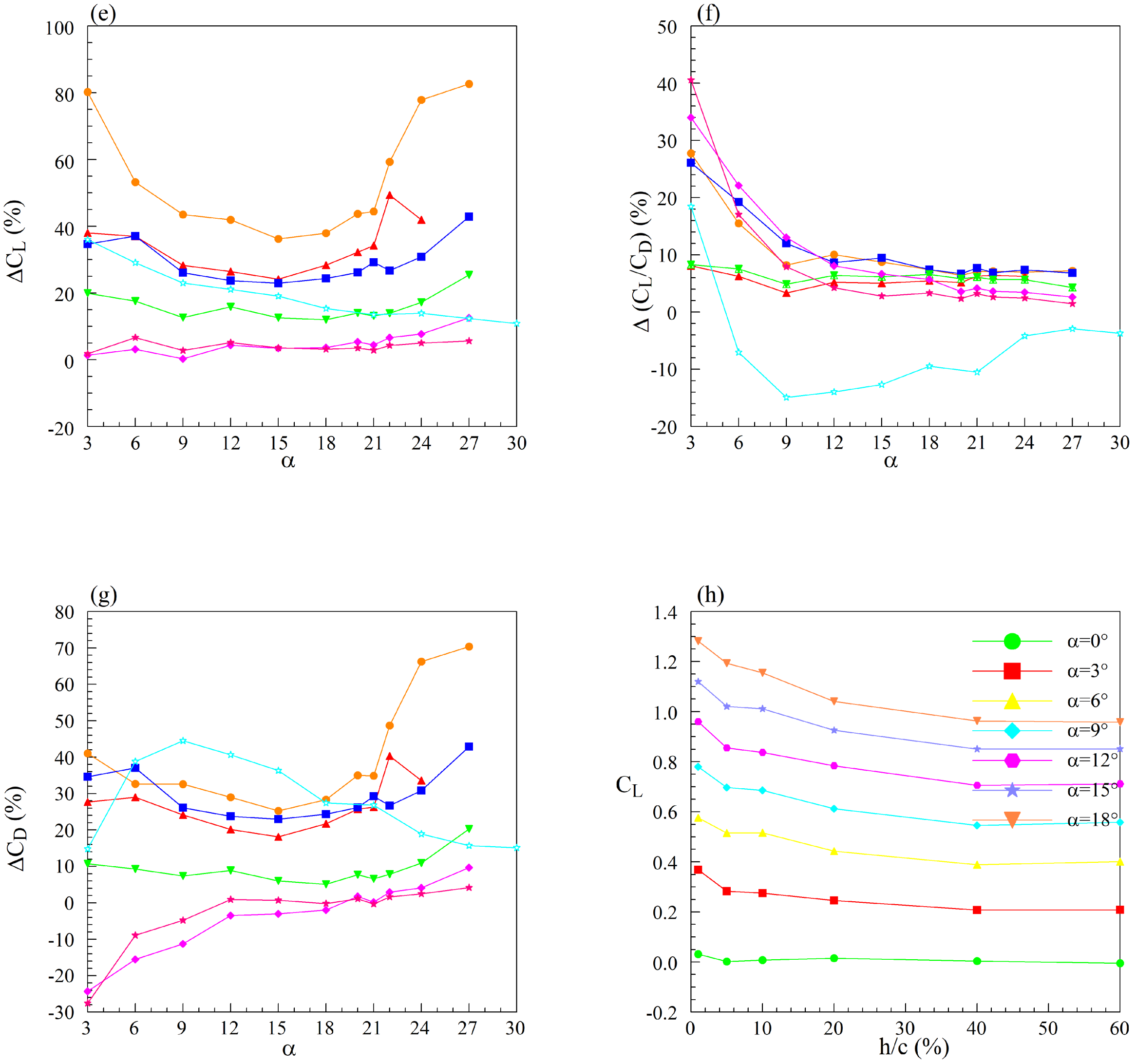

Figure 4.12: Impact of ground proximity on the $\Lambda = 50°$ delta wing. DW50 outside of ground effect (OGE) is denoted as the baseline wing (BW). DW65 at 10% h/c is included for comparison. (a)-(d) Coefficient curves, (e)-(g) increments over BW OGE where $\Delta C_L = (C_{L_{GE}} - C_{L_{OGE}})/C_{L_{OGE}}$ with GE denoting the in ground effect results and ΔC_D and $\Delta C_L/C_D$ following similarly, (h) variation of C_L with ground proximity. The horizontal axes for (e)-(g) begin at $\alpha = 3°$ due to asymptotic behavior resulting from very small baseline values.

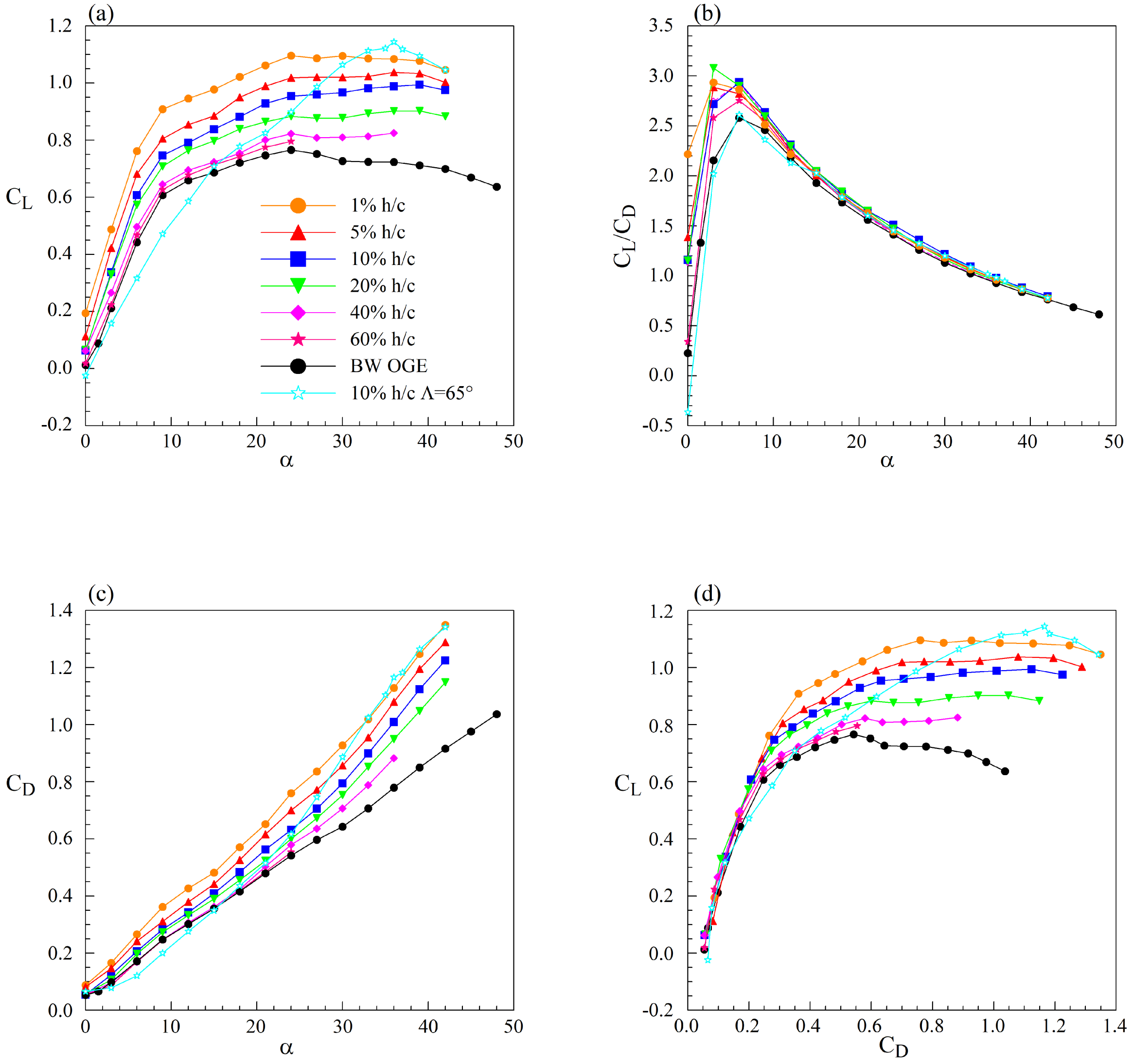

Figure 4.13: Impact of ground proximity on the $\Lambda - 50^\circ$ reverse delta wing. RDW50 outside of ground effect (OGE) is denoted as the baseline wing (BW). RDW65 at 10% h/c is included for comparison. (a)-(d) Coefficient curves, (e)-(h) increments over BW OGE where $\Delta C_L = (C_{L_{GE}} - C_{L_{OGE}})/C_{L_{OGE}}$ with GE denoting the in ground effect results and ΔC_D and $\Delta C_L/C_D$ following similarly, (h) variation of C_L with ground proximity. The horizontal axes for (e)-(f) begin at $\alpha = 3^\circ$ due to asymptotic behavior resulting from very small baseline values.

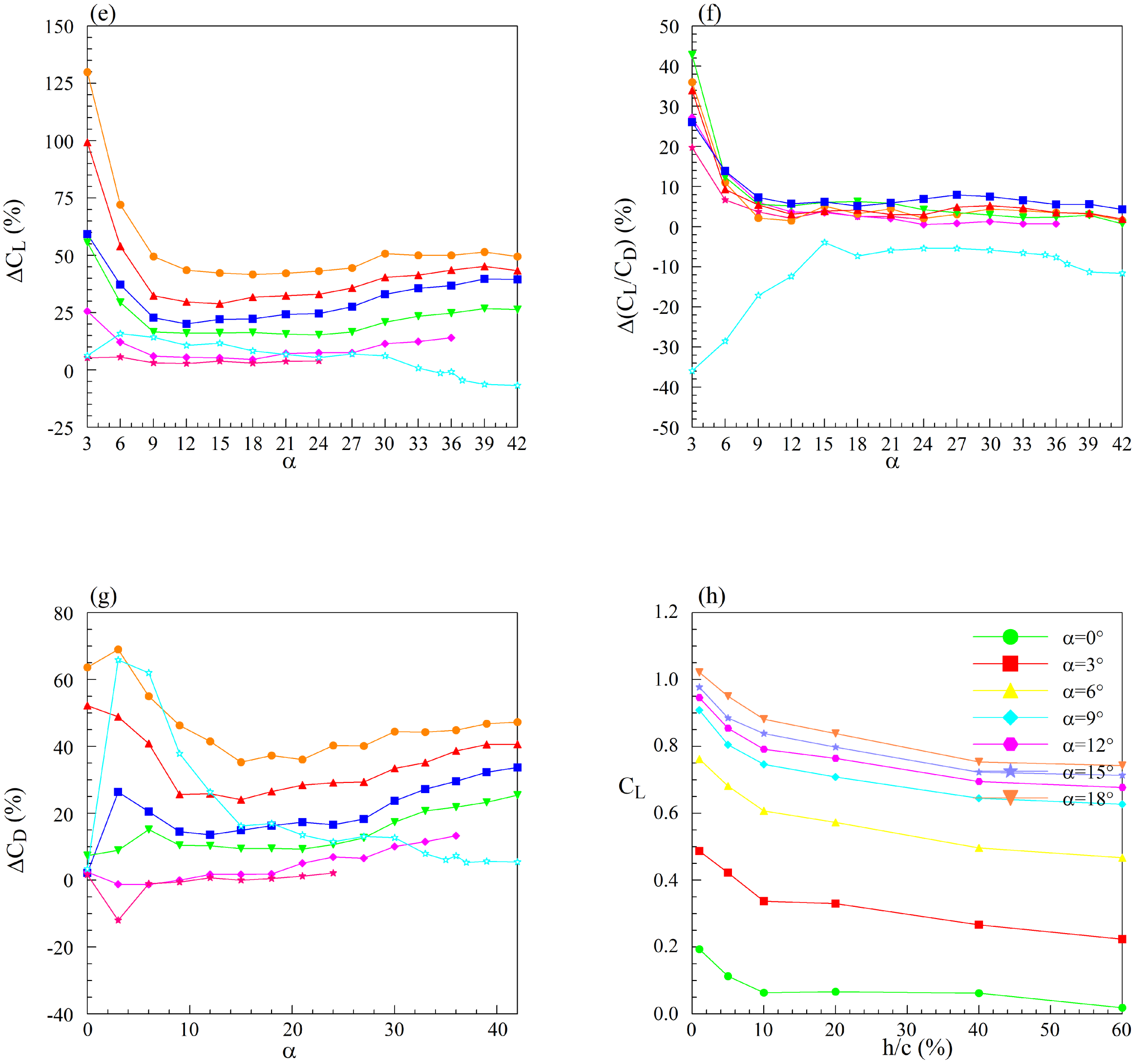

Figure 4.13: Impact of ground proximity on the $\Lambda - 50°$ reverse delta wing. RDW50 outside of ground effect (OGE) is denoted as the baseline wing (BW). RDW65 at 10% h/c is included for comparison. (a)-(d) Coefficient curves, (e)-(h) increments over BW OGE where $\Delta C_L = (C_{L_{GE}} - C_{L_{OGE}})/C_{L_{OGE}}$ with GE denoting the in ground effect results and ΔC_D and $\Delta C_L/C_D$ following similarly, (h) variation of C_L with ground proximity. The horizontal axes for (e)-(f) begin at $\alpha = 3°$ due to asymptotic behavior resulting from very small baseline values.

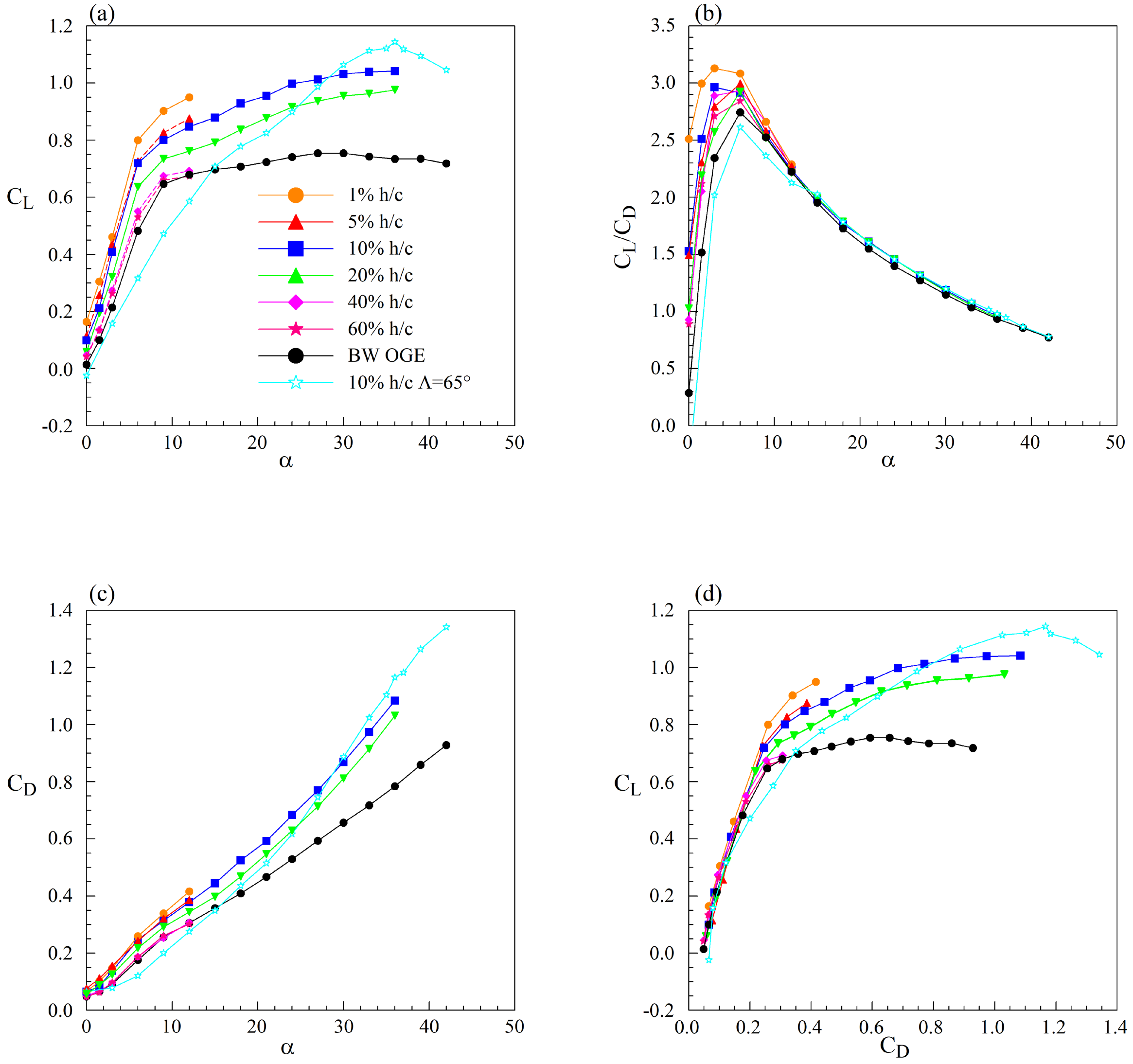

Figure 4.14: Impact of ground proximity on the $\Lambda = 42.5°$ reverse delta wing. RDW42 outside of ground effect (OGE) is denoted as the baseline wing (BW). RDW65 at 10% h/c is included for comparison. (a)-(d) Coefficient curves, (e)-(h) increments over BW OGE where $\Delta C_L = (C_{L_{GE}} - C_{L_{OGE}})/C_{L_{OGE}}$ with GE denoting the in ground effect results and ΔC_D and $\Delta C_L/C_D$ following similarly, (h) variation of C_L with ground proximity. The horizontal axes for (e)-(f) begin at $\alpha = 3°$ due to asymptotic behavior resulting from very small baseline values.

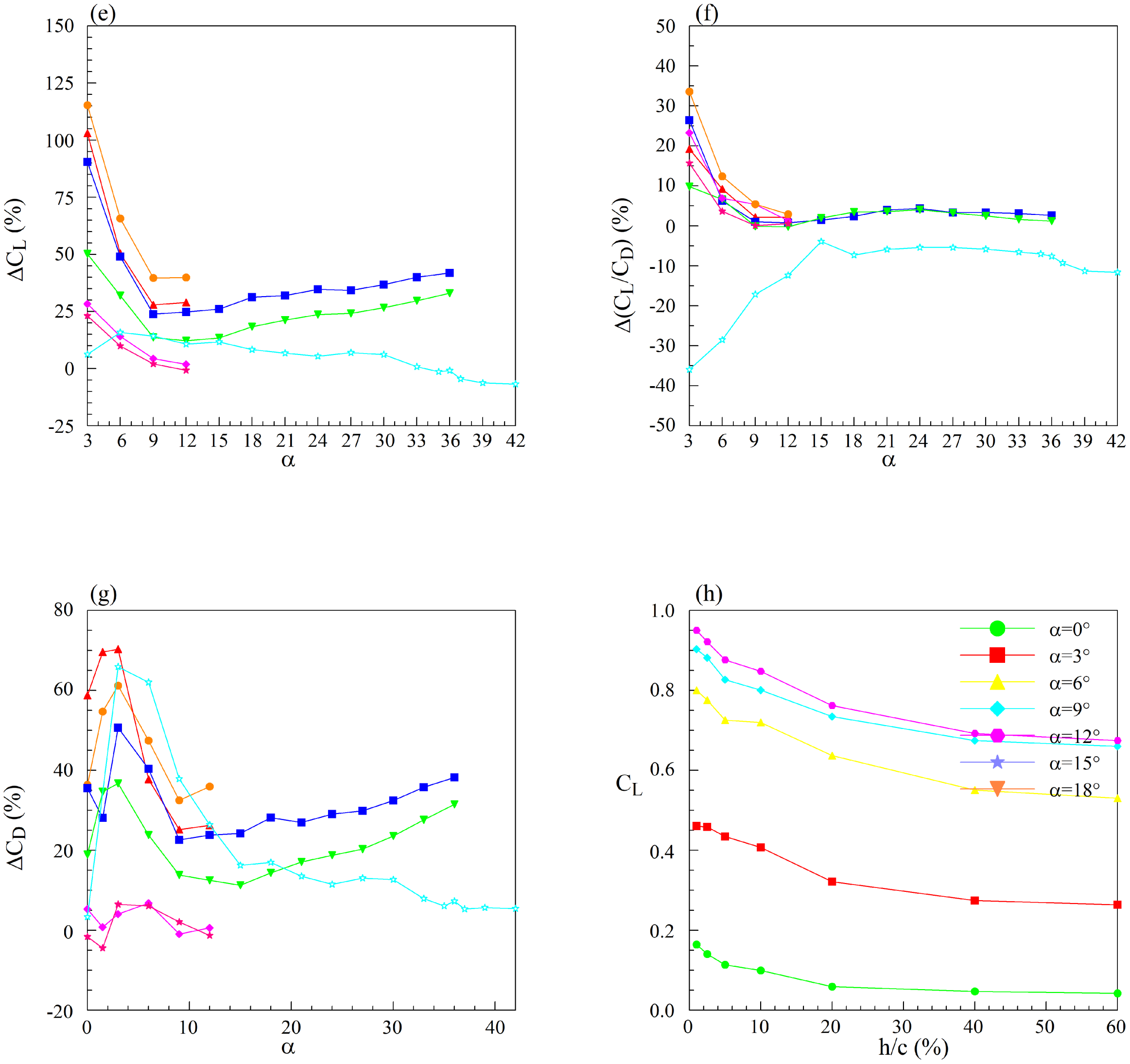

Figure 4.14: Impact of ground proximity on the $\Lambda = 42.5°$ reverse delta wing. RDW42 outside of ground effect (OGE) is denoted as the baseline wing (BW). RDW65 at 10% h/c is included for comparison. (a)-(d) Coefficient curves, (e)-(h) increments over BW OGE where $\Delta C_L = (C_{L_{GE}} - C_{L_{OGE}})/C_{L_{OGE}}$ with GE denoting the in ground effect results and ΔC_D and $\Delta C_L/C_D$ following similarly, (h) variation of C_L with ground proximity. The horizontal axes for (e)-(f) begin at $\alpha = 3°$ due to asymptotic behavior resulting from very small baseline values.

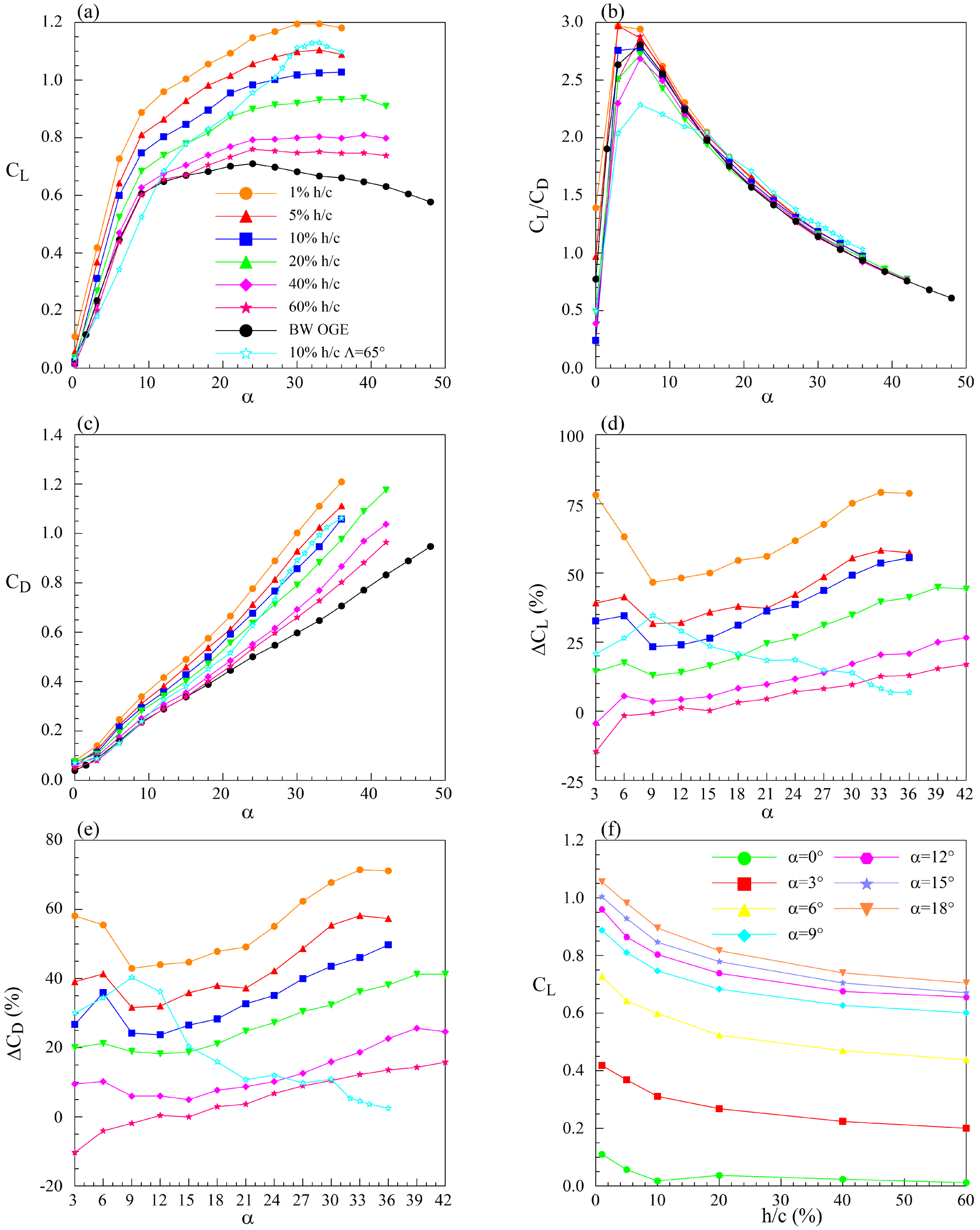

Figure 4.15: Impact of 30% planform cropping on the $\Lambda = 50°$ reverse delta wing in ground effect. The 30% RDW50 outside of ground effect (OGE) is denoted as baseline wing (BW). RDW65 at 10% h/c is included for comparison. (a)-(c) Coefficient curves, (d)-(e) increments over BW OGE where $\Delta C_L = (C_{L_{GE}} - C_{L_{OGE}})/C_{L_{OGE}}$ with GE denoting the in ground effect results and ΔC_D following similarly, (h) variation of C_L with ground proximity. All coefficients are normalized by the surface area of the non-cropped RDW50. The horizontal axes for (d)-(e) begin at $\alpha = 3°$ due to asymptotic behavior resulting from very small baseline values.

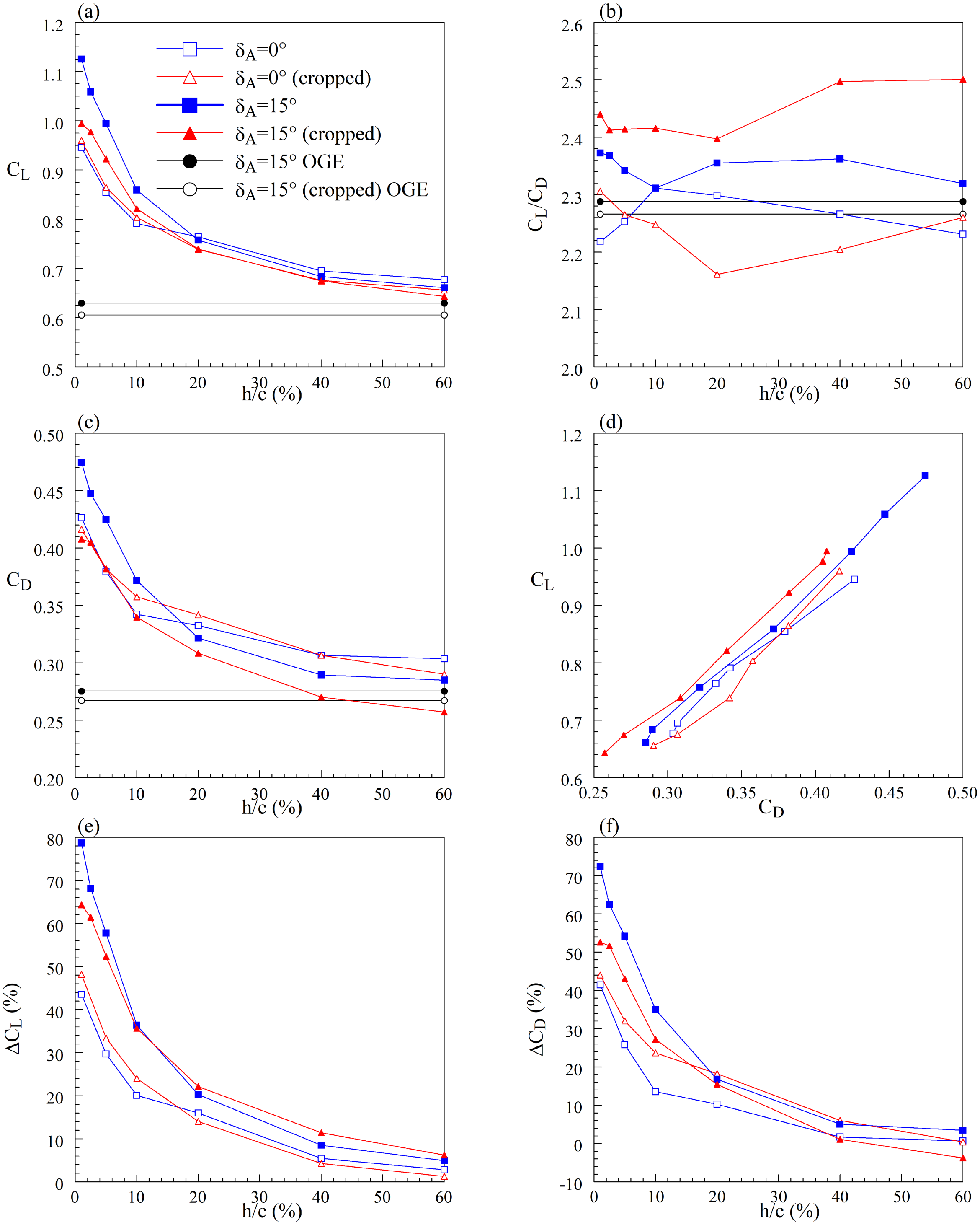

Figure 4.16: Impact of anhedral angle on the $\Lambda = 50°$ reverse delta wing in ground effect, at the angle of attack at which the trailing edge is parallel to the ground: (a)-(d) coefficient curves, (e)-(f) increments over the equivalent outside of ground effect (OGE) configuration where $\Delta C_L = (C_{L_{GE}} - C_{L_{OGE}})/C_{L_{OGE}}$ with GE denoting the in ground effect results and ΔC_D follows similarly. All coefficients are normalized by the surface area of the planar, non-cropped RDW50 wing.

4.3 INSIDE GROUND EFFECT: SES

In this section, the impact of passive control via the use of Gurney flaplike strips on a reverse delta wing in ground effect will be investigated. With increasing anhedral and increasing ground proximity at a low angle of attack, the lift coefficient rapidly increases non-linearly. Large increases are seen below 10% h/c, as can be observed in Figure 4.10 (a), and are described above in Section 4.2. The addition of the Gurney flaplike strips to an anhedraled reverse delta wing in ground effect, with and without planform cropping, are investigated in this section. These strips were added to the trailing edge of the RDW with no planform cropping and to the side-edge of the cropped RDW, in both cases to the anhedraled wing. The side-edge strips, when added to the cropped reverse delta wing, had the rear planform was closed off as discussed in Section 3.3 (see Figure 3.7 (b)). The open configuration refers to the anhedraled and cropped reverse delta wing with no further modifications (or a clean wing configuration), while the closed configuration refers to the same model with this closure of the aft planform on the lower wing surface. SES refers to both trailing edge strips and side-edge strips interchangeably. The force balance measurement results are presented in Figure 4.17-4.20. First, the impact of closing off the rear portion of the wing planform will be discussed (closed versus open configurations), then the results of the RDW equipped with SES will be discussed comparing varying the height of the strip (Figure 4.18 and Figure 4.19) and the anhedral angle (Figure 4.20).

4.3.1 Closed RDW in Ground Effect

When the aft section of the anhedraled wing is blocked off, or closed to create a bluff trailing edge, there is an incremental lift gain (see Figure 4.17 (a)). Because the trailing edge and side-edges are parallel to the ground, the flat plate that closes off the rear portion of the planform (see Figure 3.7 (b)) is suggested to reduce bleed air, resulting in a small increment from the static pressure rise at the aft portion of the lower surface. Not surprisingly, in each anhedral case, the trend and slopes of the lift curve with ground proximity remains very similar between the open and closed cases, albeit at a greater magnitude. However, unlike C_L, C_D increased significantly with the closing of the rear planform over the open wing configuration. This drag increase with increasing ground proximity is likely a primary result of the increased wake extent and separated flow resulting from preventing the high energy flow from entering the wake, while to a lesser extent a result of flow separation at the bottom of the flat plate closing off the rear portion and the increasing static pressure acting on the surface perpendicular to the flow. Due to the large increase in drag relative to lift from the introduction of the closed planform, the lift-to-drag ratio of the closed planform is lower than that of the open configuration, with the increase in lift approximately balanced by the increase in drag (see Figure 4.17 (d)), except for at low ground clearances for the $\delta_A = 8°$ case. A plateau in C_L and C_D can be observed for the $\delta_A = 30°$ cropped reverse delta wing for $h/c \leq 5\%$. This levelling off of lift and drag forces will be discussed further in the next section.

4.3.2 Impact of Varying SES Height in Ground Effect

The results obtained for the non-cropped $\delta_A = 15°$ model in ground effect equipped with side-edge strips are presented in Figure 4.18. The 6% strip height was tested, however is not presented here, as the data is suspect due to extremely low drag. As described above in Section 4.2.3, the C_L for the clean wing configuration for each anhedral angle ($\delta_A = 8°, 15°, 30°$) decreases non-linearly from a peak at $h = 0.01c$, decreasing until $h/c = 0.4$ where the wing reaches approximate freestream. Equipping the $\delta_A = 15°$ reverse delta wing with SES continues this trend, with the increase in magnitude in C_L characteristic of a conventional trailing-edge flap, as described in Section 4.1.5. The addition of the SESs to the RDW led to significant increases in C_L and C_D over the clean wing baseline wing with decreasing h/c and increasing h_{SES}, suggested to be due to the SES entrapping high-pressure fluid in the cavity between the wing and the ground. The lift and drag coefficients increase with increasing h_{SES} and decreasing h/c. The side-edge strips may thus prevent fluid from escaping the high pressure lower surface, enhancing the "air tunnel" like effect observed with the increasing anhedral angle, as observed in Section 4.2.3.

The difference in the lift coefficient between the clean wing and the 2% SES equipped model is greater than that of the difference between 2% and 4%. For example, the incremental lift added in ground effect over the $\delta_A = 15°$ clean wing configuration in the freestream (ΔC_L), presented in Figure 4.18 (e), has a maximum of 352% for the 2% SES, as compared to 371% for the 4% SES equipped model. Diminishing incremental lift returns are expected for further increases in the strip height. At low ground proximities, the lift coefficients for the 0.02c and 0.04c SES strip cases approach each other, although notably, the drag for the 2% and 4% SES cases are approximately equal for all ground proximities (Figure 4.18 (c)). The increased drag with increased lift for the SES equipped model in ground effect is similarly linear in nature (Figure 4.18 (d)) to the anhedraled models in ground effect (see Section 4.2.3). This results in marginal change in the lift-to-drag ratio in ground effect for the SES equipped $\delta_A = 15°$ model (Figure 4.18 (b) and (f)).

The results of equipping side-edge strips of varying height (2%-6% of root chord) on a $\delta_A = 15°$ 30% cropped reverse delta wing in ground effect are presented in Figure 4.19. All cropped wings equipped with side-edge strips had their rear planforms blocked off, or were tested in the "closed" configuration as described above in Section 4.3.1 (see Figure 3.7 (b)). The trend of increased C_L and C_D with increasing h_{SES} and decreasing h/c follow their non-cropped counterparts (Figure 4.18 (a)-(b)), however, a plateau and force reduction is observed for $h/c \leq 5\%$ for the SES equipped, cropped models. Despite this minor force reduction at low ground clearances, a significant lift augmentation is observed, for example 267%, 301% and 340% over the clean wing freestream configuration, for the 2%, 4%, and 6% case respectively, at $h/c = 0.05$. The application of this relatively simple mechanical device to the trailing- and side-edges of the reverse delta wing is effective in augmenting lift at all ground clearances for the angle of attack under consideration. This benefit has a corresponding drag penalty, which is particularly evident for the large increase in C_D observed for the 6% SES (Figure 4.19 (c)). The greater the strip height is outside of the boundary layer, the more that the strip is exposed to freestream flow conditions, which is thus likely to significantly increase drag from both pressure drag on the side-edge strip, and by an increase in the wake size. This is why Gurney flaps are typically of the order of the local boundary layer thickness. Thus, the 6% SES has a greatly increased drag coefficient and drag increment, and this may partly explain why the 2% and 4% cases are close for the cropped and non-cropped model. The lift and drag increments (and coefficients) observed for the 30% cropped model are of the same order as the non-cropped model. Introducing aft planform cropping may then be seen as a means to improve the lifting capabilities of the reverse delta wing when operating in ground effect when equipped with side-edge strips to augment lift generation. The cropped reverse delta wing has a lower ground proximity due to its reduced root chord, suggesting an increase in the RAM pressure on the windward surface and thus overcoming the reduction in lift from a reduced planform surface area on which the static pressure rise may act.

In the same manner as the anhedraled wing increments (i.e. without SES equipped), the lift and drag increments for the SES equipped $\delta_A = 15°$ 30% cropped model increase non-linearly with reducing h/c with a large increase for $h/c < 20\%$ (Figure 4.19 (e)-(f)). The peak increments are reached at $h/c = 5\%$ due to the aforementioned force reduction for $h/c < 5\%$. The increased lift from the 6% strip height is overwhelmed by the greatly increased drag coefficient, resulting in a significantly reduced lift-to-drag ratio relative to the clean wing for $h/c \leq 40\%$ (Figure 4.19 (b)). This indicates a balance with increasing strip height between the increased drag, from extending outside of the local boundary layer thickness and increased separated flow, and increased lift, from entrapping greater volumes of high-pressure fluid in the cavity between the wing and the ground. The 4% SES height is advantageous then in that a large lift increment is observed with a negligible increase in drag over the 2% configuration, resulting in the greatest overall lift-to-drag ratio (see Figure 4.19 (b)), when compared against the other tested $\delta_A = 15°$ cropped models in ground effect.

A force reduction at extreme ground proximities was first described in Section 4.2.2 for the cropped reverse delta wing inside ground effect. The equipping of the cropped RDW with anhedral with SESs exacerbates this force reduction below $h/c = 5$, with the force reduction occurring at higher ground clearances with larger δ_A, possibly due to the anhedral placing the wing tips and trailing edge further in ground effect while the upper surface is removed from it. This force reduction may be the result of the wing and ground boundary-layers merging, or experimental error introduced by the slot in the ground (see Figure 3.3 (a)). It may also be a result of significantly separated flow over the upper surface of the wing resulting from a strongly adverse pressure gradient at low ground proximities due to the anhedral, cropping, and the equipment of the side-edge strips.

4.3.3 Impact of Varying Anhedral on SES equipped RDW in Ground Effect

In this final section, the impact of varying anhedral angle on a cropped reverse delta wing with anhedral equipped with SES is discussed. Force balance measurement results on reverse delta wings with $\delta_A = 8°, 15°, 30°$ with $h_{SES} = 2\%, 4\%$ are presented in Figure 4.20. In general, with the addition of the SES for all anhedral angles, the lift increases non-linearly with decreasing ground clearance and with increasing SES height. As hypothesized priorly, increasing the anhedral angle increasingly traps the air under the wing in the open cavity between the windward surface and the ground, an effect further enhanced by equipping side-edge strips. The highest lift coefficient is observed for the $\delta_A = 30°$ with $h_{SES} = 4\%$, while the greatest lift increment over the freestream clean wing is seen for the $\delta_A = 8°$ model (Figure 4.20 (e)). Maximum lift increments of 504% and 305%, for example, are observed for the $\delta_A = 8°$ and $\delta_A = 15°$ wings with 4% side-edge strips, respectively. Increasing the anhedral and, as described prior, increasing the height of the side-edge strip in close ground proximity results in significant drag increases (Figure 4.20 (c)). The probable increase in separated flow, wake size and extent, and increased profile drag thus result in little change with increasing ground proximity in the lift-to-drag ratio for the cropped, anhedraled, reverse delta wings with side-edge strips (Figure 4.20 (b)). The highest C_L/C_D is seen for $\delta_A = 8°$ with $h_{SES} = 2\%$, and $\delta_A = 15°$ with $h_{SES} = 4\%$. Notably, in extreme ground effect, these configurations have a reduced effectiveness, i.e. the aforedescribed force reduction, resulting in maximum C_L and C_D at ground proximities of approximately $h/c = 2.5\% - 5\%$.

In summary, the optimum configuration in this study is the 4% side-edge strip equipped reverse delta wing, with $\delta_A = 15°$ and 30% cropping, as significant lift augmentation is found with the employment of the side-edge strips, with marginal change in the lift-to-drag ratio with decreasing ground clearance, and the greatest overall lift-to-drag ratio for the SES equipped models.

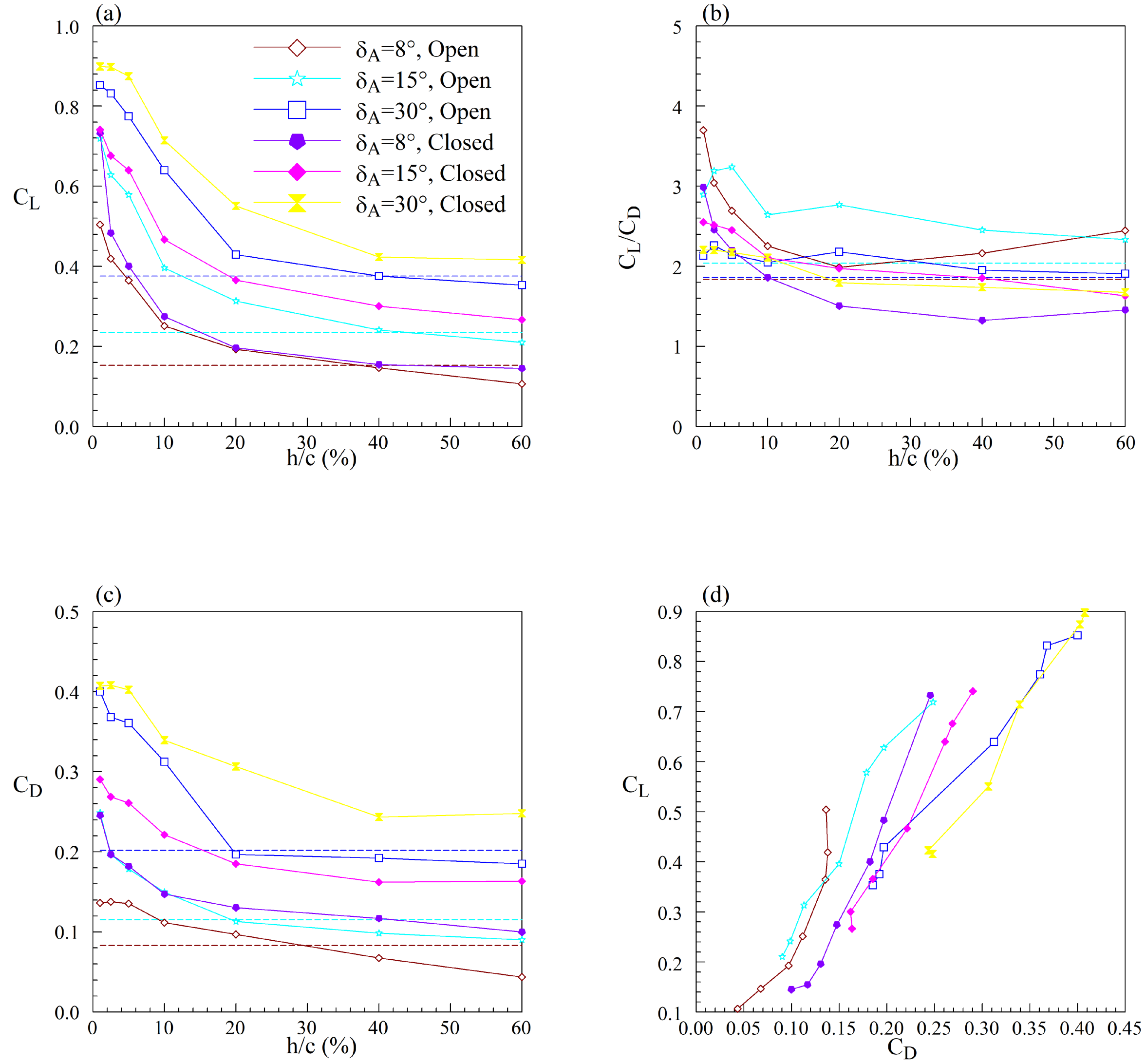

Figure 4.17: Impact on aerodynamic coefficients of closing off of the lower surface of the 30% cropped slender reverse delta wing with anhedral in ground effect, at the angle of attack at which the trailing edge is parallel to the ground. Dashed lines indicate out of ground effect quantities. All coefficients are normalized by the surface area of the non-cropped, planar RDW65.

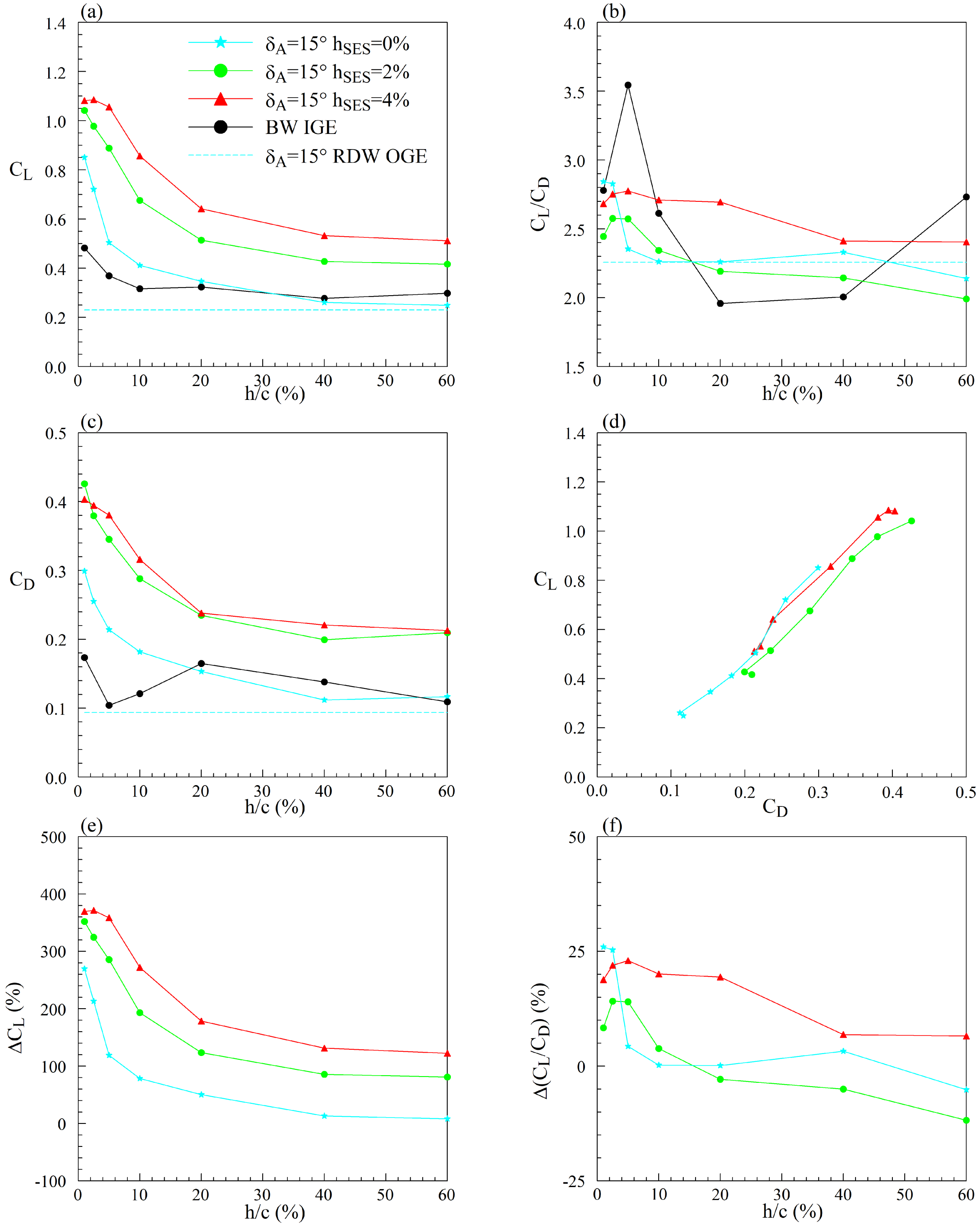

Figure 4.18: Impact of varying SES height on the $\delta_A = 15°$ slender reverse delta wing in ground effect, at the angle of attack at which the trailing edge is parallel to the ground. The planar RDW65 is denoted as the baseline wing BW. (a)-(d) Coefficient curves, (e)-(f) increments over OGE values. Here $\Delta C_L = (C_{LIGE} - C_{LOGE})/C_{LOGE}$. The increment in C_L/C_D follows similarly. The dashed line indicates freestream values. All coefficients are normalized by the surface area of the BW.

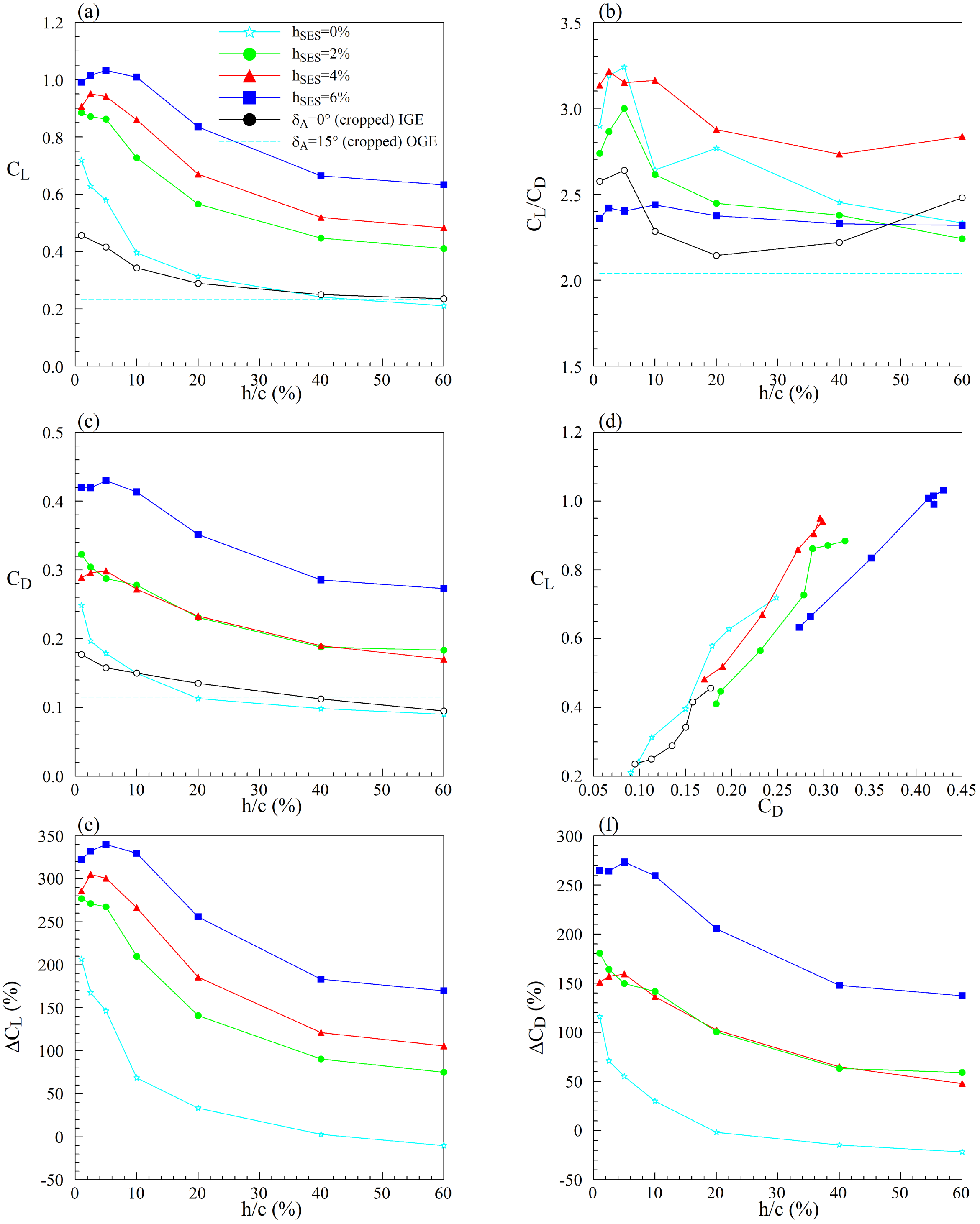

Figure 4.19: Impact of SES height on the 30% cropped, $\delta_A = 15°$ slender reverse delta wing in ground effect, at the angle of attack at which the trailing edge is parallel to the ground. OGE denotes freestream results. (a)-(d) Coefficient curves, (e)-(f) increments over OGE values. Here $\Delta C_L = (C_{LIGE} - C_{LOGE})/C_{LOGE}$. The increment in C_D follows similarly. The dashed line indicates the freestream values. All coefficients are normalized by the surface area of the planar, non-cropped RDW65.

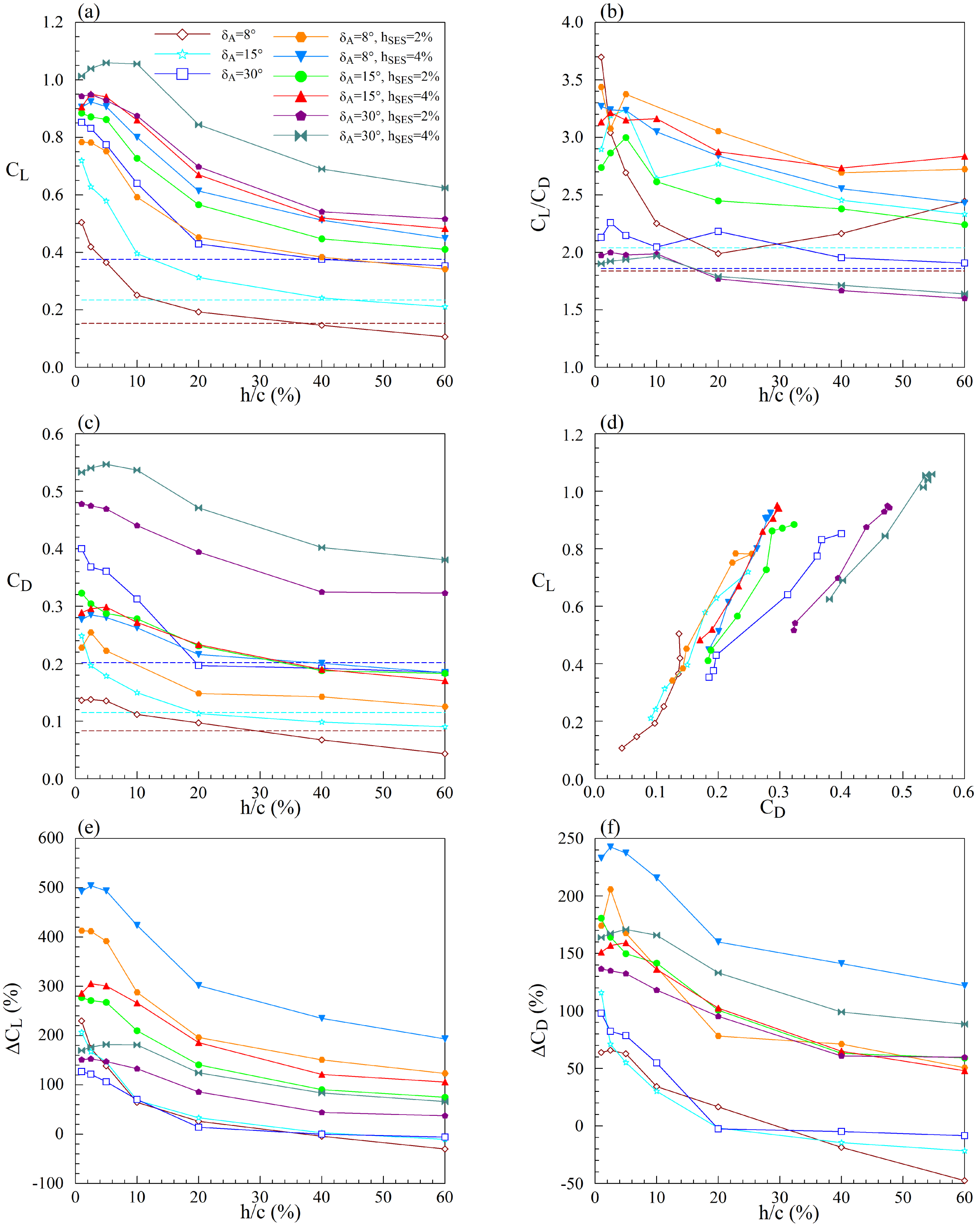

Figure 4.20: Impact of anhedral angle on the slender, 30% cropped reverse delta wing in ground effect equipped with SES, at the angle of attack at which the trailing edge is parallel to the ground. Dashed lines denote freestream results. (a)-(d) Coefficient curves, (e)-(f) increments over OGE values. Here $\Delta C_L = (C_{LIGE} - C_{LOGE})/C_{LOGE}$. The increment in C_D follows similarly. All coefficients are normalized by the surface area of the planar, non-cropped RDW65.

CHAPTER 5

CONCLUSION

A reverse delta wing was experimentally investigated in ground effect using two-component force balance measurements, alongside the impact of anhedral and rear planform cropping, and non-slenderness. Baseline results were established in freestream conditions for comparison. Gurney flaplike strips were then employed as passive control for lift augmentation.

5.1 FREESTREAM CONCLUSIONS

The reverse delta wing was found to have reduced lift generation compared to its regular counterpart for $\alpha > 14°$, resulting from the absence of vortex (non-linear) lift over the reverse delta wing. Outside of the attached potential flow regime, the primary lift generation for the reverse delta wing is from the static pressure rise on the windward surface. Drag production for the delta wing is greater however, from increased induced and pressure drag, resulting in a comparable lift-to-drag ratio for the two slender wings. The reverse delta wing exhibits a delayed stall yet reduced maximum lift coefficient. Moderate aft planform cropping ($\leq 30\%$ of root chord) of the reverse delta wing led to only a small reduction in the lift generation at most angles of attack. The increased drag production relative to the baseline reverse delta wing for the cropped reverse delta wing is suggested to be a result of increased three dimensional backflow enhancing disruption of the spanwise vortex filaments on the upper surface, this disruption resulting in pre-mature stall relative to the baseline wing. At typical flight conditions, there is a benign aerodynamic impact, thus indicating that significant weight reductions and increased lifting capacity may be achieved with the implementation of planform cropping. Incorporating anhedral resulted in decreased lift and drag forces with increasing anhedral, along with reduced maximum lift. Decreased lift production decreased is suggested to result from a reduced projected area, while the lowered C_D may be a result of a modified separated flow behavior and the reduced profile. The introduction of anhedral and cropping in the freestream resulted in a reduced lift-to-drag ratio relative to the baseline case.

In contrast to the slender model, an increase in the lift-curve slope resulted from the decreased sweep angle (increase in aspect ratio) and the non-slender reverse delta wing lift coefficient was found to level off beyond $\alpha = 9°$, likely as a result of large-scale flow separation on the leeward surface. The drag coefficient increased monotonically with increasing incidence. The lift of the non-slender models gradually increased to their respective maximum lift coefficients, at a significantly reduced C_{Lmax} and α_{SS}, before tapering off. Rear planform cropping followed the trend of the slender case except for α_{SS} which was found insensitive to the 30% cropping. Alternatively, the tested anhedral angle of 15-degrees on the non-slender reverse delta wing was found negligible on lift production in the separated flow regime.

Equipping Gurney flaplike strips of constant heights (2%-6% of root chord) to the side- and trailing-edges of the reverse delta wing resulted in a leftward and upward shift of the lift-curve (induced camber effect), in a manner characteristic of the deployment of conventional trailing edge flaps. The lift increase is primarily a result of the entrainment of high pressure flow beneath the wing, increasing the static pressure on the windward surface and alleviating cross-flow leakage. Greater strip heights resulted in increased C_L, however a stronger adverse pressure gradient promoted the separated flow over the leeward surface (increasing drag production), reducing the stall angle of the wing. The application of the side-edge strips was effective in augmenting lift generation, with the enhancement greatest at low angles of attack.

5.2 IMPACT OF GROUND EFFECT ON THE REVERSE DELTA WING

With reducing ground clearance, the lift generated by the reverse delta wing and delta wing in ground effect was found to increase non-linearly, with freestream conditions reached at a ground clearance of 40% of the root chord for the reverse delta wing, and 60% for the delta wing. The lift-curve slope was found to increase with ground proximity. Stalling was promoted for the reverse delta wing in ground effect. Rear planform cropping allowed the reverse delta wing closer ground proximity due to reduced chord length, increasing both lift and drag forces, with a net increase in the lift-to-drag ratio for the $h/c = 0.1$ case. The planar reverse delta wings, for a fixed angle of attack, were observed to have a non-linear increase in lift and drag coefficients, with a gradual increase in force from $h/c = 0.6$ to $h/c = 0.1$, and a significant non-linear increase to a maximum at the lowest achievable ground clearance. This increased lift is suggested to result from the ground effect induced static pressure rise on the windward surface, while the drag increase with decreasing ground clearance may be a result of the pressure rise and the greater extent of separated flow caused by the increasingly adverse pressure gradient. The increase in lift from ground effect was found to be greatest in the low-α regime, at low ground clearances. This effect was thus enhanced by the introduction of anhedral, at an effective angle of attack at which the trailing edge is parallel to the ground, creating an “air tunnel” effect. High pressure flow is hypothesized to be trapped in the cavity beneath the wing’s lower surface and the ground, increasing the impact of ground effect on the reverse delta wing. An increasing anhedral angle in ground effect led to a non-linear increase of C_L with increasing ground proximity, though this was coupled with an increase in the drag coefficient, with a linear relationship between C_L and C_D for a fixed α and varying h/c. Thus, while the largest lift augmentation is observed at extreme ground proximity, the maximum increase in lift-to-drag ratio was observed at $h = 0.1c - 0.2c$, with lift-to-drag ratios collapsing in the moderate- to high-α regime. The 15-degree anhedraled wings were found to have the greatest improvement in their lift-to-drag ratios in ground effect.

Similar trends to the slender wing were observed for the non-slender models, with lift and drag forces increasing with increasing ground proximity, increasing the lift-curve slope with decreasing sweep angle and increasing ground proximity. A non-zero lift was found at the zero incidence angle for the non-slender reverse delta wing in ground effect, while a negligible change in the minimum drag force was observed. The non-zero lift for the non-slender reverse delta wing significantly outweighed that of the non-slender delta wing. Further study is needed to elucidate the mechanisms behind this flow phenomenon. Increasing the relative percentage of planform area at the fore of the wing surface of the reverse delta wing, such as that achieved through a reduction of sweep angle and thus increase in aspect ratio, was found to be advantageous at low angles of attack in ground effect, as the increased fore surface area allows for greater impact of the RAM pressure rise from close ground proximity.

5.3 CONCLUSIONS ON PASSIVE CONTROL IN GROUND EFFECT

To further augment lift in ground effect, side-edge strips were subsequently employed on the slender, anhedraled, reverse delta wings, with a suggested large entrainment of high pressure fluid in the cavity between the wing and the ground, and an increase in the “air tunnel” effect observed for the anhedraled models. Increasing strip height and decreasing ground clearance resulted in increased lift and drag coefficients, with maximum aerodynamic forces observed at 5% ground clearance. The linear relation between lift and drag increments resulted in marginal improvement in lift-to-drag ratios, except at extremely low ground clearances. The greatest lift increment is observed for the application of the 4% side-edge strips to the 8-degree anhedral wing, while the largest lift coefficient was observed for the 30-degree anhedral wing. Thus, in summary, the addition of Gurney flaplike strips, along with anhedral, to a cropped reverse delta wing can increase lift, while achieving a weight reduction from cropping, when operating in close ground proximity. Moderate anhedral and strip height leads to similar C_L/C_D ratios compared to the baseline wing. The optimum configuration however was determined as the 30% cropped model, with 15° anhedral, equipped with 4% side-edge strips operating at typical ground clearances of 10%-20% of root chord.

CHAPTER 6

FUTURE WORK

This study was primarily concerned with determining the aerodynamic characteristics of reverse delta wings in ground effect, with Gurney flaplike strips employed at the trailing edge. However, there remains a need for significant research into reverse delta wings in ground effect, particularly in wholefield axial flow measurements, to obtain the vortical flow field, circulation over the wing surface, and wake measurements. Additional research may consider the addition of pressure taps to the reverse delta wing to determine the pressure distribution on the reverse delta wing surfaces, particularly to determine the modified load distribution introduced by the employment of the Gurney flaplike strips and to validate the pitching moment and stability in ground effect.

Additional modifications to the Gurney flaplike strips may also be investigated, including the reduction of wake size and potential flow instabilities through the introduction of slits, serration, holes, or vortex generators in the Gurney flaplike strips, which may reduce lift through bleed air, but may improve overall L/D from drag reduction. This may allow greater flap heights to be employed while limiting the drag increase that results.

Planform modifications may be investigated as a means to further optimize the reverse delta wing planform in ground effect, such as the implementation of a flat top reverse delta wing with only anhedral tips, which still causes an increase in RAM pressure in the cavity between the wing lower surface and the ground, however the projected area remains higher than a fully anhedraled reverse delta wing. This is expected to further enhance the lift in ground effect, and warrants further investigation. Early experiments into the aerodynamics of the flat top and anhedraled-tipped reverse delta wing have demonstrated promising results for improved lift generation and aerodynamic efficiency in ground effect.

Finally, dynamic motion remains an elusory area of investigation for reverse delta wings in and out of ground effect. The investigation of a plunging motion or a pitching oscillation of reverse delta wings is needed for a more complete understanding of the flow physics of a reverse delta wing and Lippisch-type WIG craft.

REFERENCES

Ahmed, M., and S. Sharma. 2005. “An investigation on the aerodynamics of a symmetrical airfoil in ground effect.” *Experimental Thermal and Fluid Science* 29, no. 6 (July): 633–647. doi:`10.1016/j.expthermflusci.2004.09.001`.

Ahmed, M., T. Takasaki, and Y. Kohama. 2007. “Aerodynamics of a NACA 4412 airfoil in ground effect.” *AIAA Journal* 45, no. 1 (January): 37–47. doi:`10.2514/1.23872`.

Altaf, A., A. A. Omar, W. Asrar, and H. B. L. Jamaluddin. 2011. “Study of the reverse delta wing.” *Journal of Aircraft* 48, no. 1 (January): 277–286. doi:`10.2514/1.c031101`.

Altaf, A., T. B. Thong, A. A. Omar, and W. Asrar. 2016. “Influence of a reverse delta-type add-on device on wake vortex alleviation.” *AIAA Journal* 54, no. 2 (February): 625–636. doi:`10.2514/1.j054436`.

Baker, P. A., W. G. Schweikhard, and W. R. Young. 1970. *Flight evaluation of ground effect on several low-aspect-ratio airplanes.* NASA Technical Note TN D-6053. Flight Research Center, NASA.

Buchholz, M. D., and J. Tso. 2000. “Lift augmentation on delta wing with leading-edge fences and Gurney flap.” *Journal of Aircraft* 37, no. 6 (November): 1050–1057. doi:`10.2514/2.2710`.

Chen, Y., and W. G. Schweikhard. 1985. “Dynamic ground effects on a two-dimensional flat plate.” *Journal of Aircraft* 22, no. 7 (July): 638–640. doi:`10.2514/3.45179`.

Cho, J., C. Han, Y. Moon, and J. Baek. 2001. “Aerodynamic analysis and design of an aerolevitation electric vehicle.” In *19th AIAA Applied Aerodynamics Conference.* American Institute of Aeronautics / Astronautics, June. doi:`10.2514/6.2001-2435`.

Curry, R. E., and L. R. Ownes. 2003. *Ground-effect characteristics of the Tu-144 supersonic transport airplane.* NASA TM-2003-212035. NASA.

Delery, J. M. 1994. “Aspects of vortex breakdown.” *Progress in Aerospace Sciences* 30, no. 1 (January): 1–59. doi:`10.1016/0376-0421(94)90002-7`.

Dogar, M. 2012. "An investigation of aerodynamics and flow characteristics of slender and non-slender delta wings." Master's thesis, McGill University.

Flax, A. H. 1949. "Relations between the characteristics of a wing and its reverse in supersonic flow." *Journal of the Aeronautical Sciences* 16, no. 8 (August): 496–504. doi:`10.2514/8.11839`.

Gerhardt, H. A. (N. G. Corporation). 1996. Supersonic natural laminar flow wing. U.S Patent 5,538,201, filed July 23, 1996.

Gibson, B. T., and H. A. Gerhardt. 1995. "Natural laminar flow wing concept for supersonic transports." *Journal of Aircraft* 32, no. 1 (January): 130–136. doi:`10.2514/3.46693`.

Giguère, P., G. Dumas, and J. Lemay. 1997. "Gurney flap scaling for optimum lift-to-drag ratio." *AIAA Journal* 35, no. 12 (December): 1888–1890. doi:`10.2514/2.49`.

Greenwell, D. I. 2010. "Gurney flaps on slender and nonslender delta wings." *Journal of Aircraft* 47, no. 2 (March): 675–681. doi:`10.2514/1.46610`.

Gursul, I., R. Gordnier, and M. Visbal. 2005. "Unsteady aerodynamics of nonslender delta wings." *Progress in Aerospace Sciences* 41, no. 7 (October): 515–557. doi:`10.1016/j.paerosci.2005.09.002`.

Gursul, I., Z. Wang, and E. Vardaki. 2007. "Review of flow control mechanisms of leading-edge vortices." *Progress in Aerospace Sciences* 43, nos. 7-8 (October): 246–270. doi:`10.1016/j.paerosci.2007.08.001`.

Halloran, M., and S. O'Meara. 1999. *Wing in ground effect craft review: DSTO-GD-0201.* DSTO-GD-0201. Australia: Australia Aeronautical and Maritime Research Laboratory.

Han, C., J. Cho, Y. Moon, Y. Yoon, and Y. Song. 2005. "Design of an aerolevitation electric vehicle for high-speed ground transportation system." *Journal of Aircraft* 42, no. 1 (January): 93–104. doi:`10.2514/1.95`.

Irodov, R. D. 1974. "Criteria of longitudinal stability of ekranoplan." Moscow, USSR [in English], translated Russian by R. D. Hill. *Ucheniye Zapiski TSAGI* 1, no. 4 (November): 63–72.

Jamei, S., A. Maimun, S. Mansor, N. Azwadi, and A. Priyanto. 2012. "Numerical investigation on aerodynamic characteristics of a compound wing-in-ground effect." *Journal of Aircraft* 49, no. 5 (September): 1297–1305. doi:`10.2514/1.c031627`.

Jamei, S., A. M. A. Malek, S. Mansor, N. A. C. Sidik, and A. Priyanto. 2014. "Experimental aerodynamic characteristics of a compound wing in ground effect." *Journal of Fluids Engineering* 136, no. 5 (March): 051206. doi:`10.1115/1.4026618`.

Jeffrey, D., X. Zhang, and D. W. Hurst. 2000. "Aerodynamics of Gurney flaps on a single-element high-lift wing." *Journal of Aircraft* 37, no. 2 (March): 295–301. doi:`10.2514/2.2593`.

Jobe, C. E. 2004. "Vortex breakdown location over 65 degrees delta wings empiricism and experiment." *The Aeronautical Journal* 108, no. 1087 (September): 475–482. doi:`10.1017/s0001924000000294`.

Jung, K. H., H. H. Chun, and H. J. Kim. 2008. "Experimental investigation of wing-in-ground effect with a NACA 6409 section." *Journal of Marine Science and Technology* 13, no. 4 (September): 317–327. doi:`10.1007/s00773-008-0015-4`.

Katz, J., and D. Levin. 1984. "Measurements of ground effect for delta wings." *Journal of Aircraft* 21, no. 6 (June): 441–443. doi:`10.2514/3.44988`.

Ko, L. 2017. "An experimental investigation of the aerodynamics and vortex flowfield of a Reverse delta wing." PhD diss., McGill University.

Kocivar, B., ed. 1977. *Ram-wing X-114: floats, skims, and flies* (December 1): 70–73.

Kohlman, D. L., and J. W. H. Wentz. 1971. "Vortex breakdown on slender sharp-edged wings." *Journal of Aircraft* 8, no. 3 (March): 156–161. doi:`10.2514/3.44247`.

Lambourne, N. C., and D. W. Bryer. 1961. *The bursting of leading-edge vortices - some observations and discussion of the phenomenon: RM 3282.* Reports and Memoranda. Aeronautical Research council, April 1.

Lee, H. J., B. J. Kang, J. H. Park, C. M. Lee, K. J. Kang, and C. G. Kang. 2012. "Development of hoverwing type WIG craft WSH-500." In *2012 Oceans - Yeosu.* IEEE, May 21. doi:`10.1109/oceans-yeosu.2012.6263589`.

Lee, J., C.-S. Han, and C.-H. Bae. 2010. "Influence of wing configurations on aerodynamic characteristics of wings in ground effect." *Journal of Aircraft* 47, no. 3 (May): 1030–1040. doi:`10.2514/1.46703`.

Lee, M., and C.-M. Ho. 1990. "Lift force of delta wings." *Applied Mechanics Reviews* 43, no. 9 (September): 209. doi:`10.1115/1.3119169`.

Lee, P.-H., C. E. Lan, and V. U. Muirhead. 1987. *An experimental investigation of dynamic ground effect.* NASA Contractor Report 4105. Flight Research Laboratory, The University of Kansas Center for Research, Inc.

———. 1989. "Experimental investigation of dynamic ground effect." *Journal of Aircraft* 26, no. 6 (June): 497–498. doi:`10.2514/3.45793`.

Lee, T. 2016. "Impact of Gurney flaplike strips on the aerodynamic and vortex flow characteristic of a reverse delta wing." *Journal of Fluids Engineering* 138, no. 6 (February): 061104. doi:`10.1115/1.4032301`.

Lee, T., and S. Choi. 2015. "Wingtip vortex control via tip-mounted half-delta wings of different geometric configurations." *Journal of Fluids Engineering* 137, no. 12 (August): 121105. doi:`10.1115/1.4030852`.

Lee, T., and J. Pereira. 2013. "Passive control of unsteady-wing tip vortex via a slender half-delta wing in both reverse and regular configurations." *Experiments in Fluids* 54, no. 7 (July). doi:`10.1007/s00348-013-1564-9`.

Lee, T., and Y. Y. Su. 2012. "Wingtip vortex control via the use of a reverse half-delta wing." *Experiments in Fluids* 52, no. 6 (June): 1593–1609. doi:`10.1007/s00348-012-1274-8`.

Lee, T., and L. Ko. 2016a. "Experimental study of the vortex flow and aerodynamic characteristics of a reverse delta wing." *Journal of Aerospace Engineering* 230, no. 6 (May): 1126–1138. doi:`10.1177/0954410015604653`.

Lee, T., L. Ko, and V. Tremblay-Dionne. 2017. "Effect of anhedral on a reverse delta wing." *Proceedings of the Institution of Mechanical Engineers, Part G: Journal of Aerospace Engineering* (July): 095441001771504. doi:`10.1177/0954410017715047`.

Lee, T., and L. Ko. 2016b. "Vortex flow and lift generation of a non-slender reverse delta wing." *Proceedings of the Institution of Mechanical Engineers, Part G: Journal of Aerospace Engineering* 231, no. 13 (November): 2438–2451. doi:`10.1177/0954410016671342`.

Li, Y., J. Wang, G. Tan, and P. Zhang. 2002. "Effects of Gurney flaps on the lift enhancement of a cropped nonslender delta wing." *Experiments in Fluids* 32, no. 1 (January): 99–105. doi:`10.1007/s003480200010`.

Li, Y., and J. Wang. 2003. "Experimental studies on the drag reduction and lift enhancement of a delta wing." *Journal of Aircraft* 40, no. 2 (March): 277–281. doi:`10.2514/2.3120`.

Liebeck, R. H. 1978. "Design of subsonic airfoils for high lift." *Journal of Aircraft* 15, no. 9 (September): 547–561. doi:`10.2514/3.58406`.

Liu, T., and J. Montefort. 2007. "Thin-airfoil theoretical interpretation for Gurney flap lift enhancement." *Journal of Aircraft* 44, no. 2 (March): 667–671. doi:`10.2514/1.27680`.

Lowson, M. V., and A. J. Riley. 1995. "Vortex breakdown control by delta wing geometry." *Journal of Aircraft* 32, no. 4 (July): 832–838. doi:`10.2514/3.46798`.

Luo, S., and Y. Chen. 2012. "Ground effect on flow past a wing with a NACA 0015 cross-section." *Experimental Thermal and Fluid Science* 40 (July): 18–28. doi:`10.1016/j.expthermflusci.2012.01.014`.

Maughmer, M. D., and G. Bramesfeld. 2008. "Experimental investigation of Gurney flaps." *Journal of Aircraft* 45, no. 6 (November): 2062–2067. doi:`10.2514/1.37050`.

Menke, M., H. Yang, and I. Gursul. 1999. "Experiments on the unsteady nature of vortex breakdown over delta wings." *Experiments in Fluids* 27, no. 3 (August): 262–272. doi:`10.1007/s003480050351`.

Meyer, R., W. Hage, D. W. Bechert, M. Schatz, and F. Thiele. 2006. "Drag reduction on Gurney flaps by three-dimensional modifications." *Journal of Aircraft* 43, no. 1 (January): 132–140. doi:`10.2514/1.14294`.

Mitchell, A. M., and J. Délery. 2001. "Research into vortex breakdown control." *Progress in Aerospace Sciences* 37, no. 4 (May): 385–418. doi:`10.1016/s0376-0421(01)00010-0`.

Moffat, R. J. 1998. “Describing the uncertainties in experimental results.” *Experimental Thermal and Fluid Science* 1, no. 1 (January): 3–17. doi:`10.1016/0894-1777(88)90043-x`.

Moon, Y. J., H.-J. Oh, and J.-H. Seo. 2005. “Aerodynamic investigation of three-dimensional wings in ground effect for aero-levitation electric vehicle.” *Aerospace Science and Technology* 9, no. 6 (September): 485–494. doi:`10.1016/j.ast.2005.01.005`.

Musaj, M., and S. A. Prince. 2008. “Numerical and experimental investigation of the aerodynamics of an unconventional W-leading edge reversed delta wing in ground effect.” In *26th International Congress of the Aeronautical Science (ICAS).* Alaska, USA, September 14.

Nelson, R. C., and K. D. Visser. 1990. *Breaking down the delta wing vortex: The Role of Vorticity in the Breakdown Process.* Ph.D. Thesis Final Report. Notre Dame University, October 1.

Nelson, R. C., and A. Pelletier. 2003. “The unsteady aerodynamics of slender wings and aircraft undergoing large amplitude maneuvers.” *Progress in Aerospace Sciences* 39, nos. 2-3 (February): 185–248. doi:`10.1016/s0376-0421(02)00088-x`.

Niu, Y.-Y., T.-S. Hsu, C. T. Hsieh, C. C. Chang, and C. C. Chu. 2010. “How does a Gurney flap enhance the aerodynamics forces?” *AIAA Journal* 48, no. 11 (November): 2710–2714. doi:`10.2514/1.j050437`.

Norris, G., ed. 1998. *Novel SST Configuration Revealed* (December 23): 4.

Nuhait, A., and Zedan. 1993. “Numerical simulation of unsteady flow induced by a flat plate moving near ground.” *Journal of Aircraft* 30, no. 5 (September): 611–617. doi:`10.2514/3.46389`.

Ol, M. V., and M. Gharib. 2003. “Leading-edge vortex structure of nonslender delta wings at low reynolds number.” *AIAA Journal* 41, no. 1 (January): 16–26. doi:`10.2514/2.1930`.

Ollila, R. G. 1980. “Historical review of WIG vehicles.” *Journal of Hydronautics* 14, no. 3 (July): 65–76. doi:`10.2514/3.63187`.

Payne, F. M. 1987. “The structure of leading edge vortex flows including vortex breakdown.” PhD Dissertation, Department of Aerospace and Mechanical Engineering, University of Notre Dame.

Payne, F. M., T. NG, R. C. Nelson, and L. B. Schiff. 1988. “Visualization and wake surveys of vortical flow over a delta wing.” *AIAA Journal* 26, no. 2 (February): 137–143. doi:`10.2514/3.9864`.

Peake, D. J., and M. Tobak. 1983. *On issues concerning flow separation and vortical flows in three dimensions.* NASA-TM-84374. NASA.

Pereira, J. L. 2011. “Experimental investigation of tip vortex control using a half delta shaped tip strake.” PhD diss., McGill University.

Polhamus, E. C. 1971. “Predictions of vortex-lift characteristics by a leading-edge suction analogy.” *Journal of Aircraft* 8, no. 4 (April): 193–199. doi:`10.2514/3.44254`.

Qin, Y., P. Liu, Q. Qu, and H. Guo. 2016. “Numerical study of aerodynamic forces and flow physics of a delta wing in dynamic ground effect.” *Aerospace Science and Technology* 51 (April): 203–221. doi:`10.1016/j.ast.2016.02.007`.

Qin, Y., Q. Qu, P. Liu, Y. Tian, and Z. Lu. 2015. “DDES study of the aerodynamic forces and flow physics of a delta wing in static ground effect.” *Aerospace Science and Technology* 43 (June): 423–436. doi:`10.1016/j.ast.2015.04.004`.

Qu, Q., Z. Lu, H. Guo, P. Liu, and R. K. Agarwal. 2015. “Numerical investigation of the aerodynamics of a delta wing in ground effect.” *Journal of Aircraft* 52, no. 1 (January): 329–340. doi:`10.2514/1.c032735`.

Rahman, H., S. Khushnood, A. Raza, and K. Ahmad. 2013. “Experimental and computational investigation of delta wing aerodynamics.” In *Proceedings of 2013 10th International Bhurban Conference on Applied Sciences & Technology (IBCAST).* IEEE, January 15. doi:`10.1109/ibcast.2013.6512155`.

Ranzenbach, R., and J. Barlow. 1996. “Cambered airfoil in ground effect - an experimental and computational study.” In *SAE Technical Paper Series.* SAE International, February 1. doi:`10.4271/960909`.

Ranzenbach, R., and J. B. Barlow. 1994. "Two-dimensional airfoil in ground effect, an experimental and computational study." In *SAE Technical Paper Series.* SAE International, December 1. doi:`10.4271/942509`.

Raymond, A. E. 1921. *Ground influence of airfoils.* Technical Note. National Advisory Committee for Aeronautics, December.

Roberts, L. S., M. V. Finnis, and K. Knowles. 2016. "Characteristics of boundary-layer transition and Reynolds-number sensitivity of three-dimensional wings of varying complexity operating in ground Effect." *Journal of Fluids Engineering* 138, no. 9 (June): 091106. doi:`10.1115/1.4033299`.

Rozhdestvensky, K. V. 2006. "Wing-in-ground effect vehicles." *Progress in Aerospace Sciences* 42, no. 3 (May): 211–283. doi:`10.1016/j.paerosci.2006.10.001`.

Schweikhard, W. 1967. "A method for in-flight measurement of ground effect on fixed-wing aircraft." *Journal of Aircraft* 4, no. 2 (March): 101–104. doi:`10.2514/3.43804`.

Traub, L. W. 2000. "Effects of anhedral and dihedral on a 75-deg Sweep delta wing." *Journal of Aircraft* 37, no. 2 (March): 302–312. doi:`10.2514/2.2594`.

Traub, L. W., and S. F. Galls. 1999. "Effects of leading- and trailing-edge Gurney flaps on a delta wing." *Journal of Aircraft* 36, no. 4 (July): 651–658. doi:`10.2514/2.2507`.

Troolin, D. R., E. K. Longmire, and W. T. Lai. 2006. "Time resolved PIV analysis of flow over a NACA 0015 airfoil with Gurney flap." *Experiments in Fluids* 41, no. 2 (August): 241–254. doi:`10.1007/s00348-006-0143-8`.

Urquhart, S., S. Prince, and V. Khodagolian. 2006. "Aerodynamic study of reversed-delta wing surface craft in ground effect." In *44th AIAA Aerospace Sciences Meeting and Exhibit.* American Institute of Aeronautics / Astronautics, January 9. doi:`10.2514/6.2006-253`.

Vess, R. J., R. A. Wahls, and C. A. Moksovitz. 1986. "Experimental investigation of apex fence flaps on delta wings." *Journal of Aircraft* 23, no. 10 (October): 789–797. doi:`10.2514/3.45382`.

Vincenti, W. G., J. N. Nielsen, and F. H. Matteson. 1947. *Investigation of wing characteristics at a Mach number of 1.53. I - triangular wings of aspect ratio 2: NACA RM No. A7I10.* Research Memorandum. Ames Aeronautical Laboratory, Moffett Field, California: NACA, December 19.

Visser, K. D., and R. C. Nelson. 1993. "Measurements of circulation and vorticity in the leading-edge vortex of a delta wing." *AIAA Journal* 31, no. 1 (January): 104–111. doi:`10.2514/3.11325`.

Wang, H., C. Teo, B. Khoo, and C. Goh. 2013. "Computational aerodynamics and flight stability of wing-in-ground (WIG) craft." *Procedia Engineering* 67 (May): 15–24. doi:`10.1016/j.proeng.2013.12.002`.

Wang, J., Y. Li, and K.-S. Choi. 2008. "Gurney flap—Lift enhancement, mechanisms and applications." *Progress in Aerospace Sciences* 44, no. 1 (January): 22–47. doi:`10.1016/j.paerosci.2007.10.001`.

Yang, Z., W. Yang, and Y. Li. 2009. "Analysis of two configurations for a commercial WIG craft based on CFD." In *27th AIAA Applied Aerodynamics Conference.* American Institute of Aeronautics / Astronautics, June 22. doi:`10.2514/6.2009-4112`.

Zerihan, J., and X. Zhang. 2000. "Aerodynamics of a single element wing in ground effect." *Journal of Aircraft* 37, no. 6 (November): 1058–1064. doi:`10.2514/2.2711`.

———. 2001. "Aerodynamics of Gurney flaps on a wing in ground effect." *AIAA Journal* 39, no. 5 (May): 772–780. doi:`10.2514/2.1396`.

Zhang, X., and J. Zerihan. 2003a. "Aerodynamics of a double-element wing in ground effect." *AIAA Journal* 41, no. 6 (June): 1007–1016. doi:`10.2514/2.2057`.

———. 2003b. "Off-surface aerodynamic measurements of a wing in ground effect." *Journal of Aircraft* 40, no. 4 (July): 716–725. doi:`10.2514/2.3150`.